2014-04-28

Advanced Digital Signal Processing Techniques for Linearization of Multi-band Transmitters

Younes, Mayada Fawzy

UNIVERSITY OF CALGARY

Advanced Digital Signal Processing Techniques for Linearization of Multi-band Transmitters

by

Mayada Fawzy Younes

A THESIS

SUBMITTED TO THE FACULTY OF GRADUATE STUDIES

IN PARTIAL FULFILLMENT OF THE REQUIREMENTS FOR THE

DEGREE OF DOCTOR OF PHILOSOPHY

DEPARTMENT OF ELECTRICAL AND COMPUTER ENGINEERING

CALGARY, ALBERTA

April, 2014

Abstract

Due to the increasing demands for large capacity and high performance wireless transmitters, multi-band/multi-standard transmitter architectures play an important role in modern communication. Thus, advances in the design techniques of radio frequency (RF) power amplifiers (PAs) have promoted it to use single multi-band PA and RF components in order to concurrently process multiple input signals located in different frequency bands.

In this dissertation, different RF imperfections are investigated and compensated for in multi-band wireless communications systems. Thus, a comprehensive analysis and different digital signal processing (DSP) solutions are proposed for distortion mitigation of different RF impairments in dual-band and tri-band transmitters.

A novel Feedforward Hammerstein model/DPD is proposed for the accurate characterization of the dynamic, nonlinear behavior of RF PAs. Indeed, the performance of different DPD linearizers is affected by the imperfections of the up-converters in the transmission path and down-converters in the feedback path. Therefore, a complexity-reduced compound DPD is proposed for the compensation of the impairments stemming from the quadrature modulators and PA nonlinearity in single-band transmitters.

This study is extended for multi-band transmitters and the nonlinear distortion in case of dual-band transmitters is analyzed. Indeed, the problem of modulator imperfections is more highlighted in multi-band transmitters. Therefore, a dual-input truncated Volterra DPD is proposed for the joint mitigation of dual-band PA distortion in the presence of modulator imperfections.

A theoretical analysis of the nonlinear distortion in the concurrent tri-band PA has been

given, and a three-dimensional (3-D) DPD is presented for the linearization of tri-band PA. The analysis is further extended in order to include the effects of the phase distortion in tri-band transmitters. Indeed, the transmitter wideband phase variation effects will affect the transmission quality and needs to be compensated for. Therefore, a novel 3-D phase-aligned DPD is proposed that takes into account both the compound amplitude and phase variation effects in a concurrent tri-band transmitter.

Finally, in order to reduce the computational complexity of multi-band DPDs, a novel multi-branch DPD is proposed for the linearization of dual-band transmitters. The proposed model is based on a distributed polynomial basis function with a radial pruning approach.

Acknowledgements

I am deeply indebted to my supervisor, Prof. Fadhel Ghannouchi, for his guidance, support, and advice throughout my dissertation. Prof. Ghannouchi helped me to identify research problems and provided me with his full support and financial help in order to pursue my studies.

I gratefully acknowledge the Alberta Innovates Technology Future (AITF) Institute, which provided me with AITF Doctoral Award that allowed me to pursue my degree.

I would like to give many thanks to all my friends, current, and previous colleagues in iRadio Lab for their ongoing help and support whenever I needed it. I would like to thank specifically Andrew Kwan for providing technical advice that helped me alot during my research. Also, I would like to thank Dr. Oualid Hammi, who helped and guided me a lot when I started my studies in iRadio lab.

Finally, I would like to give my sincere gratitude to the most important people in my life, my family. I deeply appreciate and give my heartfelt thanks to my parents, Fatma Hashem and Fawzy Younes, for their love and support, and to my loving sisters, Miranda and Marwa. Especially, I would like to thank my husband, Hazem, and my loving daughter, Jumana, that have blessed me with their unconditional support and encouragement.

To my beautiful daughter, Jumana Gomaa.

Table of Contents

List of Tables

List of Figures and Illustrations

List of Symbols, Abbreviations and Nomenclature

Symbol	Definition
2-D	Two-Dimensional
3-D	Three-Dimensional
2G	Second Generation
3G	Third Generation
4G	Fourth Generation
ACEPR	Adjacent Channel Error Power Ratio
ACPR	Adjacent Channel Power Ratio
ADC	Analog-to-Digital Converter
AM-AM	Amplitude Modulation to Amplitude Modulation
AM-PM	Amplitude Modulation to Phase Modulation
BER	Bit Error Rate
CA	Carrier Aggregation
DAC	Digital-to-Analog Converter
DPD	Digital PreDistortion
DSP	Digital Signal Processing
DUT	Device Under Test
EVM	Error Vector Magnitude
FIR	Finite Impulse Response
FLOP	FLoating Point Operations
GPIB	General Purpose Interface Bus

IF	Intermediate Frequency
I/Q	In-phase / Quadrature-phase
IRR	Image Rejection Ratio
LDMOS	Laterally Diffused Metal Oxide Semiconductor
LO	Local Oscillator
LS	Least Squares
LTE	Long Term Evolution
LUT	Look-Up Table
MFI	Mirror Frequency Interference
MP	Memory Polynomial
NMSE	Normalized Mean Square Error
OFDM	Orthogonal Frequency Division Multiplexed
PA	Power Amplifier
PAPR	Peak to Average Power Ratio
PM-AM	Phase Modulation to Amplitude Modulation
PM-PM	Phase Modulation to Phase Modulation
PSD	Power Spectral Density
RF	Radio Frequency
TX	Transmitter
VSA	Vector Signal Analyzer
VSG	Vector Signal Generator
WCDMA	Wideband Code Division Multiple Access

WiMAX	Worldwide Interoperability for Microwave Access
WLAN	Wireless Local Access Network

Chapter 1

Introduction

Wireless and mobile communications have become a ubiquitous part of modern life, from mobile phones to local and wireless personal area networks. A number of these wireless technologies, such as Long Term evolution (LTE) and worldwide interoperability for microwave access (WiMAX), are being developed to support higher data rate wireless services. The next generation network is expected to support data rates up to 100 megabits per second (Mb/s) for high mobility and approximately 1 gegabits per second (Gb/s) for low mobility. However, this placed very challenging demands on radio frequency (RF) front-end specifications in terms of bandwidth and power efficiency for both hand-held devices and base stations.

As the RF spectrum nowadays is shared by many users, the available bandwidth is fixed or even decreasing. Therefore, spectral efficient complex modulation schemes, such as single-carrier frequency division multiple access (SC-FDMA) and orthogonal frequency-division multiplexing (OFDM), have to be used. While existing global systems for second generation (2G) and third generation (3G) networks continue to thrive and represent a large percentage of networks today, network operators continue to roll out fourth generation (4G) carrier aggregated (CA) LTE networks [1, 2]. In order to access these various systems and services using a single user terminal, highly flexible and re-configurable radio transceivers are needed. The transceiver design should be able to simultaneously support the different frequency bands in existing and future wireless networks. Therefore, multi-band/multi-standard transceivers

are recently getting more attention and optimized in order to reduce cost, physical size, and power consumption. Hence, there is a keen motivation towards developing various passive or active RF circuits with multi-band/wideband operation capabilities [3–5].

The direct conversion transceiver [6, 7] is one of the most flexible and versatile architectures with low power and low cost. It up-converts the baseband signal to RF, or down-converts the RF signal to the baseband, directly without any intermediate frequency (IF) stage. Fig. 1.1 shows a simplified block diagram of a direct conversion transceiver. The transmitter performs digital baseband waveform generation, digital-to-analog conversion (DAC), up-conversion of the analog baseband signal to RF, bandpass filtering to eliminate harmonics, and then power amplification.

The direct conversion receiver down-converts the received signal directly from the RF to the baseband frequencies. The received signal is first amplified with low-noise amplifier (LNA) to compensate for transmission losses and is then bandpass filtered. Then, the signal is down-converted directly to the baseband with complex mixing. The in-phase (I) and quadrature (Q) components of the complex signal are then separately low-pass filtered, analog-to-digital converted (ADC), and waveform processed to decode the transmitted data.

This direct conversion transceiver can be extended to support different multi-band and multi-standard architectures. Thus, the multi-band transceivers provide the possibility of moving from one standard to another, or hopping to different carrier frequencies, while using the same device.

This dissertation focuses on advanced DSP techniques for mitigation of the main sources of linear and nonlinear distortion that degrade the overall performance of wireless systems. These techniques are first applied for single-band and then further extended in order to

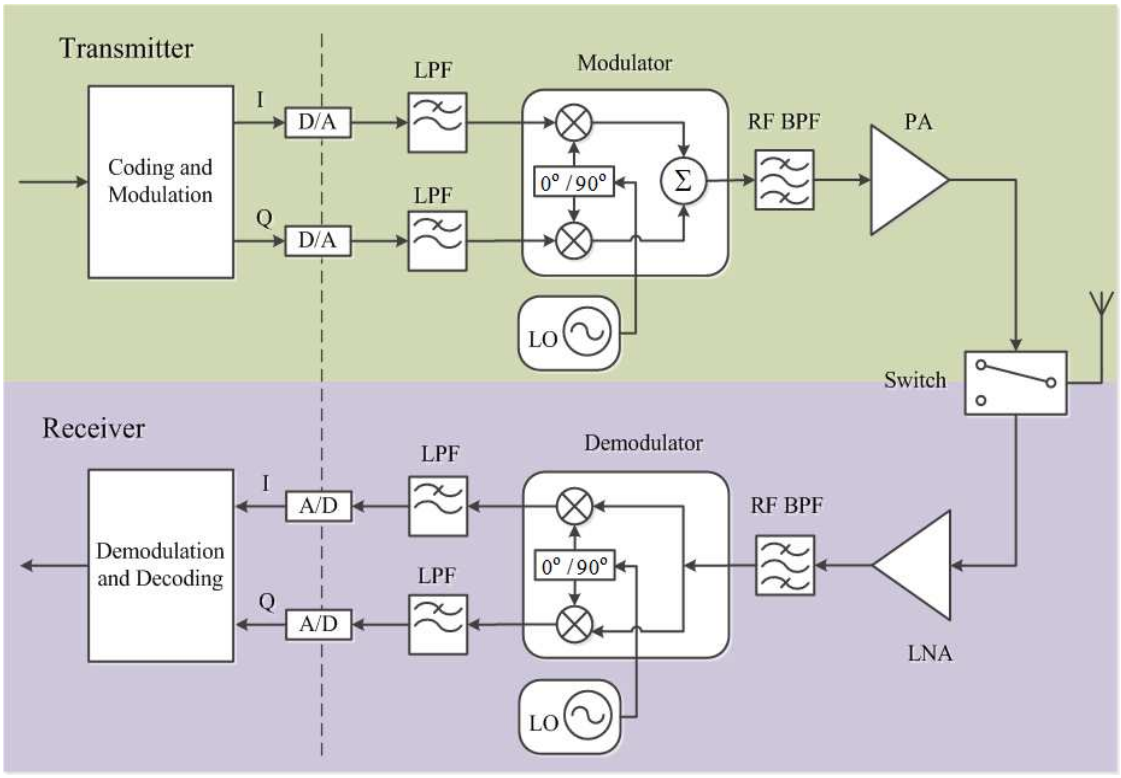

Figure 1.1: Block diagram of direct conversion transceiver.

compensate for the different impairments of multi-band transmitters.

In this introduction chapter, a background review is presented. The remainder of this chapter is organized as follows. First, the different sources of distortion in single-branch transmitters are discussed in Section 1.1. Then, the different multi-branch transmitter architectures are reviewed in Section 1.2. The additional sources of distortion in multi-band transmitters, such as inter-modulation and cross-modulation products are discussed in Section 1.3. Following in Section 1.4 are the motivations and the list of contributions. Finally, the outline of this dissertation is presented in Section 1.5.

1.1 Distortion in RF transmitters

The direct conversion transmitter architecture shown in Fig. 1.1 has different sources of distortion [8]. The most prominent imperfections are static and dynamic distortion due to mixer and PA nonlinearities [9], image-frequency interference due to in-phase/quadrature (I/Q) imbalance in modulators [10], non-constant group delay variations in band-pass filters [11, 12], and the antenna. This thesis is focused on the distortion sources created by the modulator and PA as the primary sources of distortion in wireless transmitters [13,14]. Also, the non-constant group delay distortion in the case of wideband transmitters is investigated.

1.1.1 Power amplifier nonlinearity

The radio frequency (RF) power amplifier (PA) is a key component in the RF front-ends of wireless transceivers. It is also the main power consuming device that generates unwanted nonlinear distortion [9, 15]. The purpose of the RF PA is to amplify the radio signal to a necessary power level for transmission to the receiver. The RF PAs are divided into different classes (e.g. A, AB, B, C, D and F etc.), with respect to their linearity and power efficiency. For a linear system, most of the power transmitted by the base station is confined to an allocated channel of a confined bandwidth. However for the PAs to operate efficiently, they have to be operated close to saturation region. Thus, the PAs exhibit undesired nonlinear behavior that generate distortion of a bandwidth three to five times the allocated channel bandwidth. The broadening of the distortion spectrum is known as spectral regrowth.

As modern wireless communication systems have evolved to be more spectral efficient, they utilized high peak-to-average power ratio (PAPR) signals. The high PAPR signals

are caused by complex modulation schemes and generate rapid change in the magnitude of signals. These varying envelope signals cause amplitude to amplitude (AM-AM) and amplitude to phase (AM-PM) distortion as well as spectral regrowth in the adjacent channels when amplified by nonlinear PAs. Therefore, the use of high PAPR signals results in PA operating at a large enough back-off to satisfy the stringent linearity requirement at the expense of degraded efficiency [16]. Therefore, linearization [17] and efficiency enhancement [15, 18, 19] techniques must be employed. This issue is widely explored in literature.

Some of the efficiency enhancement techniques explored in literature include Doherty [20, 21], Envelope Elimination and Restoration (EER) [22–24], Envelope Tracking (ET) [25–27], linear amplification with nonlinear control (LINC) [28], and delta sigma based modulators [29]. The most commonly known linearization techniques are mainly feedback [30–32], feedforward [32,33], and analog or digital predistortion [34]. Among these, digital predistortion (DPD) is one of the most promising linearization techniques [35–37] for the compensation of the static and dynamic distortion in transmitters. In order to work, digital predistortion requires knowledge of the dynamic nonlinear characteristics of the device under test (DUT) since it, in principle, applies the inverse of the amplifier characteristics to the signal prior to amplification. Fig. 1.2 shows a general schematic of a DPD. The AM-AM plots show that the cascade of the predistorter that show an inverse of the nonlinearity of the PA prior to the DUT, will result in a linearized output signal.

Accurate nonlinear characterization of the amplifiers is necessary for the design of DPDs and for optimizing the amplifier design. Thus, behavioral modeling, also denoted as black-box modeling, of RF PAs / transmitters is a cost and time effective approach to predict the nonlinearity generated at the output of the PA [37]. Contrary to the physics based modeling,

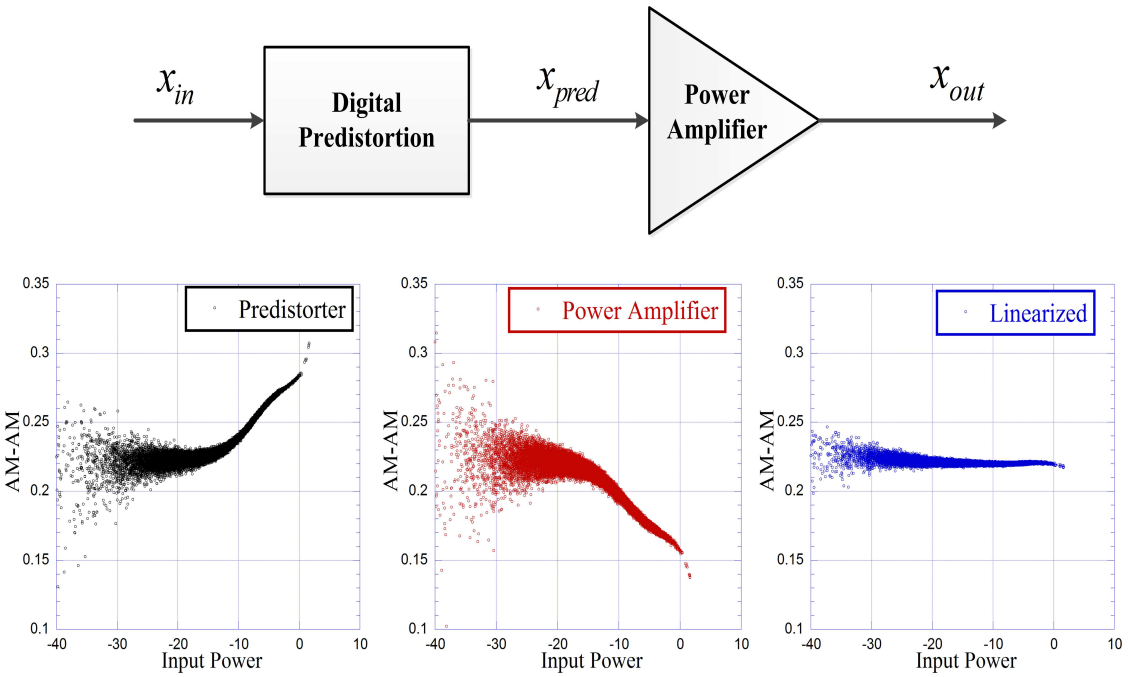

Figure 1.2: Schematic of a DPD.

the key benefit of the behavioral modeling is that it does not require a detailed knowledge of the circuit physics of the DUT. The system to be modeled is considered as a black box, wherein a mathematical representation of its transfer function is chosen and the model coefficients are then identified based on the characterization results. Numerous behavioral models suitable for PAs exhibiting memory effects have been proposed in literature. A detailed comparative study of different behavioral PA models and DPDs including a detailed classification is given in [37–40].

1.1.2 I/Q modulator nonidealities

One of the major sources of RF impairments that transmitters suffer from are the hardware imperfections of the modulators required for up-conversion of the transmitted signals. As a linearized transmitter uses a quadrature modulator to transfer the predistorted baseband signal to the RF frequency. Therefore, DPD performance is highly affected by the modulator

impairments. These imbalances are due to the imperfections of the analog RF components that result in I/Q imbalances and DC offsets due to signal leakages in local oscillators (LO) [10, 14]. In practice, the mixer does not have equal gain in the I- and Q- branches. Also, the phase shift between the quadrature ports is not exactly 90 degrees. In addition to that, the relative mismatch between the components in the I- and Q- branches such as low path filters and DACs contribute to the overall I/Q imbalance problem. IQ modulator imperfections degrade the quality of the transmitted signal during the modulation process. This degrades the Error Vector Magnitude (EVM) at the receiver, which in turn degrades the Bit Error Rate (BER) and also results in limited suppression of the image signal [10].

In most articles discussing baseband communication techniques, the effects of I/Q imbalance is ignored in the design and performance analysis since it is normally considered in the RF front-end design. However, in practice, such assumption is unrealistic, especially in multi-carrier communication systems. Indeed, in such cases, the I/Q imbalance, including amplitude imbalance and phase imbalance, is introduced into the received signal after analog processing, which in turn can cause interference and power loss.

The performance degradation due to I/Q imbalance highlights the need for compensation schemes in order to eliminate, or at least mitigate, the effects of I/Q imperfections on the performance of wireless communication systems. Recently, several compensation schemes for I/Q imbalance have been proposed at both the transmitter and receiver side [41].

1.2 Transmitter Architectures

The transmitter architecture is the building block of the communication systems. It is the physical layer of the system and the actual device that sends the modulated signal through the wireless channel. Different transmitter topologies are given in [42] and shown in Fig. 1.3.

1.2.1 Single-branch Transmitters

Fig. 1.3a presents a conventional single-band transmitter architecture that consists of a digital baseband processing unit, a single-band RF PA, filters, and other transmitter components. The RF front end can be one of the conventional architectures; direct conversion [7], super-heterodyne, or low-IF [43]. The main sources of distortion in single-branch transmitter architectures are shown in the previous sections.

1.2.2 Multi-branch Transmitters

The recent technologies nowadays are evolving towards the concurrent transmission of multi-carrier signals at different frequency bands, in order to accommodate different standards, simultaneously. Indeed, novel transmitter designs allow for different communication signals to be transmitted on different frequency bands, concurrently. Therefore, for multi-band transmission, the conventional single-band transmitter in Fig. 1.3a is modified using different topolgoies as shown in Figs. 1.3b - 1.3d.

The power amplification unit is the main building block of the transmitter RF front end in these different topologies. The transmitter architectures in Fig. 1.3b and Fig. 1.3c are considered as multi-branch transmitters (separate RF PAs), while the transmitter architecture in Fig. 1.3d is considered as a multi-band transmitter architecture (single PA).

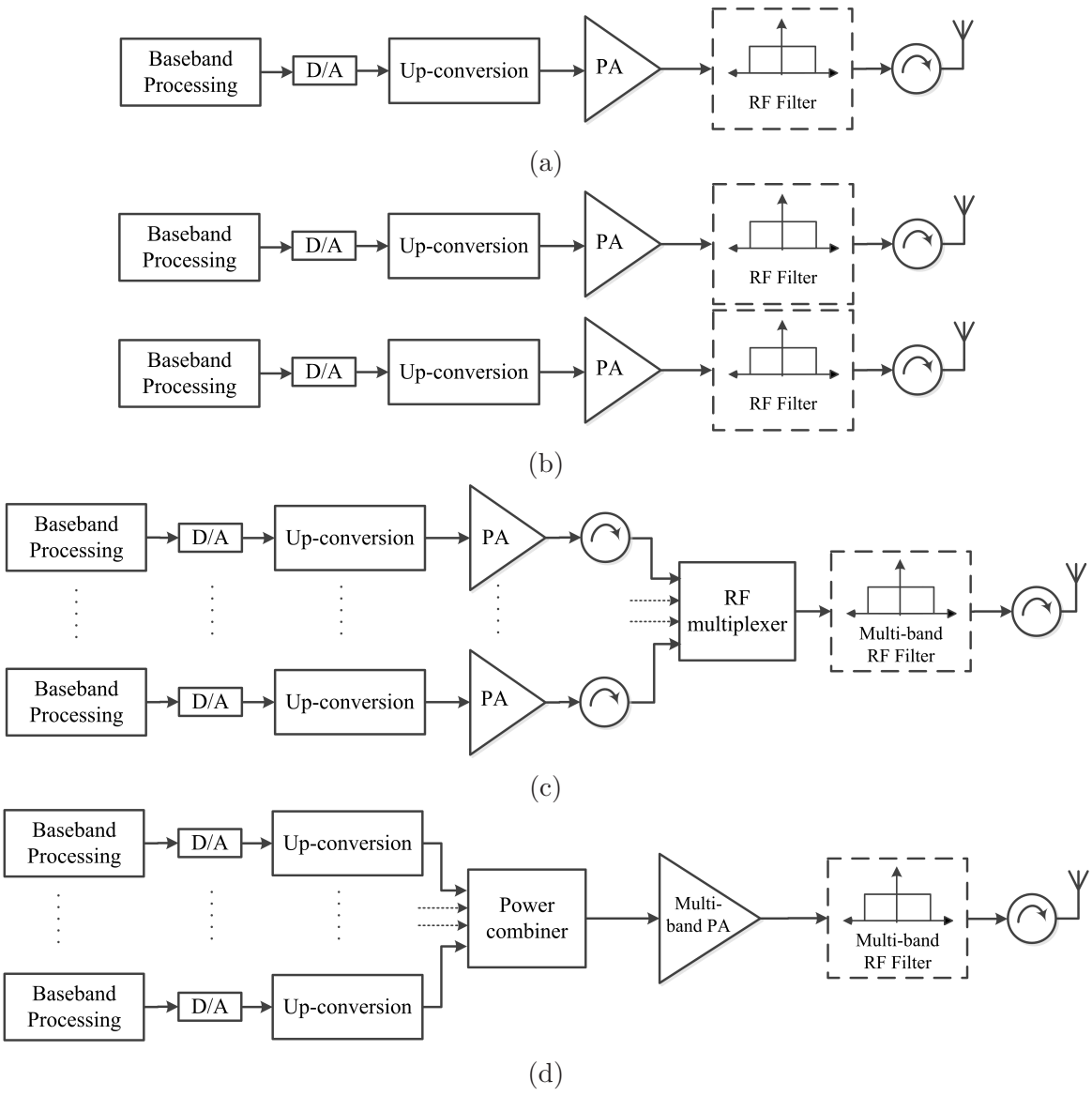

Figure 1.3: Transmitter Architectures: (a) single-branch RF transmitter, (b) multi-branch RF transmitter, (c) multi-branch RF transmitter with multi-band final stage, (d) multi-band RF transmitter architecture.

Fig. 1.3b shows multiple branches of the conventional transmitter, with each branch operating in a single frequency band. This transmitter has large circuit size, which is a main disadvantage in this topology. In order to decrease the circuit size and remove the need of bulky components, multi-band/wideband operation circuit components replace the single RF components. Fig. 1.3c and Fig. 1.3d show two possible transmitter architectures where multi-band RF components have been used.

In Fig. 1.3c, the final stage of the transmitter, the RF filters and antenna have been designed using multi-band RF components. Each RF chain has its own power amplification stage. The RF signals at the output of the power amplification stages are combined by using an RF multiplexer and passed through a multi-band RF filter. In this architecture, a linearization unit is required for the compensation of the PA nonlinear distortion in each branch, separately. In order to design more compact and efficient transmitter topologies, a single-band PA with multi-band operation is designed in order to replace the different single-band PAs each working at a single operating frequency.

Fig. 1.3d presents the multi-band architecture with one PA that could operate at different frequency bands. In this architecture, the RF signals are generated using different modulators and then combined using a low power combiner instead of the high power combiner in Fig. 1.3c. The signal at the output of the multi-band PA is filtered using a multi-band RF filter and finally passed to the antenna.

The number of PAs and the possible position of the power combination module before or after the PA affect the overall efficiency of the two transmitters shown in Figs. 1.3c and 1.3d. The loss and distortion output of the two transmitters are also affected by the two different topologies.

The multi-band transmitter architectures are designed to have a flat frequency response among the desired frequency bands. However, a high-output, high-efficiency PA design is difficult when the upper and lower limits of the required frequency bands are further apart. Finally, the multi-band amplifier shown in Fig. 1.3d consists of a single amplification device and variable matching networks that can be changed. The multi-band architecture can be designed for different frequency bands as the multi-branch architectures in Figs. 1.3b and 1.3c, which means high-efficiency and high power PA designs can be achieved with smaller circuit sizes and without the need of bulky components.

1.3 Distortion of multi-band transmitters

Recent technologies nowadays tend to use multi-band architectures [4] as shown in Fig. 1.3d. These band re-configurable architectures show more promise for software defined radio applications. Therefore, novel designs of dual-band [44–47] and tri-band PAs [48, 49] have been proposed, which can accommodate the transmission of signals in different RF bands concurrently or selectively utilizing the same hardware configuration.

However, the operation of multi-band PAs in concurrent mode results in inherent in-band and cross-band distortion, which are more severe than the inter-modulation products and spectral regrowth distortion that are observed at the output of the transmitter even in single-band [50]. This is demonstrated in Fig. 1.4, which shows the output distortion products for a dual-band transmitter when excited with a two-tone signal in each band. Thus, the nonlinear behavior of the dual-band transmitters is much more noticeable, in which two modulated signals that are separated in carrier frequencies by $\triangle\ \omega$ are transmitted simultaneously.

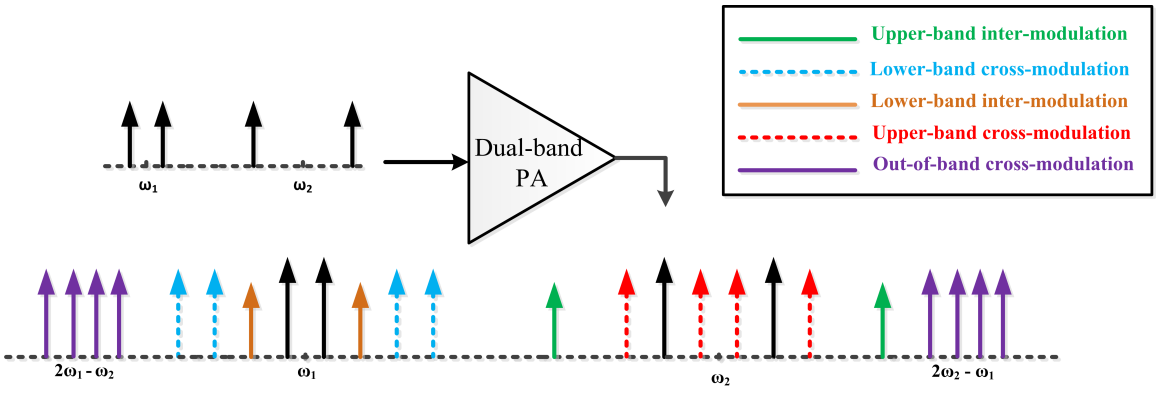

Figure 1.4: Power spectrum of the output of a dual-band transmitter.

As shown in Fig. 1.4, the output distortion of multi-band transmitters can be categorized into different groups. These groups are the in-band inter-modulation products, the cross-modulation products, and the out-of-band inter-modulation products. The first group consists of the inter-modulation products around each carrier frequency band that are caused by the nonlinearity of the PA, similar to what it is in single-band transmitters. The second group, which includes the cross-modulation products, appears within the same frequency range as the in-band inter-modulation. These cross-modulation products result from the interactions of the multi-input signals in the nonlinear PA. Finally, the last group, which is referred to as out-of-band inter-modulation, is the inter-modulation products between the input signals which happen in the different carrier frequency bands. These terms are located at different frequency bands, that are far enough from the transmitted bands in case of widely spaced carriers and can be filtered out in this case. Also, these higher-order products would lie in near bands to the transmitted bands in case of narrow-spaced carriers. In this case, they should be compensated for in order not to effect the quality of the carriers of the transmitted bands.

Therefore, distortion mitigation in the multi-band PAs is an essential task, and force

tougher requirements than the distortion compensation in a single-band transmitter.

However, when treating the system as a traditional single-input single-output (SISO) system and using conventional DPD techniques, the requirement of DACs and ADCs increases heavily depending on the frequency separation of the bands. Therefore, using multi-band DPD cells, where the RF signals in each band are captured and digitized separately, alleviates such problem. Indeed, the DPD cells will compensate for the distortion in each band separately and is independent of the frequency separation between the bands, which will require lower sampling rates than using wideband DPD [51, 52].

1.4 Motivation and Contributions

The scope of this dissertation is the behavioral modeling and digital predistortion of wireless multi-band transmitters. Multi-band power transmitter architectures are a simple way to increase the data rates and/or diversity of a wireless system, and can allow the transmission of different wireless communication signals. Therefore, they are an attractive solution due to their strong application potential in the future CA LTE systems, especially in concurrent modes of operation.

For complete transmitter linearization, a second concern is the transmitter imperfections generated at the modulator and other linear components. These imperfections include the relative amplitude and phase mismatches between the I- and Q- signal branches of direct-conversion radios. This will result in mirror frequency interference (MFI) effect [14, 53] that may cause self-interference or adjacent channel interference, depending on the spectral content of the low-frequency I and Q signals (baseband or low intermediate frequency). In

addition to this problem, I/Q imbalance and LO leakage are known to cause extra intermodulation distortion to appear at the PA output, as well as to deteriorate the performance of PA/ Transmitter predistorters [10].

Adaptability of the predistortion system is another desirable aspect in which the model configuration does not have to be changed as operating conditions change. Moreover, for an adaptive predistortion system, it is desirable that the time delay is adjusted only once using delay lines. Then, the predistorter should capable of compensating for any other small fluctuations in time delay between predistorter and transmitter output. Present predistorter models are mainly concerned with PA linearity, while I/Q imbalance and LO leakages are mitigated separately before applying the predistorter. Afterwards, the PA linearization will be considered separately. Hence, the whole transmitter linearization will be a two-step process [54] that requires two compensating circuits, which adds further complexity.

Therefore, this dissertation focuses on the joint mitigation of different RF impairments in multi-band/multi-standard systems. The effects of the different RF impairments and their impact on multi-band transmitters are analyzed and evaluated. Then, different digital signal processing (DSP) solutions for the joint compensation of these imperfections are proposed. The key contributions of this dissertation can be summarized as follows:

- A novel Feedforward model is proposed for the accurate modeling and linearization of single-band RF PAs.
- A new Generalized Twin-box model is developed for the joint and simultaneous compensation of the effects of I/Q imbalance and single-band transmitter distortion.

- A multi-cell linearization technique, based on a dual-input truncated Volterra DPD, is proposed to compensate for a dual-band transmitter distortion. This includes the inter-modulation and cross-modulation products in dual-band PAs as well as the modulators imperfections. The proposed DPD can be used for zero-IF and low-IF dual-band transmitter.

- An Analysis of the nonlinearities and DPD linearization of concurrent tri-band systems is given for the first time.

- The effect of phase distortion due to linear filtering in tri-band communication systems is discussed, and a novel 3-D phase-aligned DPD is proposed for the effective compensation of the compound amplitude and phase distortion.

- Based on the 3-D phase-aligned DPD, a complexity-reduced multi-branch DPD is derived for dual-band transmitter linearization. The proposed DPD is based on multi-dimensional radial pruning technique that separately characterize the dynamic nonlinearities of the cross-modulation products.

1.4.1 List of Publications

The work carried out for this thesis resulted in the following peer-reviewed publications:

Journal Papers

P1: M. Younes, A. Kwan, M. Rawat, and F. M. Ghannouchi, "Linearization of Concurrent Tri-Band Transmitters Using 3-D Phase-Aligned Pruned Volterra Model," *IEEE Trans. Microw. Theory Tech.*, vol. 61, no. 12, pp. 4569-4578, Dec. 2013.

P2: M. Younes, F. M. Ghannouchi, "An accurate predistorter based on a feedforward hammerstein structure," *IEEE Trans. Broadcast.*, vol. 58, no. 3, pp. 454-461, Sept. 2012.

P3: M. Younes and F. M. Ghannouchi, "On the modeling and linearization of a concurrent dual-band transmitter exhibiting nonlinear distortion and hardware impairments," *IEEE Trans. Circuits Syst. I*, Reg. Papers, vol. 60, no. 11, pp. 3055-3068, Nov. 2013.

P4: M. Younes and F. M. Ghannouchi, "Generalised twin-box model for compensation of transmitters radio frequency impairments," *IET Communications*, vol. 8, no. 4, pp. 413-418, March 2014.

P5: F. M. Ghannouchi, M. Younes, and M. Rawat, "Distortion and impairments mitigation and compensation of single- and multi-band wireless transmitters (invited)," *IET Microwaves, Antennas & Propagation*, vol. 7, no. 7, pp. 518-534, May 2013.

P6: M. Rawat, K. Rawat, M. Younes, and F. M. Ghannouchi, "Joint Mitigation of Non-Linearity and modulator imperfections in a dual-band Concurrent Transmitter Using Neural Networks," *IET Electronics Letters*, vol. 49, no. 4, pp. 253-255, Feb. 2013.

Conference Papers

C1: M. Younes, A. Kwan, M. Rawat, and F. M. Ghannouchi, "Three-dimensional digital predistorter for concurrent tri-band power amplifier linearization," in

IEEE MTT-S Int. Microw. Symp. Dig., Seattle, WA, Jun. 2013, pp. 1-4.

C2: M. Younes, A. Kwan, and F. M. Ghannouchi, "Digital Predistortion of Concurrent Dual-Band Power Amplifier based on Two-dimensional Multi-Branch DPD," *IEEE Canadian Conference on Electrical and Computer Engineering 2014* (CCECE 2014), Toronto, On., May. 2014, pp. 1-5.

C3: A. Kwan, M. Younes, S. Zhang, W. Chen, R. Darraji, M. Helaoui, F. M. Ghannouchi, "Dual-band Predistortion Linearization of an Envelope Modulated Power Amplifier Operated in Concurrent Multi-Standard Mode," in *IEEE MTT-S Int. Microw. Symp. Dig. 2014*, Tampa bay, Florida, USA, Jun. 2014, pp. 1-4.

1.5 Dissertation Organization

The dissertation is organized as follows: In Chapter 2, an overview of the mathematical modeling and digital predistortion of single-band transmitters is presented. An accurate Feedforward Hammerstein structure is proposed for the modeling/DPD of the PA. It is composed of two coupled loops, a signal cancellation loop for the modeling of the PA behavior and a distortion injection loop for the modeling of the distortion, which enhances the model accuracy due to the better characterizing of the PA inter-modulation distortion products.

In Chapter 3, the RF front end impairments such as mismatches between the I and Q branches and DC offsets that degrade the performance of direct conversion transmitters are investigated. A single-step compound structure for the joint estimation and compensation of I/Q modulator imperfections as well as the single band PA distortion is developed, without

the need of extra RF hardware. Therefore, the proposed DPD is generic in the sense that it will be able to adapt to any change in the input data even in the presence of modulator I/Q imbalance.

In Chapter 4, a study of the characterization of a dual-band PA output distortion is presented, where the output distortion arises from the cross modulation and inter-modulation products that result from interaction of the multiple channels in a nonlinear environment, concurrently. These manifest themselves as extra in-band and out-of-band distortion than the operation in single-band. So, a dual-input truncated Volterra model is proposed for the joint mitigation of dual-band PA inter-modulation and cross-modulation distortion in the presence of modulator imperfections and DC offset. The proposed model showed enhanced performance than the state-of-the-art as well as a complexity reduced structure. Therefore, it is more practical for implementation on DSP/FPGA platform as well as it is more economical in utilizing the FPGA resources.

In Chapter 5, the nonlinear behavior of tri-band PAs is analyzed. The effect of phase and group delay variations in the pass-band of RF filter circuits is undesirable in communications systems. However, it is difficult to achieve constant group delay effects in wideband systems, or even in narrow-band communications when tight filtering is required. Any in-band group delay distortion in the circuit inevitably distorts its output signal by introducing inter-symbol interference, thereby degrading the overall system performance. Therefore, a phase-aligned three-dimensional (3-D) DPD is proposed that accounts for the phase-variation effects in tri-band transmitters.

In Chapter 6, a multi-branch two-dimensional (2-D) DPD is proposed for concurrent dual-band PA linearization. The proposed DPD is based on multi-branch basis functions that

incorporates the amplitude and phase variation effects. The model is based on distributed polynomial system with separate identification of the dynamic nonlinear behavior of the dual-band PA, in order to generate a complexity-reduced model.

Chapter 7 concludes the dissertation with a summary of this work. The key points and main contributions of the dissertation are summarized. Finally, future research directions related to advanced signal processing techniques to compensate for the distortion and nonlinearities of the next generation of wireless communication transmitters are recommended.

Chapter 2

An Accurate Predistorter based on a Feedforward Hammerstein Structure

2.1 Introduction

Nowadays, stringent efficiency and linearity requirements are demanded in wireless communication systems, mostly in base stations and mobile phones as mentioned in Chapter 1. Different modulated signals, such as wideband code division multiple access (WCDMA) and orthogonal frequency division multiplexed (OFDM) signals, are used in order to maintain good system spectral efficiency. However, these varying-envelope signals are vulnerable to spectral regrowth and in-band distortions when amplified by RF PAs, which are excessively nonlinear and affect the performance of wireless systems [55–57]. Also, these signals have high peak-to-average power ratios (PAPR), which require the PA to be operated in its linear region to avoid the nonlinear distortion.

However, the PA operation in the linear region would result in very poor efficiency, which is impractical for the battery life in mobile phones and other portable device applications. Thus, a trade-off between linearity and power efficiency occurs, as the linearity degradation is more significant when PAs operate near their saturation points, where high efficiency can be achieved.

Thus, various linearization techniques have been proposed in the literature [17]. The most commonly known linearization techniques are mainly feedback [30–32], feedforward [32, 33],

and analog or digital predistortion [34]. One of the most promising and efficient linearization techniques is digital predistortion (DPD) [36, 37]. Digital predistortion is one of the most cost-effective and efficient linearization techniques. Thus, behavioral modeling is an essential first task in the development of different DPD functions, as it analyzes different PA behavior.

This chapter presents a feedforward Hammerstein structure that is proposed for the modeling and digital predistortion of the dynamic nonlinear behavior of RF PAs. The remainder of this chapter is organized as follows. First a review of different well-established DPDs is presented in Section 2.2. In Section 2.3, the feedforward Hammerstein structure is proposed and its identification procedure is discussed. Then, the measurement setup is explained, and the measurement results of the feedforward model and other state-of-the-art models are compared in Section 2.4. In Section 2.5, the digital predistortion scheme and the experimental results are reported. Finally, in Section 2.6, a brief conclusion is presented.

2.2 Overview of single-band behavioral models/ DPDs

Early predistorter techniques in literature used memoryless structures, in which the predistorter compensates for the instantaneous nonlinear behavior of the PA [58]. This behavior was characterized in terms of amplitude modulation to amplitude modulation (AM-AM) and amplitude modulation to phase modulation (AM-PM) effects as a function of the instantaneous value of the PA's input signals. The Look-up-table (LUT) is the basic behavioral model for representing the memory less AM-AM and AM-PM, which are extracted from raw measured data, as follows:

$$x_{\text{out}}(n) = G(|x_{\text{in}}(n)|)x_{\text{in}}(n) \tag{2.1}$$

where x_{in} and x_{out} are the input and estimated model output. $G(.)$ is the instantaneous complex gain of the DUT.

However, as the bandwidth increases nowadays in the different wireless communication systems, the memory effects can no longer be neglected. Hence, the memory effects emulated by the PA are dependent on the operating conditions of the DUT and also signal dependent , such as signal statistics, bandwidth and PAPR. Therefore, in order to achieve a relevant good performance of the DPDs, memory effects should be taken into consideration [36, 59]. Therefore, different DPD architectures that compensate for nonlinear distortion and memory effects are proposed in literature [37–40]. Broadly they can be categorized into three-main categories which are: box-oriented models [60–68], polynomial or Volterra series models [70–79], and artificial neural-network models [80, 81].

The Volterra series is a general model to accurately characterize a dynamic nonlinear system [69–71], and is given by:

$$x_{\text{out}}(n) = \sum_{p=1}^{K} \sum_{i_1=0}^{M} \cdots \sum_{i_p=0}^{M} h_p(i_1, i_2, \cdots, i_p) \prod_{j=1}^{p} x_{\text{in}}(n - i_j) \tag{2.2}$$

where $h_p(i_1, i_2, \cdots, i_p)$ are the parameters (kernels) of the Volterra model, K is the nonlinearity order of the model, and M is the memory depth.

However, it results in a large number of coefficients that increases rapidly with the degree of the nonlinearity and memory depth of the system, which increases the computational complexity of the model. Therefore, the Volterra series is only limited for modeling mildly nonlinear systems. To overcome the computational complexity of the Volterra series, different reductions of the Volterra series have been proposed [76–79]. The memory polynomial (MP) [36] model is the most widely used pruned Volterra series in which all off-diagonal coefficients

of the Volterra kernels are set to zero, as follows:

$$x_{\text{out}}(n) = \sum_{m=0}^{M} \sum_{k=1}^{K} h_{km} x_{\text{in}}(n-m)|x_{\text{in}}(n-m)|^{k-1} \tag{2.3}$$

Even though, MP models are reduced Volterra models, but they still could result in over-sized models, due to the use of nonlinear polynomials in all branches, which will also translate into large number of coefficients. In fact, this translates into significant computational complexity and also may give rise to numerical stability problems when inverting the Vandermonde matrix to estimate the model coefficients. Furthermore, the poor condition of the Vandermonde matrix makes its pseudo-inverse calculation very sensitive to slight disturbances due to the large conditioning numbers of these matrices [73, 83]. Therefore, this makes these models impractical for real applications, i.e. when limited resources are available for field programmable gate array (FPGA) implementation [66, 82]. However, the Wiener and Hammerstein models [60, 61], which are composed of a cascade combination of a linear filter and a nonlinear function, are less complex models as they consume lower number of coefficients. Therefore, compared to the approaches previously proposed, these models have the great advantage of simplicity and are easier to implement in real-time systems. However, due to the structure of these models, they can only capture the linear memory effects. The linear memory effects are caused by the frequency response of the transmitter around the carrier frequency. In addition, the linear filters in the structure of these models, can not simulate the out-of-band spectrum regrowth caused by the nonlinear memory effects; such as trapping effects, impedance matching conditions at harmonic frequencies, and the envelope frequency response of the biasing circuit, using such a simple linear filter [84, 85].

Hence, the Wiener and Hammerstein models have limited performance. Therefore, dif-

ferent extensions for these models were proposed to enhance their performance [62–67], such as the augmented Hammerstein [62] and augmented Wiener [63] models, which consist of an extra branch of linear filter to compensate for the nonlinear memory effects due to the impedance variation of the bias circuits and harmonic loading of the power transistors. In [64], an Extended Hammerstein feedforward structure was also proposed using neural networks. Indeed, the twin nonlinear box model [65] was proposed, which is composed of two nonlinear boxes, one is a low-order polynomial function (constructed using a MP function) and the other is a look-up-table, which were placed in three different structures, to compensate for memory effects with strong static nonlinearity and was further extended in [66] to include a third box that add extra memory cross terms. Also, an Enhanced Hammerstein model was also proposed [67], which is composed of a weighted memoryless polynomial followed by a low-nonlinear order Volterra filter for predicting both the static and dynamic nonlinearities of RF PAs.

2.3 Feedforward Hammerstein Model

2.3.1 Model Architecture

In this section, a feedforward Hammerstein model, as hybrid box and polynomial based model, is proposed for the modeling of nonlinear PAs. The architecture of this model is shown in Fig. 2.1. It is consisted of two coupled loops, one is the signal cancellation loop, and the other is the distortion injection loop.

The main signal cancellation loop of this model is composed of a Hammerstein model, which is composed of a cascade connection of a static nonlinear box implemented as a LUT

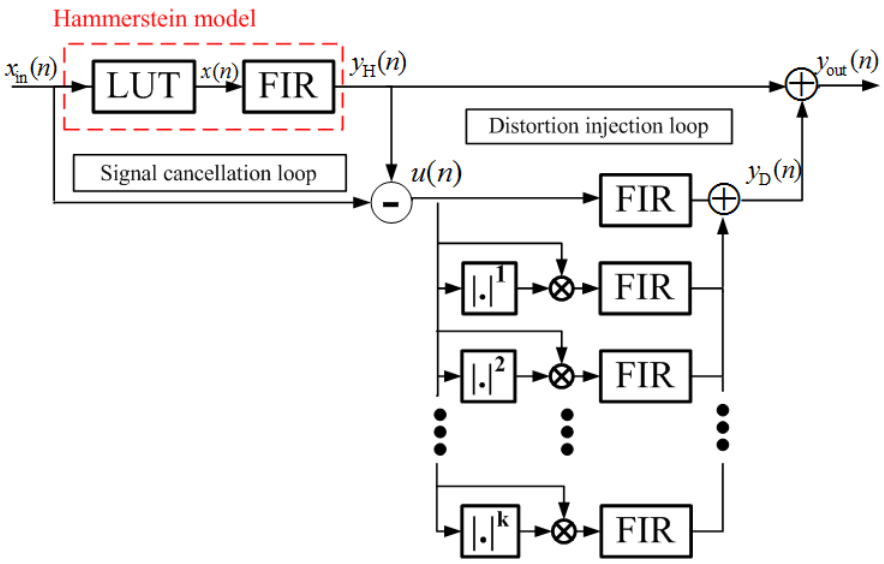

Figure 2.1: Feedforward Hammerstein model structure.

and a dynamic linear box implemented as a FIR filter, to characterize the static nonlinearities and the linear memory effects of the PA. Indeed, the distortion injection loop accurately models the inter-modulation distorted signal that results from subtracting the Hammerstein model output from the PA input. This distorted signal is modeled by a set of parallel linear filters.

The total model output $y_{\text{out}}(n)$ is given by:

$$y_{\text{out}}(n) = y_{\text{H}}(n) + y_{\text{D}}(n) \tag{2.4}$$

where $y_{\text{H}}(n)$ is the output of the first loop, i.e the Hammerstein model output, that is determined as follows : The output of the first LUT box, $x(n)$, can be described by the following:

$$x(n) = G(|x_{\text{in}}(n)|)x_{\text{in}}(n) \tag{2.5}$$

and the total Hammerstein model output, $y_{\text{H}}(n)$, is:

$$y_{\text{H}}(n) = \sum_{l=0}^{M_1} a_l x(n-l) \tag{2.6}$$

where $x_{\text{in}}(n)$, $y_{\text{H}}(n)$, and $x(n)$ are the input, estimated Hammerstein model output, and LUT box output, respectively. a_l and M_1 are the coefficients and the memory depth of the first FIR filter in the signal cancellation loop, respectively. $G(.)$ is the memoryless complex gain function of the LUT.

$y_{\text{D}}(n)$ is defined as the distortion injection loop output signal that is given by:

$$y_{\text{D}}(n) = \sum_{j=0}^{M_2} \sum_{i=0}^{K} b_{ij} u(n-j)|u(n-j)|^i \tag{2.7}$$

where M_2, K, and b_{ij} are the memory depth, nonlinearity order, and the coefficients of the FIR filter of the second loop, respectively; and $u(n)$ is the input of the distortion injection loop and is given by:

$$u(n) = x_{\text{in}}(n) - y_{\text{H}}(n) \tag{2.8}$$

2.3.2 Model Identification

The identification procedure of the feedforward model is composed of the following steps. First, the nonlinear memory less behavior of the device-under-test (DUT) is extracted by extracting the AM-AM and AM-PM curves from the measured data using polynomial fitting or smoothing algorithm [86] to identify the LUT static nonlinear box. Second, the input and output waveforms are de-embedded to identify the FIR filters. In this way, the problem of solving a nonlinear set of equations is alleviated [63]. Both, the FIR box of the first loop and the set of parallel filters FIRs of the second loop are identified simultaneously, using the traditional linear algorithms such as the least mean square (LMS) method. The simultaneous identification of the FIR filters of the two loops is formulated as a conventional

linear identification problem as follows:

$$\vec{y}_{\text{out}}(n) = \phi\vec{A} \tag{2.9}$$

where $\vec{y}_{\text{out}}(n)$ is the output vector of the model given by: $\vec{y}_{\text{out}}(n) = [y_{\text{out}}(n), y_{\text{out}}(n+1), \cdots, y_{\text{out}}(n+L)]^T$, where L is the length of the observation vectors used for the FIR coefficients identification, and $[.]^T$ is the complex transpose. In this work, L was set to 10,000 samples.

ϕ is the matrix constructed using the basis functions of the FIR filters of the two loops and their input signals and defined as follows:

$$\phi = \begin{bmatrix} x(n) & \cdots & x(n-M_1) & u(n) & \cdots & u(n-M_2)|u(n-M_2)|^K \\ x(n+1) & \cdots & x(n+1-M_1) & u(n+1) & \cdots & u(n+1-M_2)|u(n+1-M_2)|^K \\ \vdots & & \vdots & \vdots & \ddots & \vdots \\ x(n+L) & \cdots & x(n+L-M_1) & u(n+L) & \cdots & u(n+L-M_2)|u(n+L-M_2)|^K \end{bmatrix}$$

while $\vec{A}$ is the vector containing the FIR filters coefficients given by:

$$\vec{A} = [a_0, a_1, \cdots, a_{M_1}, b_{00}, b_{10}, \cdots, b_{K0}, b_{01}, \cdots, b_{KM_2}]^T \tag{2.10}$$

Subsequently, the coefficients $\vec{A}$ of the FIR filters are determined by the pseudo-inversing of the basis matrix ϕ as follows:

$$\vec{A}_{\text{LS}} = (\phi^H\phi)^{-1}\phi^H\vec{y}_{\text{out}} \tag{2.11}$$

where $[.]^H$ is the Hermitian transpose.

Compared to polynomial models, the identification of the proposed feedforward model requires one additional step that consists in de-embedding the data to construct the input signal of the FIR filters. However, this identification complexity is compensated by the use

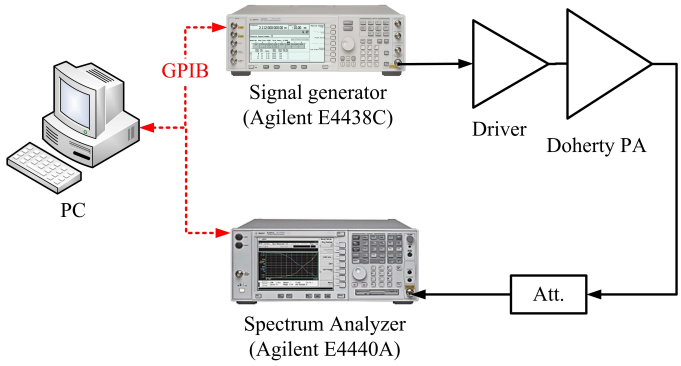

Figure 2.2: Measurement setup used for the DUT characterization.

of lower number of coefficients in the proposed model, as will be shown in the following sections.

2.4 Measurement Setup and Results

2.4.1 Experimental Setup

For measurement and experimental validation purposes, the proposed DPD model is implemented in a MATLAB/ Advanced Design System (ADS) platform and used to linearize a real PA. The model identification and validation steps are carried out using the measurement setup presented in Fig. 2.2.

The DUT is characterized using the standard instantaneous input and output baseband complex waveforms technique proposed in [87]. This experimental setup is composed of the DUT, a vector signal generator (Agilent, VSG4438C), a vector signal analyzer (Agilent, VSAE4440), and a computer. The computer is used to download, through a general purpose interface bus (GPIB), the signal into the VSG that drove the DUT with the RF input signal. The measured signal at the output of the DUT is attenuated and then down-converted and demodulated within the VSA. Data processing software is then used to identify the behavioral

model/ DPD and evaluate its performance, as well as identifying the predistortion function and synthesizing the predistorted signal. Finally, the signals are uploaded to the computer through the GPIB interface and processed using ADS to compute the different metrics to evaluate the model/ DPD performance. The time delay between the input and output waveforms is estimated and compensated for using the method described in [63].

The DUT used in this work for the performance assessment of the different models and DPDs, is a high-power, high-efficiency, laterally diffused metal oxide semiconductor (LDMOS) based Doherty PA that had a peak power of 300 watts and operated around 2,140 MHz. The frequency range in which the DUT is designed to operate in is from 2110 to 2170 MHz.

During the measurement steps, the DUT is operated at the same average power, which corresponded to an input power backoff of 10.6 dB. The input RF signal centered at 2,140 MHz, which is fed into the DUT and used to identify the different behavioral models/ DPDs, is a three-ON-carrier WCDMA signal of carrier configuration 111 (hereafter referred to as WCDMA 111). The WCDMA test signal had a bandwidth of 15 MHz, and a PAPR of 10.6 dB.

The input and output waveforms of the signal are sampled at 92.16 MHz, and only 10,000 samples out of the 184,320 samples of the input and output baseband waveforms are used for the model identification. During the model validation step, the entire waveform is used to assess the robustness of the different models.

2.4.2 Model performance assessment

The feedforward Hammerstein model was identified for the Doherty PA driven by a three-carrier WCDMA signal. The memory depth of the FIR in the Hammerstein structure of the first loop, is set to $M_1 = 3$. Herein, the the number of parameters of the LUT box corresponds to a 12 order polynomial. In order not to increase the number of parameters aggressively with the addition of the second loop that will consequently affect the model computational complexity, the model dimensions of the parallel branches of FIR filters were chosen based on a sweep method. They were set to $M_2 = 3$ and $K = 3$. The choice of these values was based on Fig. 2.3. As shown in Fig. 2.3(a), the normalized mean square error (NMSE) of the model is plotted versus M_2, which is the memory depth of the FIR filter of the second loop, for a single branch, i.e $K = 0$.

It is clear that the NMSE improves with more than 3 dB, with the addition of the filter in the second loop, than using only the Hammerstein model in the first loop, i.e $M_2 = 0$. Therefore, the memory depth M_2 is chosen to be 3, as a stable accuracy was obtained. Besides, the number of branches of the second distortion loop, which is denoted as K, was chosen by sweeping K versus the NMSE, for the given memory depth $M_2 = 3$, as illustrated in Fig. 2.3(b). Therefore, K was selected to be 3, as a degradation of the NMSE values was noticed beyond this value.

2.4.3 Comparison of the state-of-the-art models

Evaluation of the behavioral model performance of PAs and transmitters operating in their nonlinear region and exhibiting memory effects is a very critical task. In fact, an accurate behavioral model should mimic the response of the DUT inband, the contribution of the

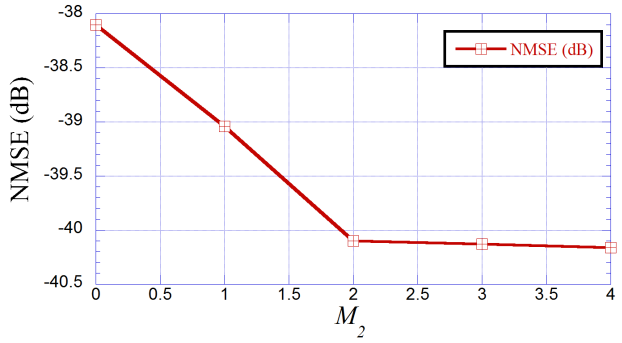

(a)

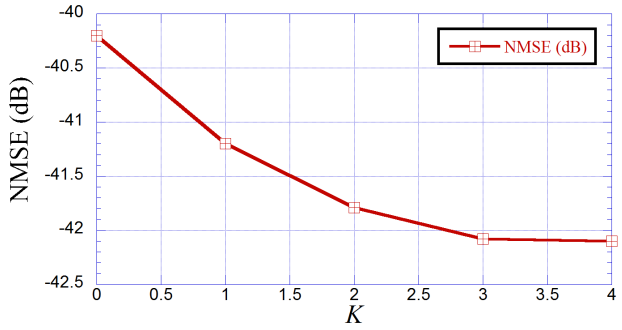

(b)

Figure 2.3: NMSE values versus (a) the memory depth M_2 at $K = 0$, (b) the number of parallel branches K at $M_2 = 3$.

static nonlinearity in adjacent channels, and the memory effects exhibited by the DUT. However, these three components of the DUT behavior have different intensity scales. In fact, the static nonlinearity in the adjacent channels is typically at least 25 dBc lower than the in-band power. Moreover, memory effects are often buried by the static nonlinearity. Accordingly, different metrics need to be considered to evaluate the accuracy of a behavioral model in predicting each of the three components of DUT behavior.

It has been shown that the NMSE based metrics are mainly dominated by the in-band response and, thus, do not accurately reflect the performance in the adjacent channels, where most of the nonlinear distortion takes place. The NMSE criterion is used in this work to evaluate the performance of behavioral models in predicting the behavior of the DUT

in-band [75, 88, 89]. The NMSE is given by:

$$\mathrm{NMSE_{dB}} = 10\log_{10}\left(\frac{\sum_{n=1}^{K}\left|y_{\mathrm{meas}}(n) - y_{\mathrm{est}}(n)\right|^2}{\sum_{n=1}^{K}\left|y_{\mathrm{meas}}(n)\right|^2}\right) \tag{2.12}$$

where $y_{\mathrm{meas}}(n)$ and $y_{\mathrm{est}}(n)$ are the measured and estimated output waveforms, respectively, and K is the number of samples of the output waveform.

To alleviate the limitation of the NMSE in quantifying and clearly differentiating the performance of several behavioral models, it is essential to use an additional figure of merit that precisely quantifies the performance in the adjacent channel. For this purpose, the adjacent channel error power ratio (ACEPR) which is a frequency domain metric can be used. The ACEPR is defined as the ratio between the power of the error signal $e(n)$ in an adjacent channel calculated in the time domain and the power of the measured output signal within the main channel [88]. The ACEPR can be calculated for both the lower and upper adjacent channels. However, in this work, the average ACEPR was considered. The average ACEPR is given by:

$$\mathrm{ACEPR} = \frac{1}{2}\left(\frac{\int_{\text{Lower adj ch.}}\left|E(f)\right|^2 df + \int_{\text{Upper adj ch.}}\left|E(f)\right|^2 df}{\int_{\text{main ch.}}\left|Y_{\mathrm{meas}}(f)\right|^2 df}\right) \tag{2.13}$$

where $Y_{\mathrm{meas}}(f)$ and $E(f)$ are the discrete Fourier transforms of $y_{\mathrm{meas}}(n)$, and the error signal $e(n)$, respectively, and the error signal is defined as:

$$e(n) = y_{\mathrm{meas}}(n) - y_{\mathrm{est}}(n) \tag{2.14}$$

Also, the computational complexity of these models is compared in terms of the number of coefficients utilized by the models as well as the number of floating point operations (FLOPs).

Operation	number of FLOPs
Conjugate	0
Delay	0
Real addition	1
Real multiplication	1
Complex addition	2
Complex-real multiplication	2
Complex-complex multiplication	6
$\|.\|^2$	3
Square-root	$6 \sim 8$

Table 2.1: Number of FLOPs for different operations

In DSP hardware, the computational effort is mainly spent on additions, subtractions, and multiplications. FLOPs is a measure of the number of these mathematical operations, so it can also be used as a measure of running computational complexity [82]. Table 2.1 shows the operation-FLOP conversion used as shown in [82].

The WCDMA 111 signal was used for the assessment of the models for the Doherty PA. The results of the NMSE and ACEPR metrics for the proposed model and the other compared models, which are the MP model, Hammerstein model, and the Augmented Hammerstein model, are reported in Table 2.2. Also, the number of coefficients and the number of FLOPs are reported for applying a fair comparison between these models in terms of the computational complexity.

These results illustrate the accuracy of the proposed model by clearly improving the ACEPR with around 4 dB, than the well established MP model (with 10 polynomial order, 3 memory delay taps, and both the even- and odd-terms are considered to improve the modeling accuracy [74]), 6 dB than the Hammerstein model, and almost 3 dB than the augmented Hammerstein model.

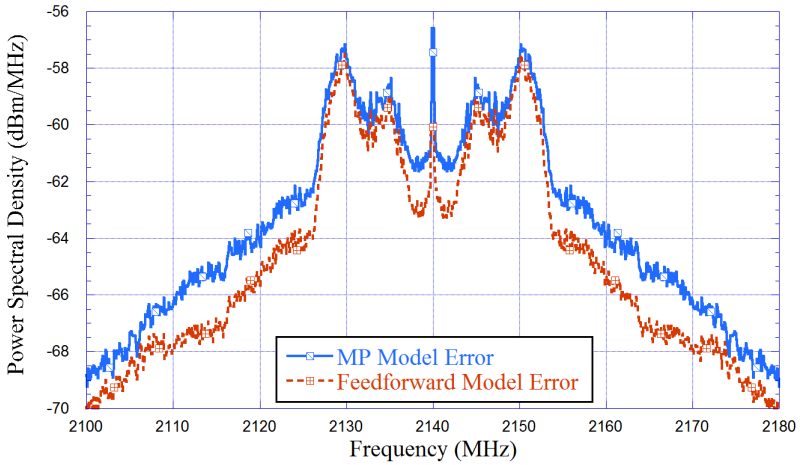

Figure 2.4: Error Spectra of the MP model and Feedforward model.

Indeed, the ACEPR is mostly dominated by the out-of-band errors; therefore the improvement achieved by the feedforward model is due to the addition of the second distortion injection loop that helped to do a better characterizing of the dynamic nonlinear effects of the intermodulation distortions in the out-of-band regions, while maintaining a reasonable number of coefficients.

It can be also concluded from Table 2.2, that the NMSE of the feedforward model is slightly improved than the other models, since it is mostly impacted by the in-band distortions, which can be accounted for by the linear filter in the Hammerstein model structure. Hence, that further validates what was mentioned earlier in the paper, that the conventional Hammerstein model can predict only the linear memory effects.

In terms of running computational complexity, Table 2.3 shows a comparison of the computational complexity of the different models. The MP model is the most computational complex model in terms of the number of coefficients as well as the number of Flops, due to the use of constant nonlinearity order in all branches. The Hammerstein model is the least complex model, but has the worst accuracy, as the nonlinear memory effects are not

Model ⇓	NMSE (dB)	ACEPR (dB)
Feedforward model	−42.1	−52.9
MP model	−39.8	−48.4
Hammerstein model	−38.1	−46.5
Aug. Hammerstein model	−40.2	−49.7

Table 2.2: Performance comparison of the models

characterized. The Augumented Hammerstein model and the feedforward model are more computationally-efficient than the MP model, as the characterization of the highly nonlinear static (modeled by the LUT) and the mildly nonlinear dynamics (modeled by the FIR filters), is done in two steps. The slight increase in the number of coefficients and Flops of the proposed feedfoward model than the Aug. Hammerstein model, due to the added distortion loop, is compensated for with the accuracy improvement in terms of NMSE and ACEPR.

To further validate the accuracy of the proposed model, the spectra of the error between the measured and estimated outputs of the MP model and proposed model, are plotted in Fig. 2.4. This figure further confirms the ability of the proposed model to accurately predict the measured PA spectrum, due to the addition of the distortion injection loop that accounts for the nonlinear memory effects of the DUT (the slight discrepancies between the two curves toward the edges is due to the limited bandwidth of the VSA 80 MHz). Therefore, the output of the model; which is the summation of the outputs of the two loops, accounts for both linear and nonlinear memory effects and will consequently allow for better modeling accuracy and mimicking of the dynamic nonlinear effects of the DUT.

Model ⇓	No. of Coefficients	No. of Flops
Feedforward model	28	211
MP model	40	337
Hammerstein model	16	155
Aug. Hammerstein model	20	188

Table 2.3: Computational complexity comparison of the models

2.5 Digital Predistortion Results

The general predistortion concept is that the DPD is placed upstream of the PA, and has ideally the exact inverse characteristics of the PA, in order to linearize the whole system. The feedforward Hammerstein structure shown in the previous sections can be utilized as a PA model as well as a digital predistorter.

In the latter, the indirect learning architecture is employed as shown in Fig. 2.5. The indirect learning is a conceptually approach where a learning loop is closed around the PA system, where the input and output measurements of the PA are used for deducing its inverse model, and the parameters of the PAs post-inverse are identified, which is then directly copied and used for predistortion [73]. The baseband predistorter input is denoted by $x(n)$, the predistorter output/ baseband PA input is denoted by $u(n)$, and the baseband PA output is denoted by $y(n)$. The identification procedure of the DPD is similar to the previously explained procedure, with replacing the input with $y(n)/G$, where G is the small-signal gain of the PA, and the output is $\tilde{u}(n)$.

The proposed linearization DPD was tested on a highly power Doherty amplifier, and its performance was compared to different conventional approaches. The DUT was driven by a

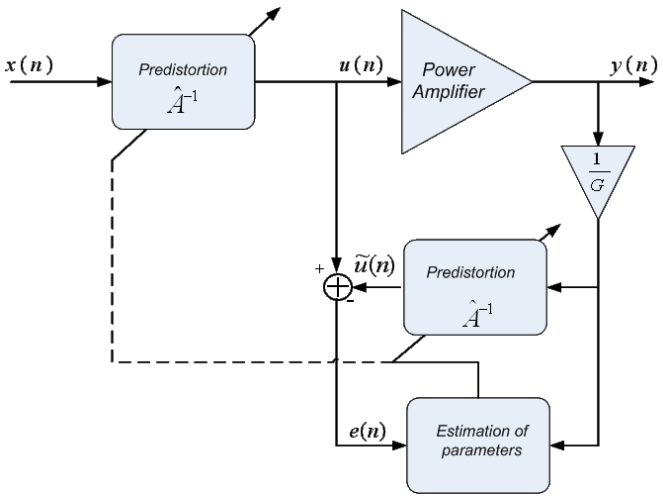

Figure 2.5: General Indirect learning architecture Predistorter scheme.

three-carrier WCDMA signal. The results shown herein are for the measured spectra at the output of the DUT after employing different reverse models.

In order to perform a comparative study on the different DPDs behavior proposed in literature, different DPD structures were implemented, which are the MP, Augmented Hammerstein, and a static LUT DPDs.

The performance of the feedforward DPD was compared to these DPDs, and the results are reported in Fig. 2.6. The figure also shows the spectrum without any DPD employed and the spectrum of the input WCDMA signal. The different DPD functions were able to suppress the spectrum regrowth at the output of the DUT, where the spectral regrowth at the output with no DPD employed is almost -30 dB higher than the in-band spectral level. As shown in the figure, the feedforward DPD has achieved a superior performance than the other DPDs, which further validates the accuracy of the proposed structure. The non-symmetry of the spectrum shown in Fig. 2.6 is induced due to the residual distortion and inherent impairment of the modulator inside the generator.

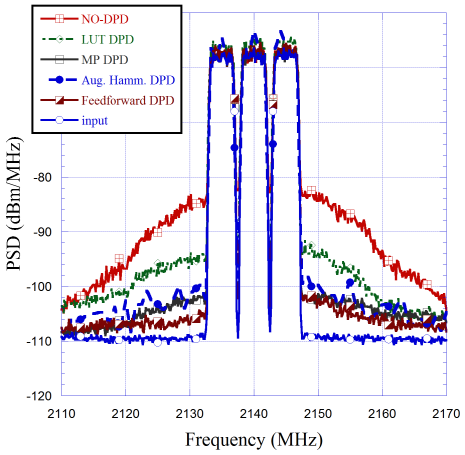

(a)

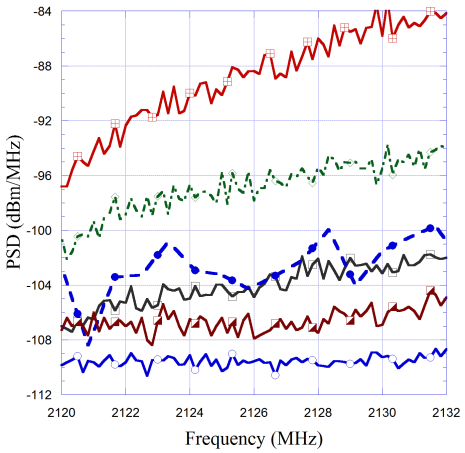

(b)

Figure 2.6: Measured spectra at the output of the linearized DUT. (a) the full spectrum, (b) zoomed version.

2.6 Conclusion

In this chapter, an overview of the characterization and modeling of the static and nonlinear behavior of single-band PAs. Then a feedforward Hammerstein structure was proposed for the behavioral modeling and digital predistortion of the PAs / wireless transmitters. The proposed structure consists of a Hammerstein model in its first signal cancellation loop and it also consists of a second distortion injection loop for the better fitting and characterizing

of the dynamic nonlinear effects of the distortions caused by the PA. The second loop captures the nonlinear memory effects that are not characterized by the Hammerstein model in the signal cancellation loop, due to the structure of the model. In comparison with other state-of-the-art-models, it showed better ACEPR and better mimicking of the measured PA spectrum.

Also, as it was tested for linearization of a highly nonlinear Doherty PA. It showed superior performance in suppressing the spectral-regrowth than the other DPDs. The characterization of the distorted signal through a separate loop enhanced the performance of the model/ DPD and showed better accuracy in mimicking the dynamic behavior of the PA with only adding very limited extra complexity than the conventional Hammerstein model. Since, the dimensions of the extra blocks in the distortion loop are tailored separately, in order to choose the optimal dimensions at limited extra complexity cost.

Chapter 3

A Generalized Twin-Box Model for Compensation of Transmitters RF Impairments

3.1 Introduction

A current trend in the implementation of future wireless radio transceivers is to use the direct-conversion or the low-IF transmitter architectures [7]. A schematic of direct conversion transmitter and a low-IF transmitter are shown in Fig. 3.1. The RF PA is the last component in the transmitter chain and the main source of distortion in the transmitter chain. The modeling and linearization of the PA distortion was discussed in Chapter 2. However, there are still a number of practical issues that contribute to signal deterioration that has to be compensated for before these transmitter architectures can be fully implemented in future wideband flexible transceiver units. In both architectures, many transceiver functions have been moved from analog parts towards the digital parts, thus enabling low-cost, simple, highly integrable, and less power consuming transceiver units [7]. However, one practical problem is the sensitivity of such simplified analog RF front-ends to imperfections of the used radio electronics.

Both of the direct conversion and low-IF transmitters are based on analog complex in-phase/quadrature (I/Q) up- and down-conversion which makes them vulnerable to amplitude and phase mismatch between I- and Q-branches, as well as LO leakages [10]. Perfectly balanced I/Q mixing (equal gain in the I- and in the Q-branch, exactly 90° phase shift be-

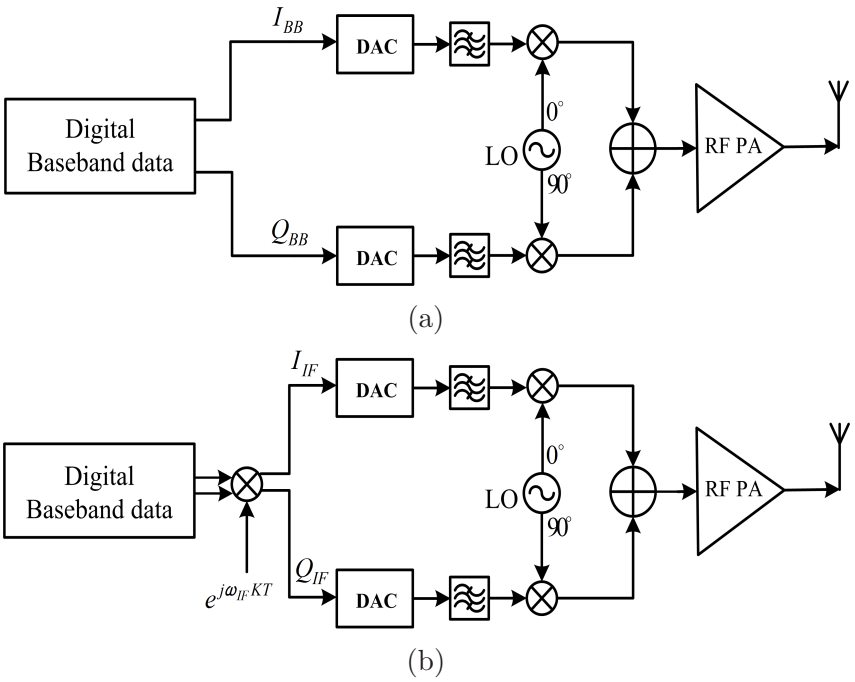

Figure 3.1: (a) Direct conversion transmitter. (b) Low-IF transmitter.

tween both phases of the oscillator) leads to an infinite rejection of the image signal, hence no costly image rejection filter is required. However, due to hardware limitations, a perfectly balanced analog I/Q mixer is not feasible, resulting in a limited suppression of the image signal. A radiation of the unwanted residual image is critical, since it might violate the compliance with the spectral mask of the desired communications standard. As a result, there is cross-talk between mirror frequency interference (MFI) [14], which yields self-interference or adjacent channels interference, depending on the selected transmitter topology.

Many methods have been proposed for the digital compensation of the I/Q imbalance problem in [14,54,90–95]. In [14,54,90], frequency dependent linear distortion compensation methods are proposed. In [91], an approach for blind estimation and compensation of I/Q imbalance for wideband receivers was proposed, where the parameter estimation does not depend on the structure of the received signals and no training signals are needed. A nonlin-

ear Volterra model for the characterization of the nonlinear behavior of the I/Q modulators is presented in [92]. In [94, 95], the joint compensation of the I/Q impairments as well as the nonlinear distortion of the PA is presented.

In this chapter, a complexity-reduced compound DPD is proposed. The proposed DPD is generic in the sense that it can adapt to any changes in the input data even in the presence of modulator I/Q imperfections [96]. The robustness of the proposed compound DPD is verified by linearizing a nonlinear Class AB PA in the presence of hardware impairments, and compared to other state-of-the-art DPDs.

The remainder of the chapter is organized as follows: In Section 3.2, different models of quadrature I/Q modulators are presented. The joint modeling of the PA and modulator imperfections is discussed in Section 3.3. The proposed Generalized Twin-box model is presented in Section 3.4. Section 3.5 presents the identification procedure for the proposed model. The experimental setup and the measurement results are demonstrated in Sections 3.6 and 3.7, respectively. Finally, a brief conclusion is presented in Section 3.8.

3.2 I/Q imbalance modeling

Ideally, the in-phase (I) and quadrature (Q) channels of a quadrature communication system are orthogonal to each other. However, due to implementation imperfections, there always exist gain and phase imbalances that destroy the orthogonality between these two channels and degrade the performance of the communication system. Figs. 3.2a and 3.2b depict the gain response (AM-AM) and phase response (AM-PM) of the transmitter including the PA. The quadrature modulator used has gain imbalance of 1 dB, phase imbalance of 3 degrees,

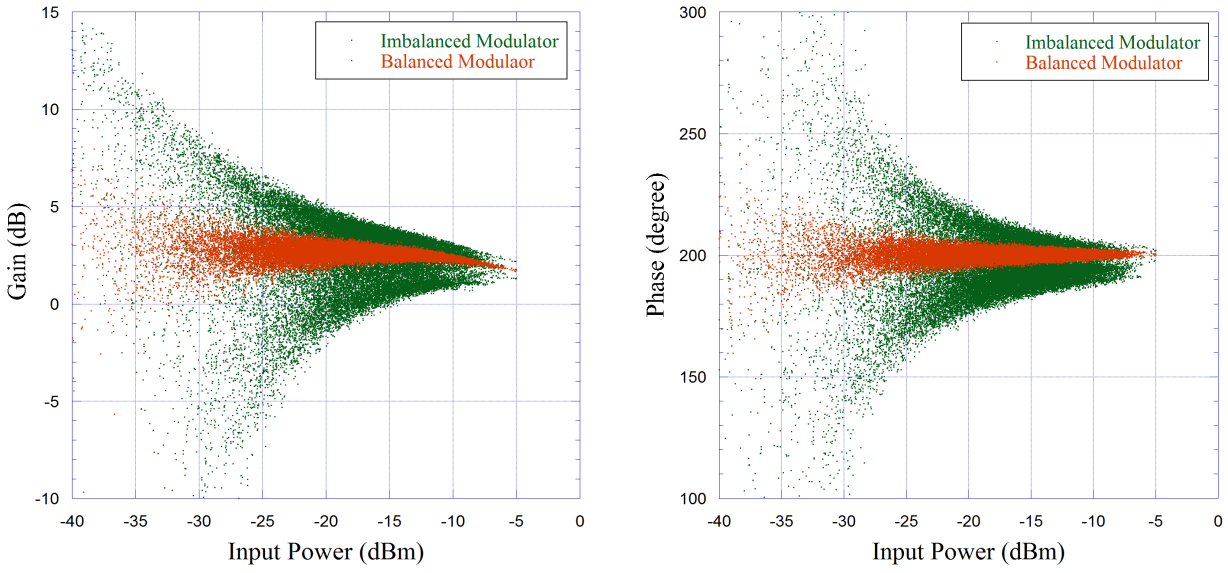

(a) (b)

Figure 3.2: Effect of modulator imperfections on PA performance: (a) AM/AM (b) AM/PM.

and DC offsets of 3% and 5% for I and Q, respectively. From these figures, it is clear that both the characteristics are drastically changed with the introduction of I/Q imperfections and DC offsets in the modulator.

The gain and phase modelling is a complex issue. Considering a quadrature modulator of g dB gain imbalance and ϕ degree phase imbalance, the discrete-time samples of the RF signal $x_{\mathrm{m}}(n)$ at the output of modulator is given by:

$$x_{\mathrm{m}}(n) = \alpha_1 I(n)\cos(\omega n + \theta_1) - \alpha_2 Q(n)\sin(\omega n + \theta_2) \tag{3.1}$$

where $I(n)$ and $Q(n)$ are the in-phase and quadrature components of the baseband signals; ω is the carrier frequency; $\dfrac{\alpha_2}{\alpha_1} = 10^{\left(\frac{g}{20}\right)}$ and $\phi = \theta_2 - \theta_1$.

By using the trigonometric identity, (3.1) can be expressed as:

$$x_{\mathrm{m}}(n) = I_{\mathrm{m}}(n)\cos(\omega n) - Q_{\mathrm{m}}(n)\sin(\omega n) \tag{3.2}$$

In case of gain and phase imbalances, the general expressions of $I_{\mathrm{m}}(n)$ and $Q_{\mathrm{m}}(n)$ are

given by:

$$\begin{cases} I_{\mathrm{m}}(n) = & \alpha_1 \cos(\theta_1) I(n) - \alpha_2 \sin(\theta_2) Q(n) \\ Q_{\mathrm{m}}(n) = & \alpha_1 \sin(\theta_1) I(n) + \alpha_2 \cos(\theta_2) Q(n) \end{cases}$$

In the absence of modulator imperfections, i.e. $\alpha_1 = \alpha_2$ and $\phi = 0$, $I_{\mathrm{m}}(n)$ and $Q_{\mathrm{m}}(n)$ are given by:

$$\begin{cases} I_{\mathrm{m}}(n) = & I(n) \\ Q_{\mathrm{m}}(n) = & Q(n) \end{cases}$$

Using the matrix notation, the distortion caused by the I/Q imbalance can be modeled as:

$$\begin{bmatrix} I_m(n) \\ Q_{\mathrm{m}}(n) \end{bmatrix} = \begin{bmatrix} \alpha_1 \cos(\theta_1) & -\alpha_2 \sin(\theta_2) \\ \alpha_1 \sin(\theta_1) & \alpha_2 \cos(\theta_2) \end{bmatrix} \begin{bmatrix} I(n) \\ Q(n) \end{bmatrix}$$

3.2.1 Complex I/Q channel model

The frequency-dependent gain/phase imbalance comes from the frequency-dependent behavior of the analog components in the I and Q paths. In order to model the I and Q channels and the cross coupling channels between them, different filter structure models were proposed in [54, 91].

Therefore in a direct conversion transmitter, the baseband output of the modulator is is based on four real filters h_{11}, h_{21}, h_{12}, and h_{22}. The complex I/Q channel model [91] is given as:

$$y_{\mathrm{mod}}(n) = \sum_{m=0}^{M} [h_{\mathrm{i}}(m) x_i(n-m) + h_{\mathrm{q}}(m) x_q(n-m)] + d \tag{3.3}$$

where x_i and x_q are the real and imaginary parts of the baseband input signal $x(n)$, and, $y_{\mathrm{mod}}(n)$ is the modulator output, d is the DC offset ($d = d_i + jd_q$). h_{i} and h_{q} are the coefficients of the I and Q filters. These filters can be represented in terms of four real filters

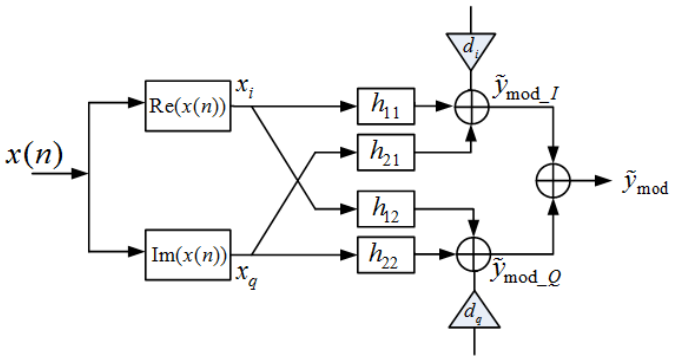

Figure 3.3: Schematic of the modulator.

h_{11}, h_{21}, h_{12}, and h_{22}, as shown in Fig. 3.3 as follows, $h_{\mathrm{i}} = h_{11} + jh_{21}$ and $h_{\mathrm{q}} = h_{12} + jh_{22}$. The filters are supposed to have the same length M.

3.2.2 Direct / Image channel model

Another model for the I/Q modulator is the Direct/ Image model in terms of the signal $x(n)$ and its complex conjugate $x^*(n)$, that can are related to $x_i(n)$ and $x_q(n)$ as: $x_i(n) = \dfrac{x(n) + x^*(n)}{2}$ and $x_q(n) = \dfrac{x(n) - x^*(n)}{2j}$.

Therefore, the direct/image filter structure model is presented as:

$$y_{\mathrm{mod}}(n) = \sum_{m=0}^{M} [h_{\mathrm{D}}(m)x(n-m) + h_{\mathrm{I}}(m)x^*(n-m)] + d \tag{3.4}$$

where $x(n)$ and $y_{\mathrm{mod}}(n)$ are the input and estimated output of the modulator, respectively. d is the DC offset of the modulator, and $(.)^*$ denotes the complex conjugate, where $x^*(n)$ can be seen as the image of $x(n)$. While, h_{D} and h_{I} are the coefficients of the direct and image filters of length M and are related to the filter coefficients h_i and h_q as follows: $h_D = \dfrac{h_{\mathrm{i}} - jh_{\mathrm{q}}}{2}$ and $h_I = \dfrac{h_{\mathrm{i}} + jh_{\mathrm{q}}}{2j}$.

3.3 Compensation of PA nonlinearity and I/Q imbalance imperfections

3.3.1 A two-step predistortion and I/Q compensation approach

As a solution to problem imposed by modulator imperfections, the techniques in [14, 54, 90–92] focus on mitigating I/Q modulator/demodulator errors only, with the assumption that correction for this enables the successful use of any digital predistorters. Fig. 3.4 illustrates a general structure of the two-step baseband predistortion system and I/Q estimation and compensation modules. As mentioned in the previous section, we use direct up-conversion in the transmitter chain, shows such a two-step characterization and compensation process. During the modulator impairment compensation process, and a one-stage downconverter and digital demodulator in the feedback path. Additional baseband processing of the input signal $u(n)$ in the transmitter includes predistortion and I/Q compensation, whose outputs are denoted by $z(n)$ and $x(n)$, respectively. During the initialization phase, the predistorter and I/Q compensator are bypassed: i.e., $x(n) = z(n) = u(n)$. We also bypass the PA and acquire the direct upconverter output in baseband, i.e., $y(n)$. Based on $x(n)$ and $y(n)$, we can estimate the parameters of the channel model and calculate the coefficients of the I/Q compensator (shown by the dashed loop). After the I/Q compensator is activated, we put the PA back in the loop and start training the predistorter (shown by the solid loop).

However, the separate processing of the PA and modulator impairments requires extra RF hardware compared to just a PA predistorter in the form of either an RF switch or a second feedback loop. Moreover, this two-step compensation technique is effective only with the condition that the Tx characteristics do not change with the environment, which is an

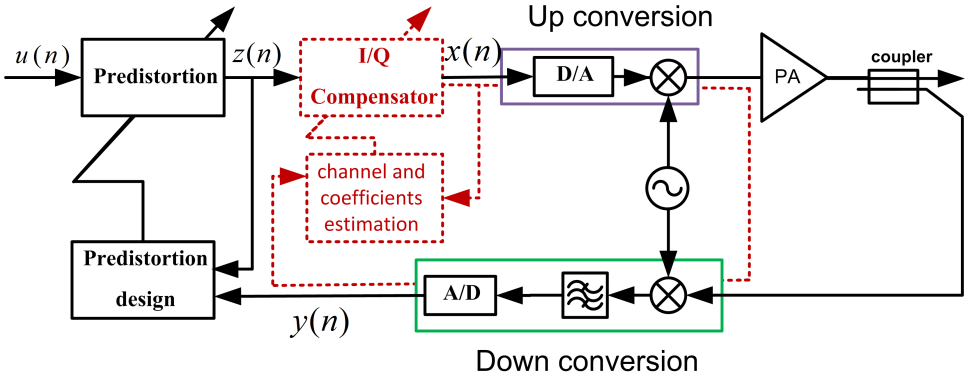

Figure 3.4: Successive compensation for modulator imperfections and PA nonlinearity.

impractical assumption.

3.3.2 A single-step predistortion and I/Q compensation approach

Some recent attempts at joint compensation have been reported with memoryless PA model [94], which is not fair assumption in the case of fast varying envelope signals such as wideband WiMax and LTE signals. Therefore, in [95] a Parallel-Hammerstein (PH) based approach, which can be qualified as true joint compensation for a simulated environment. However, the complexity of this model is increased due to the added conjugate branches, as the number of complex-valued parameters is more than doubled. The total output of the PA and modulator compound model [95] is given by:

$$y_{\text{pa,mod}}(n) = \sum_{m=0}^{M} \left[\sum_{k=1}^{N_1-1} a_{mk} \varphi_{mk}(x(n)) + \sum_{k=1}^{N_2-1} b_{mk} \bar{\varphi}_{mk}(x^*(n)) \right] + d \tag{3.5}$$

where, φ_{mk} and $\bar{\varphi}_{mk}$ are the nonlinear basis functions of the MP model [16] of inputs $x(n)$ and its complex conjugate $x^*(n)$, respectively; N_1 is the nonlinear order of the signal branch and N_2 for the complex image branch of memory depth M; and a_{mk} and b_{mk} are the two sets of coefficients for the MP model of input $x(n)$ and the image MP model of input $x^*(n)$, respectively.

The two basis functions φ_{mk} and $\bar{\varphi}_{mk}$ are defined as follows:

$$\begin{aligned} \varphi_{mk} &= x(n-m)|x(n-m)|^{k-1} \\ \bar{\varphi}_{mk} &= x^*(n-m)|x(n-m)|^{k-1} \end{aligned} \tag{3.6}$$

The compound model for the PA dynamic nonlinearity and I/Q impairments compensation in a single-band TX can, therefore, be viewed as a parallel-Hammerstein model [95] structure of two inputs, which are the signal and its complex conjugate signal, as shown in Fig. 3.5.

Therefore, the compound model for the PA dynamic nonlinearity and I/Q impairments compensation in a single-band transmitter, can be viewed as a PH model structure of two inputs, which are the signal and its conjugate image. However, the compound PH model that compensates for the I/Q imperfections as well as the PA nonlinearity, will further increase the dimensionality of the model, by adding a parallel MP structure, and applying the signals conjugate image as input to this parallel structure. The dimensionality of the model in terms of the number of coefficients can indicate the number of complex-valued multiplications per sample done in the linear filters. In the compound structure of the PH model, the input samples share the same basis functions for the nonlinear part (excluding complex conjugation, which is just a sign change) [95] as shown in (3.5), but each sample require extra complex-valued multiplications for the memory effect part. So, the number of complex multiplications in general for the whole function will be doubled if $N_1 = N_2$. Also, the number of floating points is proportional to the number of coefficients of the model. Indeed, this severe increase in the number of coefficients will increase the computational load and the numerical stability of the model during the identification step, and will further affect the performance of the model.

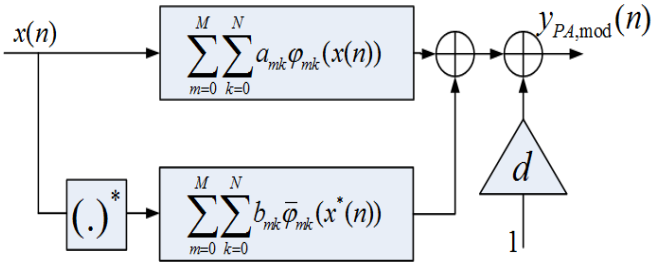

Figure 3.5: Schematic of the joint predistorter of PA nonlinearity and I/Q impairments for a single-band PA.

3.4 Proposed Model

A complexity-reduced Generalized Twin-box model is proposed for the modeling and compensation of the PA distortion as well as the I/Q modulator impairments. The model is inspired by the forward Twin-box nonlinear Box model (FTNTB) in [65]. It is also composed of two cascaded nonlinear boxes. The first Box is implemented as dual parallel branches of simplified Volterra filters that include second-order cross-terms as shown in Fig. 3.6. The second box is composed of a static nonlinear function that can be implemented as a LUT or static polynomial function. The dual branches of simplified Volterra filters [77], where only the second-order cross-terms are considered, i.e., the products of the signal and the delayed envelope at a different time delay, and with an arbitrary polynomial order, is given by:

$$u(n) = \left[\sum_{k=0}^{M} h_k x(n-k) + \sum_{k=0}^{M}\sum_{j=0}^{l_1} h_{jk} x(n-k)|x(n-k-j)|\right] + \left[\sum_{k=0}^{M} \bar{h}_k x^*(n-k) + \sum_{k=0}^{M}\sum_{j=0}^{l_1} \bar{h}_{jk} x^*(n-k)|x(n-k-j)|\right] + d \tag{3.7}$$

where $x(n)$ and $u(n)$ are the input and estimated output of the nonlinear (NL) filters, respectively. M is the finite memory length of the input signal, while l_1 is the time delay lag of the envelope signal. $h_{(.)}$ designates the model coefficients.

In this way, the frequency dependent behavior of the I/Q modulator is characterized through the mild nonlinear Volterra filters, which offers more flexibility in modeling the memory effects and thus reduces the model complexity. Hence, the PA nonlinear behavior is characterized through the second box, without the need to duplicate the static nonlinear function. Thus, the number of complex multiplications is much reduced than the PH model. The dual-branch Volterra filters herein are linear in terms of coefficients. Therefore, linear estimation techniques; such as least squares (LS) or recursive least squares (RLS) can be applied for coefficients estimation. In this work, the LS estimation was used for coefficients estimation, where the output signals of this box are de-embedded for identification of the second static box as will be shown in the next section.

The second box which is a highly nonlinear static function is implemented herein as a LUT, given as:

$$y(n) = G(u(n)) \times u(n) \tag{3.8}$$

where $u(n)$ and $y(n)$ are the input and output signals of the second box, respectively. $G(.)$ is the memoryless complex gain functions of the LUT.

The LUT can be identified using moving average approaches [86] or polynomial fitting as follows:

$$G(u(n)) = \sum_{k=1}^{K} s_k |u(n)|^{(k-1)} \tag{3.9}$$

where K is the nonlinearity order of the complex nonlinear gain of the LUT; s_k is the set of the coefficients.

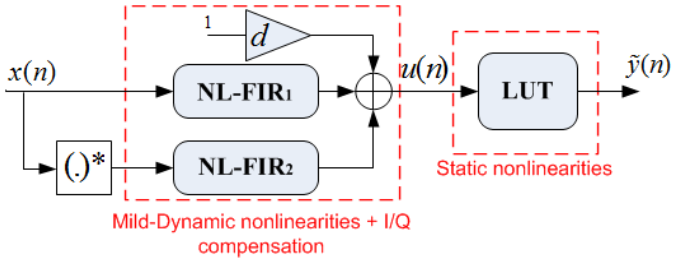

Figure 3.6: Schematic of the proposed model.

3.5 Identification Procedure

The identification procedure of the mildly nonlinear dynamic function implemented using the Volterra filters is done using least squares algorithm. Both filters of the main and conjugate branches are identified simultaneously as follows:

$$\vec{u} = \Phi \cdot \vec{h} \tag{3.10}$$

where $\vec{u}$ is the estimated output vector of the two dynamic nonlinear Volterra filters, Φ is the matrix constructed using the basis functions of these two polynomial boxes and their input signals, and $\vec{h}$ is the vector containing the polynomial boxes coefficients. These vectors are defined as follows:

$$\vec{u} = [u(1), u(2), \cdots, u(L)]^T \tag{3.11}$$

and

$$\vec{h} = \left[h_0, h_1, \cdots, h_M, h_{00}, \cdots, h_{Ml_1}, \bar{h}_0, \bar{h}_1, \cdots, \bar{h}_M, \bar{h}_{00}, \cdots, \bar{h}_{Ml_1}, d\right]^T \tag{3.12}$$

where L is the length of the input samples used for identification. The matrix Φ is analyzed into sub matrices as follows:

$$\Phi = [\Phi_{(x)}\ \Phi_{(x^*)}\mathbf{1}] \tag{3.13}$$

where $\Phi_{(x)}$ and $\Phi_{(x^*)}$ are the sub-matrices constructed using the two basis functions, given as:

$$\Phi_{(x)} = \left[\vec{\phi}(x(1)), \vec{\phi}(x(2)), \cdots, \vec{\phi}(x(L))\right]^T \tag{3.14}$$

where $\vec{\phi}(x(n))$ is given by:

$$\begin{aligned}\vec{\phi}(x(n)) =&[x(n), x(n-1), \cdots, x(n-M),\\ &x(n)|x(n)|, \cdots, x(n)|x(n-l_1)|,\\ &x(n-1)|x(n-1)|, \cdots\cdots, x(n-M)|x(n-M-l_1)|]\end{aligned} \tag{3.15}$$

where L is the length of the training sequence of 10000 samples.

Similarly, $\Phi_{(x^*)}$ can be expressed as follows:

$$\Phi_{(x^*)} = \left[\vec{\phi}(x^*(1)), \vec{\phi}(x^*(2)), \cdots, \vec{\phi}(x^*(L))\right]^T \tag{3.16}$$

and $\vec{\phi}(x^*(n))$ is given by:

$$\begin{aligned}\vec{\phi}(x^*(n)) =&[x^*(n)x^*(n-1), \cdots, x^*(n-M),\\ &x^*(n)|x(n)|, \cdots, x^*(n)|x(n-l_1)|,\\ &x^*(n-1)|x(n-1)|, \cdots\cdots, x^*(n-M)|x(n-M-l_1)|]\end{aligned} \tag{3.17}$$

The least-square solution $\vec{h}_{\mathtt{LS}}$ is, therefore, obtained by using the pseudo-inverse of the basis matrix Φ as follows:

$$\vec{h}_{\mathtt{LS}} = pinv(\Phi) \centerdot \vec{u} \tag{3.18}$$

where $pinv(\Phi) = \left(\Phi^H \Phi\right)^{-1} \Phi^H$ is the pseudo-inverse of the matrix Φ, and $[.]^H$ is the Hermitian transpose.

While, The LUT functions given by (3.9) are identified using polynomial fitting, where the coefficients s_k are extracted using least squares.

The proposed model has added identification complexity than the MP and PH models. The identification of the proposed model is done in two steps: the first step is the identification of the parallel dual-input Volterra filters; and, the second step is the de-embedding of the output signals for the identification of the memoryless nonlinear behavior of the LUT. On the other hand, the identification of the MP and PH models is done in only one step. This added identification step adds an extra identification complexity to the proposed model. However, this additional identification complexity is compensated for with the improved performance of the proposed model and the significant reduction in computational complexity represented by the number of coefficients, than the PH model as will be shown in the next sections. Also, this identification complexity can be considered to be minor, and not as important as the computational complexity, since the identification step in this work is done offline.

3.6 Measurement Setup

For measurement and experimental validation purposes, the proposed DPD model is implemented in a MATLAB platform and used to linearize a real PA. The model identification and validation steps are carried out using the measurement setup presented in the previous chapter.

The DUT used in this chapter for the performance assessment of the different models and DPDs, is a Class AB PA working at center frequency of 1.96 GHz.

The experimental setup was set to work at two cases:

Case I: Balanced modulator: gain imbalance = 0, phase imbalance= 0, I offset = 0, Q offset = 0.

Case II: Imbalanced modulator: gain imbalance = 1 dB, phase imbalance = 3 degree, I offset = 3%, Q offset = 5%.

3.7 Measurement Results

Two scenarios were used for the validation of the model. The first one with baseband signals and the second one is with low-IF signals.

3.7.1 Scenario 1

The input signal used to evaluate the performance of the different studied models is a WiMAX signal which was characterized by a bandwidth of 10 MHz, 16-QAM data modulation, a cycle prefix of 1/8, 500,000 samples and a sampling frequency $f_s = 92.16$ MHz.

The proposed model was used to compensate jointly for I/Q imbalance and PA nonlinearity, and its performance was evaluated in comparison with the MP model [36] and PH model [95]. For out-of-band evaluation, a comparison between the different models was carried out, in terms of Power spectral Density (PSD) for the two cases of balanced and imbalanced modulators. From Fig. 3.7a, it can be noticed that the three models were able to compensate for the out-of-band distortions in the case of balanced modulator.

However, the proposed predistorter showed a clear improvement over the MP and PH predistorters in the presence of I/Q imbalance in the modulator. As shown in Fig. 3.7b, the MP model is incapable of mitigating the out-of band distortion in the presence of I/Q

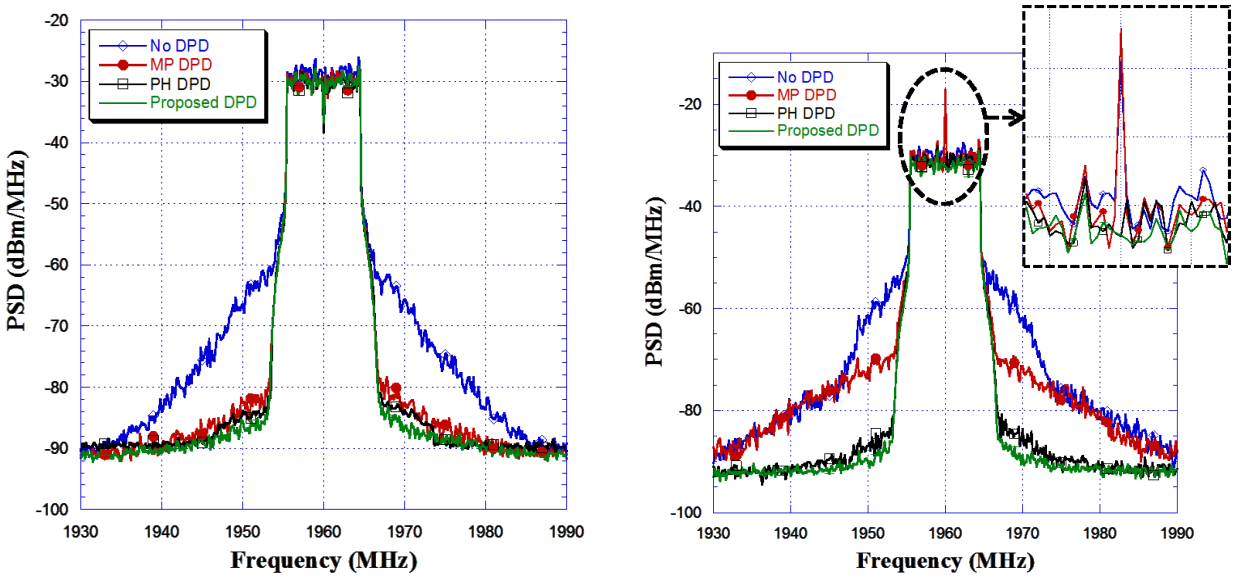

(a) (b)

Figure 3.7: Measured PSDs with and without DPD (a) Case I (b) Case II for Scenario 1.

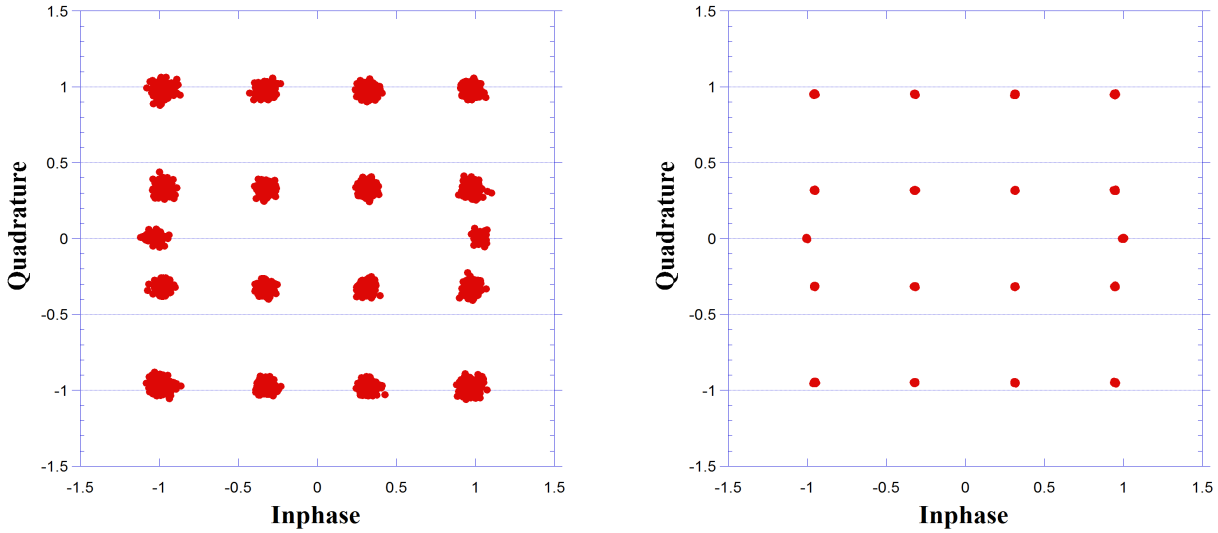

(a) (b)

Figure 3.8: Constellation of balanced modulator Case I (a) Output with No DPD (b) linearized output with proposed DPD.

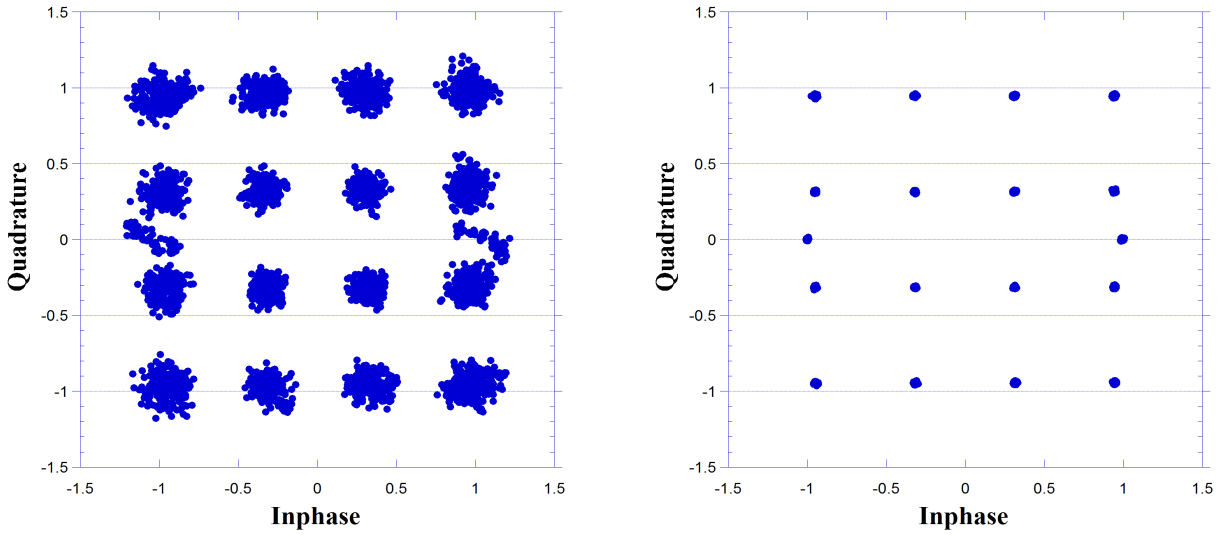

(a) (b)

Figure 3.9: Constellation of imbalanced modulator Case II (a) Output with No DPD (b) linearized output with proposed DPD.

impairments and was incapable of compensating the DC offset and make it even worse.

To evaluate the in-band performances, the error vector magnitude (EVM) was calculated and is shown in Table 3.1. As shown, the EVM was very high in the case of no compensation; and, it was equal to -23.12 dB and -18.47 dB for the balanced and gain/phase imbalanced modulators, respectively. The MP was able to compensate for the nonlinear distortion as their EVM reached -44.26 dB in the case of balanced modulator. However, for the imbalanced modulator, the MP DPD only achieved an EVM around -28.45 dB. While, the proposed model kept a good EVM of around -46 dB in the different studied cases. It can, therefore, be concluded that the performance of the proposed predistorter has a very good EVM in both cases as compared to the other models and with least complexity in terms of number of coefficients as shown in Table 3.2. This was also clear in the resulting constellation of the output signals as shown in Fig. 3.8 and Fig. 3.9 without linearization and with the proposed predistorter for the two modulator cases.

Model	Case I	Case II
No-DPD	-23.120	-18.47
MP DPD	-44.26	-28.45
PH DPD	-44.58	-43.357
Proposed DPD	-46.235	-45.934

Table 3.1: EVM values in (dB) for the Stated Models

Model	Model dimensions	Number of Coefficients
MP DPD	$(M, N) = (4, 8)$	$(M+1)\text{x}N = 40$
PH DPD	$(M, N_1, N_2) = (4, 8, 5)$	$(M+1)\text{x}(N_1+N_2)+1 = 66$
Proposed DPD	$(M, l_1, K) = (3, 2, 8)$	$2\text{x}((M+1)\text{x}(l_1+2))+K+1 = 41$

Table 3.2: Model dimensions and Number of Coefficients for the Stated Models

3.7.2 Scenario 2

The input signal used for validation in this case is a low-IF LTE signal of bandwidth 5 MHz used at intermediate frequency of 5 MHz. The sampling frequency is 92.16 MHz and the input waveform is 184,320 samples.

Due to the spectral content of the low-IF signals, an image signal will be generated at the output of the PA, that lie in the image band of the signal. In Case of the baseband signal, and due to its symmetry around the DC offset, the image signal will lie in the same band of the main signal, so the I/Q imperfections will appear as linear distortion in the signal constellation. Hence, the I/Q imbalance problem is less obvious. However, due to the MFI, the I/Q imbalance problem is more pronounced in the IF signals of scenario 2 than the baseband signals in scenario 1.

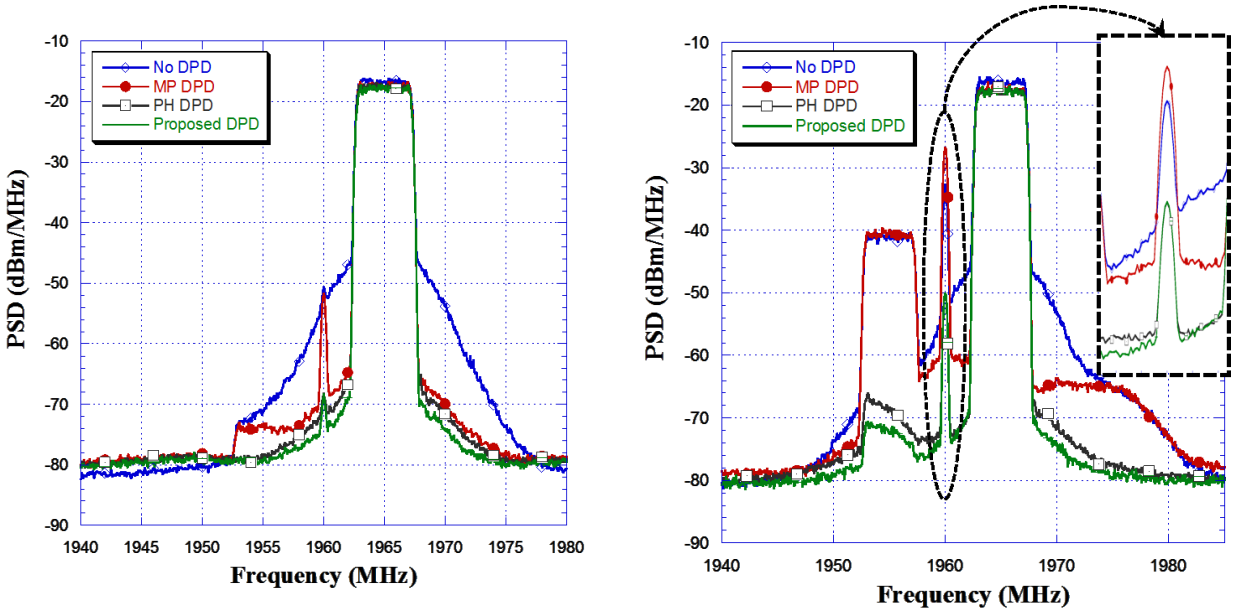

(a)

(b)

Figure 3.10: Measured PSDs with and without DPD for Scenario 2. (a) Case I. (b) Case II.

This is demonstrated in Figs. 3.10a and 3.10b, where the image signal is more obvious even in Case I with balanced modulators. In this case the MP DPD fell short of suppressing the image and the resultant DC offset even when there is no induced I/Q imbalance in Fig. 3.10a, but only the minor I/Q imperfections in the ESG are present. The proposed model for both cases can considerably push the MFI effect down and results in better linearity performance than the MP DPD and the PH DPD in both cases.

Table 3.3, shows the Image Rejection Ratio (IRR) in dBc for the three DPDs in case II for Scenario 2. The IRR is defined as the ratio of the IF signal level produced by the desired input frequency to that produced by the image frequency [14]. The results demonstrate that the effectiveness of the proposed DPD in further suppressing the image signal in the image band than the PH DPD. However, the MP DPD results in a very low IRR, due to its incapability of suppressing the image signal due to the MFI effects.

Model	IRR
MP DPD	25.1
PH DPD	51.1
Proposed DPD	54.8

Table 3.3: IRR in case II for Scenario 2

3.8 Conclusion

A Generalized Twin-Box model is proposed for the mutual compensation of the modulator imperfections and PA nonlinearities. The separate identification of the I/Q impairments and high static nonlinearities of the PA, significantly reduced the computational complexity of the model and offered more flexibility for the memory effects characterization. The proposed model was compared to the PH and the MP models, and showed improved performance in linearizing a class AB PA, than the state of the art DPDs for two different scenarios of zero-IF and low-IF transmitters.

Chapter 4

Linearization of a Concurrent Dual-Band Transmitter Exhibiting Nonlinear Distortion and Hardware Impairments

4.1 Introduction

With the fast development of wireless communication systems, there is an increasing demand of multi-band/multi-standard systems. In such systems, multi-band radio base stations allow the transmission of different wireless communication signals and support different standards concurrently.

However, when utilizing independent, conventional DPD techniques, such as Volterra DPD or MP DPD [37] for linearizing each band separately, do not provide satisfactory performance. Moreover, if these conventional DPDs are utilized to sample the multi-band signals as a wideband signal, tougher requirements for the bandwidth of the DACs and ADCs are forced. Therefore, using multi-band DPD cells, where the RF signals in each band are captured and digitized separately, alleviates such problems. Hence, the DPD cells will compensate for the distortion in each band separately, and incorporate the effects of the multi-input signals. Also, it is independent of the frequency separation between the bands, which will require lower sampling rates than those used by wideband DPDs.

linearization of multi-band transmitters has been recently explored in [51, 52, 97–101].

In [51], a frequency-selective linearization approach is proposed, where two independent DPD cells are used in order to alleviate the use of a wideband DPD model, and the nonlinear behavior of the PA is characterized using a large-signal network analyzer. In [52] and [97], a two-dimensional (2-D) memory polynomial (MP) DPD is applied to linearize a widely spaced dual-band PA transmitter. In [101], the analysis is extended to include the effects of third- and fifth-order inter-modulation products, which was previously analyzed in [102]. The effectiveness of adding the higher-order inter-modulation products on the DPD linearization is investigated in [101], for narrow-spaced input signals in dual-band and tri-band cases.

These different reported multi-band DPD cells use quadrature modulators to transfer the predistorted baseband signals to RF. However, they do not account for the imperfections of the I/Q modulators used in the feedback loop, which is used to estimate the nonlinear relation functions of the dual inputs and corresponding dual outputs. Therefore, their performance will be limited.

The effects of I/Q imbalance and the nonlinear dynamic distortion of the single-band PAs are discussed in the previous chapter. I/Q imperfections for concurrent multi-band transmitters are much greater than single-band transmitters, since the signal in each band is transmitted through a separate I/Q modulator channel, thus multiplying the problem. This was concluded in [103], where the authors deduced that multi-input multi-output (MIMO) systems are more vulnerable to RF impairments than SISO systems. However, PA distortion and other RF impairments were not investigated in [103]. In [104], the PA distortion as well as the modulator imperfections in a MIMO system are investigated by expanding the parallel Hammerstein single-band PA model in [95]. However in this case, the complexity of the model is very high as will be discussed later in this chapter. Also in [105], a real valued feedforward

neural network model is proposed for the joint predistortion of modulator imperfections and dual-band PA nonlinearity. The structure of the neural network model is extended in order to model the cross-modulation effects and modulator imperfections in the dual-band transmitter, which also results in an inherently complex model.

In this chapter, a technique for the joint mitigation of dual-band PA distortion and I/Q impairments in a complexity-reduced structure is proposed. A dual-input two-box structure was developed to accurately characterize and mitigate the in-band and cross-band distortion of the dual-band PA operating in concurrent mode and to compensate for the I/Q imperfections in the quadrature modulators of both bands [106].

The remainder of this chapter is organized as follows: Section 4.2 presents the modeling and characterization of the dual-band PA. Dual-band PA modeling and I/Q imbalance modeling are analyzed in Section 4.3. The motivation and the detailed description of the proposed model are given in Sections 4.4 and 4.5, respectively. Section 4.6 presents the measurement setup. The measurement and simulation results are presented in Section 4.7; and, the conclusion is presented in Section 4.8.

4.2 Dual-Band PA Modeling

The nonlinear behavior of a concurrent dual-band PA is more complex than that of a single-band PA, due to the cross-modulation products between the dual bands and the inter-modulation products of the PA nonlinear behavior [51]. Therefore, cross modulation and in-band inter-modulation both contribute to the nonlinearity of a concurrent dual-band PA [97,98]. This can be seen by exciting a dual-band PA with two inputs and capturing the

resultant distortion at the output of the PA.

Fig. 4.1 shows the power spectral densities (PSDs) at the output of a dual-band Doherty PA for concurrent and single modes of operation. The input signals for the upper and lower bands were two WCDMA signals. A WCDMA 111 signal was applied to the lower band (ω_1 = 880 MHz) with a PAPR of 10.6 dB. A WCDMA 101 signal was applied for the upper band (ω_2 = 1978 MHz) with a PAPR of 10.5 dB. Both signals have bandwidth of 15 MHz. The red curves in Fig. 4.1 (a and b) show the PA output at the lower and upper bands, when driven by the two WCDMA signals, concurrently. However, the blue curves show the PA output signals when the PA was driven in single-band mode, with one input signal. Fig. 4.1 compares the added in-band and out-of-band distortion at the output of the PA for the two bands in concurrent dual-band mode, with the single-band mode. This added distortion resulted from the cross-modulation and inter-modulation effects of the two input signals. Hence, using a conventional single input/single output DPD for the characterization of dual-band PAs is not appropriate, as it does not account for the cross-band effects.

Consequently, a dual-band model/DPD should be composed of two cells, one for each communication band. Each individual cell is fed with the dual inputs, such that the characterization of each band takes into account the in-band and cross-band effects of each band, as shown in Appendix A. This can be described by the general memoryless passband nonlinear transmitter model:

$$y(t) = \sum_{k=1}^{N} a_k x^k(t) \tag{4.1}$$

where N is the polynomial order, a_k is the set of bandpass model coefficients, $y(t)$ is the bandpass model output, and $x(t)$ is the bandpass input.

In case of multi-band transmitter, the bandpass model input can be represented as:

$$x(t) = \sum_{q} \mathrm{Re}[\tilde{x}_q(t) e^{j\omega_q t}] \tag{4.2}$$

where ω_q is the angular carrier frequency, $\tilde{x}_q(t)$ is the complex envelope of the bandpass signal $x_q(t)$, and $t = nT_\mathrm{s}$ where T_s is the sampling time intervals $T_\mathrm{s} = 1/f_\mathrm{s}$.

In this chapter, a dual-band transmitter is considered; therefore, the total input signal is $x(t) = x_1(t) + x_2(t)$. The general model for the dual-band transmitter output y is derived in the Appendix, (the notation (t) is removed for convenience) and given by:

$$\begin{aligned} y = \sum_{k=1}^{N} \sum_{r_1=0}^{k} \sum_{k_1=0}^{k-r_1} \sum_{k_2=0}^{r_1} \frac{1}{2^k} a_{kr_1} C_{r_1}^{k} C_{k_1}^{k-r_1} C_{k_2}^{r_1} \\ \times \Big[(\tilde{x}_1 |\tilde{x}_1|^{2k_1} |\tilde{x}_2|^{2k_2}) e^{j\omega_1 t} \\ + (\tilde{x}_2 |\tilde{x}_1|^{2k_1} |\tilde{x}_2|^{2k_2}) e^{j\omega_2 t} \\ + (\tilde{x}_1^* \tilde{x}_2^2 |\tilde{x}_1|^{2(k_1-1)} |\tilde{x}_2|^{2k_2}) e^{j(2\omega_2-\omega_1)t} \\ + (\tilde{x}_1^2 \tilde{x}_2^* |\tilde{x}_1|^{2k_1} |\tilde{x}_2|^{2(k_2-1)}) e^{j(2\omega_1-\omega_2)t} \\ + (\tilde{x}_1^3 \tilde{x}_2^{*2} |\tilde{x}_1|^{2k_1} |\tilde{x}_2|^{2(k_2-2)}) e^{j(3\omega_1-2\omega_2)t} + \cdots \Big] \end{aligned} \tag{4.3}$$

This general equation has components around two carrier frequencies (ω_1 and ω_2) and other higher-order inter-modulation (IMD) products.

If the frequency spacing between the two carrier frequencies is large enough, the inter-band third-order inter-modulation products around $(2\omega_2 - \omega_1)$ and $(2\omega_1 - \omega_2)$ and further higher order inter-modulation products can be filtered out. The model can then consider the terms around the two center frequencies, which include the in-band inter-modulation and cross-band inter-modulation products, as derived in Appendix A ((A.10) and (A.11)).

The general model can be further enhanced to include the memory effects exhibited by a

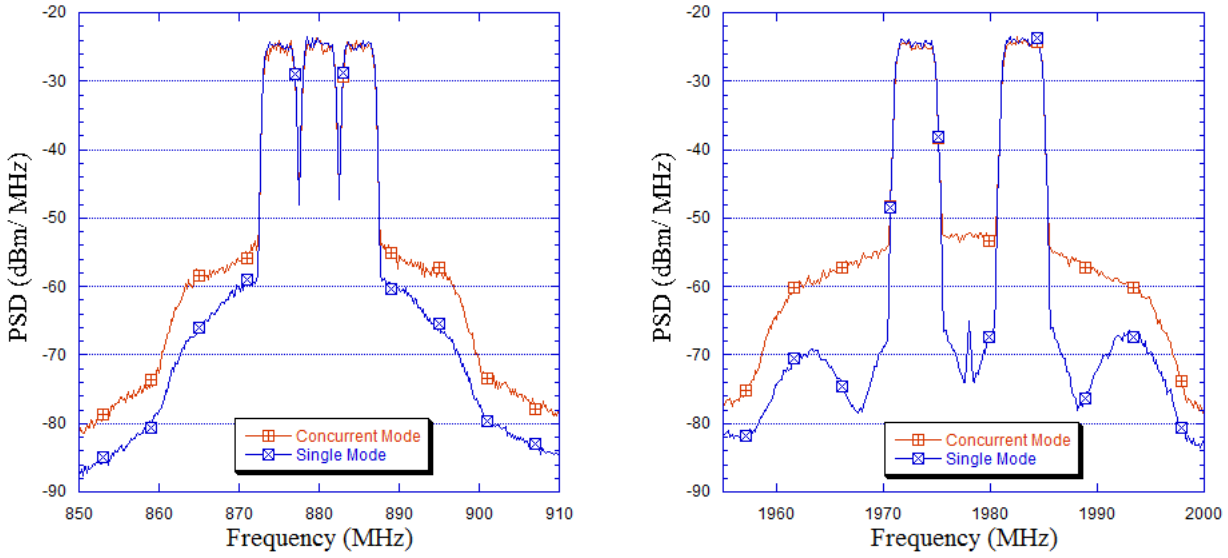

Figure 4.1: PSDs at the output of a dual-band Doherty PA for concurrent and single modes of operation. (a) Lower band at 880 MHz. (b) Upper band at 1978 MHz.

dual-band PA, for better characterization of the static and dynamic nonlinearities exhibited by the PA.

A 2-D MP model has been developed for the modeling of the dual-band transmitter [52]. This model is composed of two cells, one for each band. The model estimated outputs are given by the following equations:

$$\tilde{y}_1(n) = \sum_{k=0}^{N} \sum_{j=0}^{k} \sum_{m=0}^{M} h_{k,j,m}^{(1)} \tilde{x}_1(n-m) \times |\tilde{x}_1(n-m)|^{k-j} |\tilde{x}_2(n-m)|^{j} \tag{4.4}$$

$$\tilde{y}_2(n) = \sum_{k=0}^{N} \sum_{j=0}^{k} \sum_{m=0}^{M} h_{k,j,m}^{(2)} \tilde{x}_2(n-m) \times |\tilde{x}_1(n-m)|^{k-j} |\tilde{x}_2(n-m)|^{j} \tag{4.5}$$

where $\tilde{y}_1(n)$ and $\tilde{y}_2(n)$ are the complex envelopes of the estimated baseband model outputs of the two bands centered around the two fundamental frequencies ω_1 and ω_2, respectively; $\tilde{x}_1(n)$ and $\tilde{x}_2(n)$ are baseband input signals at the lower and upper bands, respectively; $h_{k,j,m}^{(1)}$ and $h_{k,j,m}^{(2)}$ are the model coefficients for the two bands.

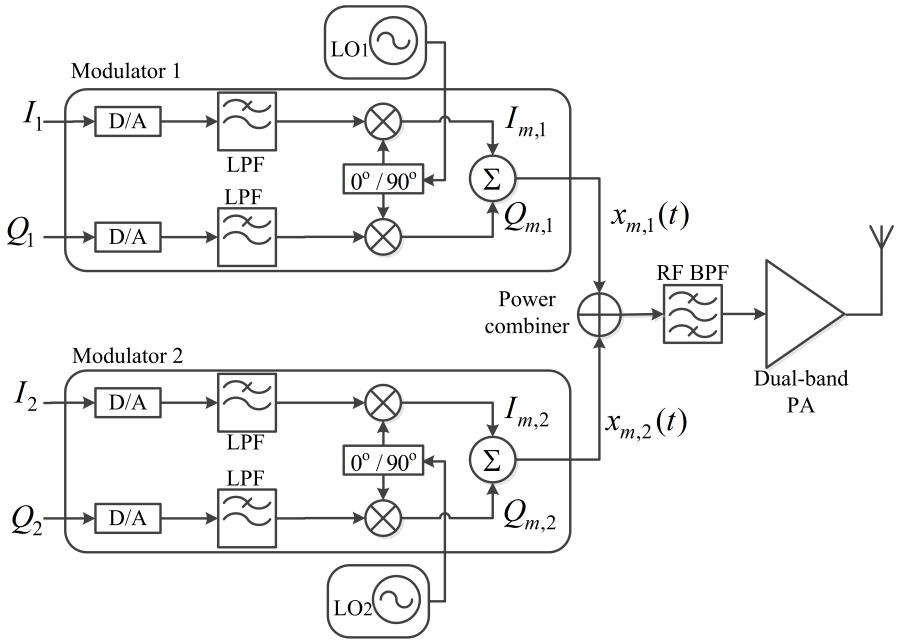

Figure 4.2: Concurrent Dual-band transmitter.

However, this model, which is referred to as the 2-D MP model throughout the rest of the paper, does not consider the I/Q impairments and DC offsets of the quadrature modulators in a multi-band transmitter. Therefore, the performance of this 2-D MP DPD suffers a noticeable degradation, as will be demonstrated in the following sections.

4.3 Joint compensation of Dual-Band PA and I/Q Imbalance

A first approach to develop a compound single structure for the modeling and compensation of dual-band transmitter distortions (inter-modulation and cross-modulation) and the I/Q imperfections in the two quadrature modulators in a dual-band transmitter chain is presented in this section.

This section provides the analytical formulation and modeling approach of a dual-band nonlinear system consisting of two quadrature modulators and a dual-band PA as shown in Fig. 4.2. It is assumed that each quadrature modulator has independent I/Q imbalance

effects and the dual-band PA has nonlinear behavior as described in Section 4.2.

Considering the first quadrature modulator required to up-convert the lower band to ω_1 with G_1 gain imbalance in dB, and ϕ_1 phase imbalance in degrees. The second quadrature modulator, required to up-convert the upper band to ω_2, has G_2 gain imbalance in dB, and ϕ_2 phase imbalance in degrees. The RF signals at the output of the two modulators, $x_{m,1}(t)$ and $x_{m,2}(t)$, are given as:

$$\begin{aligned} x_{\mathrm{m},1}(t) &= \alpha_1 I_1(t)\cos(\omega_1 t + \theta_1) - \alpha_2 Q_1(t)\sin(\omega_1 t + \theta_2) \\ x_{\mathrm{m},2}(t) &= \alpha_3 I_2(t)\cos(\omega_2 t + \theta_3) - \alpha_4 Q_2(t)\sin(\omega_2 t + \theta_4) \end{aligned} \tag{4.6}$$

where $\frac{\alpha_2}{\alpha_1} = 10^{\left(\frac{G_1}{20}\right)}$, $\frac{\alpha_4}{\alpha_3} = 10^{\left(\frac{G_2}{20}\right)}$, $\phi_1 = \theta_2 - \theta_1$, and $\phi_2 = \theta_4 - \theta_3$. $I_1(t)$ and $Q_1(t)$ are the in-phase and quadrature components of the baseband signal $x_1(t)$, respectively. While, $I_2(t)$ and $Q_2(t)$ are the in-phase and quadrature components of the complex envelope of the baseband signal $x_2(t)$, respectively.

The discrete time samples of the complex envelope of the RF signal, $x_{\mathrm{m},1}(t)$, at the output of the first quadrature modulator, are given by:

$$\begin{aligned} I_{\mathrm{m},1}(n) &= \alpha_1\cos(\theta_1) I_1(n) - \alpha_2\sin(\theta_2) Q_1(n) \\ Q_{\mathrm{m},1}(t) &= \alpha_1\sin(\theta_1) I_1(n) + \alpha_2\cos(\theta_2) Q_1(n) \end{aligned} \tag{4.7}$$

The discrete time samples of the complex envelope of the RF signal, $x_{\mathrm{m},2}(t)$, at the output of the second quadrature modulator, are given by:

$$\begin{aligned} I_{\mathrm{m},2}(n) &= \alpha_3\cos(\theta_3) I_2(n) - \alpha_4\sin(\theta_4) Q_2(n) \\ Q_{\mathrm{m},2}(t) &= \alpha_3\sin(\theta_3) I_2(n) + \alpha_4\cos(\theta_4) Q_2(n) \end{aligned} \tag{4.8}$$

Therefore, the complex envelope signals of the RF signals considering the effects of the

quadrature modulators imperfections are given as:

$$\tilde{x}_{\mathrm{m},1}(n) = [\alpha_1 \cos(\theta_1) + \alpha_2 \cos(\theta_2)]\, \tilde{x}_1(n) + [\alpha_1 \cos(\theta_1) - \alpha_2 \cos(\theta_2)]\, \tilde{x}_1^*(n)$$
$$+ j\, \{[\alpha_1 \sin(\theta_1) + \alpha_2 \sin(\theta_2)]\, \tilde{x}_1(n) + [\alpha_1 \sin(\theta_1) - \alpha_2 \sin(\theta_2)]\, \tilde{x}_1^*(n)\} \tag{4.9}$$

$$\tilde{x}_{\mathrm{m},2}(n) = [\alpha_3 \cos(\theta_3) + \alpha_4 \cos(\theta_4)]\, \tilde{x}_2(n) + [\alpha_3 \cos(\theta_3) - \alpha_4 \cos(\theta_4)]\, \tilde{x}_2^*(n)$$
$$+ j\, \{[\alpha_3 \sin(\theta_3) + \alpha_4 \sin(\theta_4)]\, \tilde{x}_2(n) + [\alpha_3 \sin(\theta_3) - \alpha_4 \sin(\theta_4)]\, \tilde{x}_2^*(n)\} \tag{4.10}$$

Using the 2-D MP model in (4.4) and (4.5), the complex envelope of the signals at the output of the dual-band PA at the center frequencies ω_1 and ω_2, accounting for the imperfections of the quadrature modulators, can be expressed as follows for a memoryless case:

$$\tilde{y}_1(n) = \sum_{k=0}^{N} \sum_{j=0}^{k} h_{k,j}^{(1)} \tilde{x}_{\mathrm{m},1}(n) |\tilde{x}_{\mathrm{m},1}(n)|^{k-j} |\tilde{x}_{\mathrm{m},2}(n)|^j \tag{4.11}$$

Then, by using (4.9) and (4.10), the relation between the complex envelope of the dual-band PA output and the input signals to the modulators will be given as follows:

$$\begin{aligned}
&\tilde{y}_1(n) = \\
&\left(h_{0,0}^{(1)} \alpha_1 \cos(\theta_1) + h_{0,0}^{(1)} \alpha_2 \cos(\theta_2) + j h_{0,0}^{(1)} \alpha_1 \sin(\theta_1) + j h_{0,0}^{(1)} \alpha_2 \sin(\theta_2) \right) \tilde{x}_1(n) + \\
&\left(h_{0,0}^{(1)} \alpha_1 \cos(\theta_1) - h_{0,0}^{(1)} \alpha_2 \cos(\theta_2) + j h_{0,0}^{(1)} \alpha_1 \sin(\theta_1) - j h_{0,0}^{(1)} \alpha_2 \sin(\theta_2) \right) \tilde{x}_1^*(n) + \\
&\left(\begin{array}{l} 4 h_{1,0}^{(1)} \alpha_1^2 \alpha_2 \cos^2(\theta_1) \cos(\theta_2) + 4 h_{1,0}^{(1)} \alpha_1 \alpha_2^2 \cos(\theta_1) \cos^2(\theta_2) + \\ j 4 h_{1,0}^{(1)} \alpha_1^2 \alpha_2 \sin(\theta_1) \cos(\theta_1) \cos(\theta_2) + j 4 h_{1,0}^{(1)} \alpha_1 \alpha_2^2 \sin(\theta_2) \cos(\theta_1) \cos(\theta_2) \end{array} \right) \tilde{x}_1^3(n) + \\
&\left(\begin{array}{l} 4 h_{1,0}^{(1)} \alpha_1^2 \alpha_2 \cos(\theta_1) \sin(\theta_1) \sin(\theta_2) - 4 h_{1,0}^{(1)} \alpha_1 \alpha_2^2 \cos(\theta_1) \sin(\theta_1) \sin(\theta_2) + \\ j 4 h_{1,0}^{(1)} \alpha_1^2 \alpha_2 \sin^2(\theta_1) \sin(\theta_2) - j 4 h_{1,0}^{(1)} \alpha_1 \alpha_2^2 \sin(\theta_1) \sin^2(\theta_2) \end{array} \right) \tilde{x}_1^{*3}(n) +
\end{aligned}$$

$$
\left(\begin{array}{l}
2h_{1,0}^{(1)}\alpha_1\cos(\theta_1)(\alpha_1^2-\alpha_2^2)+2h_{1,0}^{(1)}\alpha_2\cos(\theta_2)(\alpha_1^2-\alpha_2^2)+\\
j2h_{1,0}^{(1)}\alpha_1\sin(\theta_1)(\alpha_1^2-\alpha_2^2)+j2h_{1,0}^{(1)}\alpha_2\sin(\theta_2)(\alpha_1^2-\alpha_2^2)+\\
4h_{1,0}^{(1)}\alpha_1^2\alpha_2\cos^2(\theta_1)\cos(\theta_2)-4h_{1,0}^{(1)}\alpha_1\alpha_2^2\cos(\theta_1)\cos^2(\theta_2)+\\
j4h_{1,0}^{(1)}\alpha_1^2\alpha_2\sin(\theta_1)\cos(\theta_1)\cos(\theta_2)-j4h_{1,0}^{(1)}\alpha_1\alpha_2^2\sin(\theta_2)\cos(\theta_1)\cos(\theta_2)
\end{array}\right)\tilde{x}_1(n)|\tilde{x}_1(n)|^2+
$$

$$
\left(\begin{array}{l}
2h_{1,0}^{(1)}\alpha_1\cos(\theta_1)(\alpha_1^2-\alpha_2^2)-2h_{1,0}^{(1)}\alpha_2\cos(\theta_2)(\alpha_1^2-\alpha_2^2)+\\
j2h_{1,0}^{(1)}\alpha_1\sin(\theta_1)(\alpha_1^2-\alpha_2^2)-j2h_{1,0}^{(1)}\alpha_2\sin(\theta_2)(\alpha_1^2-\alpha_2^2)+\\
j4h_{1,0}^{(1)}\alpha_1^2\alpha_2\sin^2(\theta_1)\sin(\theta_2)+j4h_{1,0}^{(1)}\alpha_1\alpha_2^2\sin(\theta_1)\sin^2(\theta_2)+\\
4h_{1,0}^{(1)}\alpha_1^2\alpha_2\cos(\theta_1)\sin(\theta_1)\sin(\theta_2)+4h_{1,0}^{(1)}\alpha_1\alpha_2^2\cos(\theta_1)\sin(\theta_1)\sin(\theta_2)
\end{array}\right)\tilde{x}_1^*(n)|\tilde{x}_1(n)|^2+
$$

$$
\left(\begin{array}{l}
2h_{0,1}^{(1)}\alpha_1\cos(\theta_1)(\alpha_3^2-\alpha_4^2)+2h_{0,1}^{(1)}\alpha_2\cos(\theta_2)(\alpha_3^2-\alpha_4^2)+\\
j2h_{0,1}^{(1)}\alpha_1\sin(\theta_1)(\alpha_3^2-\alpha_4^2)+j2h_{0,1}^{(1)}\alpha_2\sin(\theta_2)(\alpha_3^2-\alpha_4^2)
\end{array}\right)\tilde{x}_1(n)|\tilde{x}_2(n)|^2+
$$

$$
\left(\begin{array}{l}
2h_{0,1}^{(1)}\alpha_1\cos(\theta_1)(\alpha_3^2-\alpha_4^2)-2h_{0,1}^{(1)}\alpha_2\cos(\theta_2)(\alpha_3^2-\alpha_4^2)+\\
j2h_{0,1}^{(1)}\alpha_1\sin(\theta_1)(\alpha_3^2-\alpha_4^2)-j2h_{0,1}^{(1)}\alpha_2\sin(\theta_2)(\alpha_3^2-\alpha_4^2)
\end{array}\right)\tilde{x}_1^*(n)|\tilde{x}_2(n)|^2+
$$

$$
\left(\begin{array}{l}
4h_{1,1}^{(1)}\alpha_1(\alpha_1^2-\alpha_2^2)(\alpha_3^2-\alpha_4^2)\cos(\theta_1)+\\
4h_{1,1}^{(1)}\alpha_2(\alpha_1^2-\alpha_2^2)(\alpha_3^2-\alpha_4^2)\cos(\theta_2+\\
j4h_{1,1}^{(1)}\alpha_1(\alpha_1^2-\alpha_2^2)(\alpha_3^2-\alpha_4^2)\sin(\theta_1)+\\
j4h_{1,1}^{(1)}\alpha_2(\alpha_1^2-\alpha_2^2)(\alpha_3^2-\alpha_4^2)\sin(\theta_2)+\\
8h_{1,1}^{(1)}\alpha_1^2\alpha_2(\alpha_3^2-\alpha_4^2)\cos^2(\theta_1)\cos(\theta_2)-\\
8h_{1,1}^{(1)}\alpha_1\alpha_2^2(\alpha_3^2-\alpha_4^2)\cos(\theta_1)\cos^2(\theta_2)+\\
j8h_{1,1}^{(1)}\alpha_1^2\alpha_2(\alpha_3^2-\alpha_4^2)\sin(\theta_1)\cos(\theta_1)\cos(\theta_2)-\\
j8h_{1,1}^{(1)}\alpha_1\alpha_2^2(\alpha_3^2-\alpha_4^2)\sin(\theta_2)\cos(\theta_1)\cos(\theta_2)
\end{array}\right)\tilde{x}_1(n)|\tilde{x}_1(n)|^2|\tilde{x}_2(n)|^2+
$$

$$\left(\begin{array}{l} 4h_{1,1}^{(1)}\alpha_1(\alpha_1^2-\alpha_2^2)(\alpha_3^2-\alpha_4^2)\cos(\theta_1)- \\ 4h_{1,1}^{(1)}\alpha_2(\alpha_1^2-\alpha_2^2)(\alpha_3^2-\alpha_4^2)\cos(\theta_2)+ \\ j4h_{1,1}^{(1)}\alpha_1(\alpha_1^2-\alpha_2^2)(\alpha_3^2-\alpha_4^2)\sin(\theta_1)- \\ j4h_{1,1}^{(1)}\alpha_2(\alpha_1^2-\alpha_2^2)(\alpha_3^2-\alpha_4^2)\sin(\theta_2)+ \\ j8h_{1,1}^{(1)}\alpha_1^2\alpha_2(\alpha_3^2-\alpha_4^2)\sin^2(\theta_1)\sin(\theta_2)+ \\ j8h_{1,1}^{(1)}\alpha_1\alpha_2^2(\alpha_3^2-\alpha_4^2)\sin(\theta_1)\sin^2(\theta_2)+ \\ 8h_{1,1}^{(1)}\alpha_1^2\alpha_2(\alpha_3^2-\alpha_4^2)\cos(\theta_1)\sin(\theta_1)\sin(\theta_2)+ \\ 8h_{1,1}^{(1)}\alpha_1\alpha_2^2(\alpha_3^2-\alpha_4^2)\cos(\theta_1)\sin(\theta_1)\sin(\theta_2) \end{array}\right) \tilde{x}_1^*(n)|\tilde{x}_1(n)|^2|\tilde{x}_2(n)|^2+\cdots \tag{4.12}$$

Similarly, the output $\tilde{y}_2(n)$ around ω_2 can be formulated in a similar manner to (4.12). The general equation (4.12) has terms located away from the band of interest, so they can be ignored herein.

Therefore, in order to compensate for the modulator imperfections and dual-band PA dynamic distortion, a joint dual-band model can be formulated as follows:

$$\begin{aligned}\tilde{y}_1(n) = \sum_{m=0}^{M}\Bigg[&\sum_{k=0}^{N_1}\sum_{j=0}^{k} a_{k,j,m}^{(1)}\psi_{mkj}^{(1)}(\tilde{x}_1(n),\tilde{x}_2(n))+ \\ &\sum_{k=0}^{N_1}\sum_{j=0}^{k} b_{k,j,m}^{(1)}\bar{\psi}_{mkj}^{(1)}(\tilde{x}_1^*(n),\tilde{x}_2(n))\Bigg]+d_1\end{aligned} \tag{4.13}$$

$$\begin{aligned}\tilde{y}_2(n) = \sum_{m=0}^{M}\Bigg[&\sum_{k=0}^{N_1}\sum_{j=0}^{k} a_{k,j,m}^{(2)}\psi_{mkj}^{(2)}(\tilde{x}_2(n),\tilde{x}_1(n))+ \\ &\sum_{k=0}^{N_1}\sum_{j=0}^{k} b_{k,j,m}^{(2)}\bar{\psi}_{mkj}^{(2)}(\tilde{x}_2^*(n),\tilde{x}_1(n))\Bigg]+d_2\end{aligned} \tag{4.14}$$

where d_1 and d_2 are the DC offsets in the lower and upper bands, respectively; with a memory depth of M; N_1 and N_2 are the nonlinearity orders for the direct and image branches. $\psi_{mkj}^{(1)}$

are $\bar{\psi}^{(1)}_{mkj}$ the nonlinear basis function series of the dual-input signals of inputs ($x_1(n)$ and $x_2(n)$) and ($x_1^*(n)$ and $x_2(n)$), respectively, as follows:

$$\begin{aligned}\psi^{(1)}_{mkj}(\tilde{x}_1(n),\tilde{x}_2(n)) &= \tilde{x}_1(n-m)|\tilde{x}_1(n-m)|^{k-j}|\tilde{x}_2(n-m)|^j \\ \bar{\psi}^{(1)}_{mkj}(\tilde{x}_1^*(n),\tilde{x}_2(n)) &= \tilde{x}_1^*(n-m)|\tilde{x}_1(n-m)|^{k-j}|\tilde{x}_2(n-m)|^j\end{aligned} \tag{4.15}$$

$\psi^{(2)}_{mkj}$ are $\bar{\psi}^{(2)}_{mkj}$ the nonlinear basis function series of the dual-input signals of inputs ($x_2(n)$ and $x_1(n)$) and ($x_2^*(n)$ and $x_1(n)$), respectively, and are computed in a similar manner to (4.15). This compound structure model is referred to as the parallel-MP model throughout the rest of the paper.

A schematic of the model is shown in Fig. 4.3. As deduced, this compound parallel-MP model could characterize and compensate for the dual-band transmitter RF impairments, which include the inter-modulation products of the PA, the cross-modulation products due to the dual inputs, and the I/Q modulators imperfections.

The dimensionality of the 2-D MP model in [52] (given by (4.4) and (4.5)) is, however, greater than that of the single-band MP model [36]. This increase is unavoidable, due to the addition of the cross effects of both inputs at the output of each band, which significantly increases the number of coefficients. Furthermore, the compound parallel-MP model (4.13) and (4.14), which compensates for the I/Q imperfections as well as the dual-band PA nonlinearity, further multiplies the dimensionality of the model, by adding a parallel-MP structure and applying the signals' conjugate images as input to this parallel structure.

It can be deduced that the number of complex coefficients (P) for each band, given by the 2-D MP model [52], can be computed as follows:

$$P = \sum_{i=1}^{N+1}(i) \times (M+1) \tag{4.16}$$

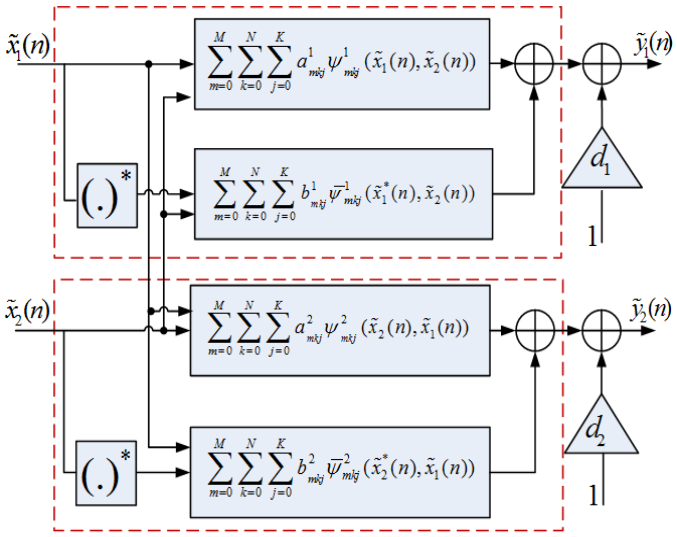

Figure 4.3: Schematic of the joint predistorter of PA nonlinearity and I/Q impairments for a dual-band PA.

For example, if the memory depth M is 4 and the nonlinearity order N is 5, the total number of coefficients P for each band is equal to 105. For the compound parallel-MP model with I/Q compensations, given by (4.13) and (4.14), the total number of coefficients is equal to $(2P+1)$ for each band (for $N_1 = N_2$). For the numerical example of $M = 4$ and $N_1 = N_1 = 5$, the total number of coefficients is equal to 212 for each band.

This significant increase in the number of coefficients increases the computational load and the numerical stability of the model during the identification step and affects the performance of the model. One approach to reducing the complexity of this model is the selection of a lower nonlinearity order for the complex branch rather than the nonlinearity order of the direct signal branch (i.e., $N_1 > N_2$). In this way, the total number of coefficients is reduced. However, the overall complexity is still considered high.

4.4 Motivation of the Proposed Model

In order to alleviate the drawback of the previously reported parallel-MP compound structure and to further enhance the performance of the model, a complexity-reduced model is presented in this chapter. The model is based on a dual-input truncated Volterra structure that is proposed for the modeling and compensation of the dual-band distortion and the I/Q modulator impairments. The proposed model is also composed of two cells, one for each communication band. Each cell is composed of two parallel branches of a dual-input truncated Volterra filter, which includes second-order cross terms followed by a 2-D LUT, as shown in Fig. 4.4.

The dual-input truncated Volterra filters in the two branches are used for the modeling of the mildly nonlinear dynamic effects of the PA as well as for I/Q impairment modeling and compensation. The 2-D LUT in each cell of each band is used for the modeling of the high static nonlinearities of the dual-band PA, which includes the inter-modulation and cross-modulation distortion effects of the two bands. The major advantage of this proposed model compared to the parallel-MP model given by (4.13) and (4.14) is the identification of the mild dynamic nonlinearities and the I/Q imbalances in one step through the dual-input Volterra filters, offering more flexibility in modeling the memory effects of the dual-band PA.

The high static nonlinearities are also characterized through a 2-D LUT. However, the nonlinearity orders are different for the static nonlinear LUT box and the dynamic nonlinear Volterra filter, which reduces the complexity of the model. On the other hand, the parallel-MP model has a fixed nonlinear order for all the branches, which results in an oversized model.

A truncated Volterra filter is used as the first block instead of a linear-time-invariant (LTI) filter, since an LTI filter does not take into account the nonlinear memory effects [68] and the cross terms of the interaction between the previous samples. Therefore, in order to model the nonlinear memory effects and to further improve the model capabilities, a dual-input truncated Volterra filter is used. The extracted transfer functions of the dynamic memory effect model show a weak nonlinear behavior. Thus, a truncated Volterra filter is sufficient to represent this weak nonlinearity. Moreover, the inclusion of the cross terms in this model results in a more accurate characterization of the dual-band PA.

A full nonlinear Volterra model is not applied to the signal and its conjugate image in a similar manner to the parallel-MP model, since this considerably increases the computational complexity of the model. This will affect the stability of the model, while calculating the pseudo-inverse matrix for model identification. It was found that passing the dual-band signals and their conjugate images to the truncated Volterra filters can jointly compensate for mild dynamic nonlinearities and I/Q imperfections. The separate characterization of the highly static nonlinearities of the dual-band PA through a 2-D LUT reduces the computational complexities of the model, thus enhancing its performance.

4.5 Proposed dual-input truncated Volterra model

4.5.1 Proposed Model Configuration

A single-input truncated Volterra model [77], where only the second-order cross-terms are considered, i.e., the products of the signal and the delayed envelope at a different time delay,

and with an arbitrary polynomial order, is given by:

$$y(n) = \sum_{i=0}^{M_1} h_i u(n-i) + \sum_{i=0}^{M_1}\sum_{j=0}^{M_2}\sum_{k=1}^{K} h_{ijk} u(n-i)|u(n-j)|^k \tag{4.17}$$

where, $u(n)$ and $y(n)$ are the input and estimated output of the model, respectively. M_1 and M_2 are the finite memory length of both the input signal and its delayed envelope, respectively; K is the truncated nonlinearity order of the Volterra model; and, $h_{(.)}$ designates the model coefficients.

The proposed model configuration can be described as follows: The truncated Volterra models given by (4.17) are extended to include the effects of both input signals on the output in each band and applied in two parallel branches for the signal and its conjugate image. The modified dual-input truncated Volterra function is then given by:

$$\begin{aligned} u_1(n) = &\sum_{m_1=0}^{M_1} x_1(n-m_1) \times \left[\sum_{m_2=0}^{M_2}\sum_{k=0}^{N} a^{(1)}_{m_1m_2}(k)|x_1(n-m_1)|^k + \sum_{m_2=0}^{M_2} b^{(1)}_{m_1m_2}|x_2(n-m_2)|\right] + \\ &\sum_{m_1=0}^{M_1} x_1^*(n-m_1) \times \left[\sum_{m_2=0}^{M_2}\sum_{k=0}^{N} \bar{a}^{(1)}_{m_1m_2}(k)|x_1(n-m_1)|^k + \sum_{m_2=0}^{M_2} \bar{b}^{(1)}_{m_1m_2}|x_2(n-m_2)|\right] + d_1 \end{aligned} \tag{4.18}$$

$$\begin{aligned} u_2(n) = &\sum_{m_1=0}^{M_1} x_2(n-m_1) \times \left[\sum_{m_2=0}^{M_2}\sum_{k=0}^{N} a^{(2)}_{m_1m_2}(k)|x_2(n-m_1)|^k + \sum_{m_2=0}^{M_2} b^{(2)}_{m_1m_2}|x_1(n-m_2)|\right] + \\ &\sum_{m_1=0}^{M_1} x_2^*(n-m_1) \times \left[\sum_{m_2=0}^{M_2}\sum_{k=0}^{N} \bar{a}^{(2)}_{m_1m_2}(k)|x_2(n-m_1)|^k + \sum_{m_2=0}^{M_2} \bar{b}^{(2)}_{m_1m_2}|x_1(n-m_2)|\right] + d_2 \end{aligned} \tag{4.19}$$

where $x_1(n)$ and $x_2(n)$ are the input signals in the lower and upper bands, respectively; $u_1(n)$ and $u_2(n)$ are the Volterra filters output signals of the lower and upper bands. M_1 and M_2 are the finite memory depths of the input signal and the envelope signal, respectively; $(a^{(1)}_{m_1m_2}, b^{(1)}_{m_1m_2})$ and $(\bar{a}^{(1)}_{m_1m_2}, \bar{b}^{(1)}_{m_1m_2})$ are the model coefficients for the lower-band signal and

its conjugate image; $(a^{(2)}_{m_1m_2}, b^{(2)}_{m_1m_2})$ and $(\bar{a}^{(2)}_{m_1m_2}, \bar{b}^{(2)}_{m_1m_2})$ are the model coefficients for the upper-band signal and its conjugate image; and, d_1 and d_2 are the DC offsets in the lower and upper bands, respectively.

The second block of the proposed model is a 2-D LUT for the characterization of the higher order static nonlinearities and the cross-modulation effects of both inputs. The output of the 2-D LUT, which is a function of the outputs of the first blocks, is given by:

$$\begin{aligned} y_1(n) &= G_1\left(|u_1(n)|.|u_2(n)|\right) \times u_1(n) \\ y_2(n) &= G_2\left(|u_1(n)|.|u_2(n)|\right) \times u_2(n) \end{aligned} \tag{4.20}$$

where $y_1(n)$ and $y_2(n)$ are the estimated model outputs for the lower and upper bands, respectively; G_1 and G_2 are the memoryless complex gain functions of the 2-D LUTs of the lower and upper bands, respectively, which are functions of the input signals complex envelopes, and are given by:

$$\begin{aligned} G_1\left(|u_1(n)|.|u_2(n)|\right) &= \sum_{i=0}^{K-1} \sum_{j=0}^{K-i-1} s^{(1)}_{i,j} |u_1(n)|^i |u_2(n)|^j \\ G_2\left(|u_1(n)|.|u_2(n)|\right) &= \sum_{i=0}^{K-1} \sum_{j=0}^{K-i-1} s^{(2)}_{i,j} |u_1(n)|^i |u_2(n)|^j \end{aligned} \tag{4.21}$$

The LUT functions are identified using polynomial fitting, where the coefficients $s^{(1)}_{i,j}$ and $s^{(2)}_{i,j}$ are extracted using least squares. Fig. 4.5 shows a schematic of the 2-D LUT of the lower band.

4.5.2 Model Identification

The identification procedure of the mildly nonlinear dynamic function implemented using the Volterra filters is done using least squares algorithm. Both filters of the main and conjugate branches are identified simultaneously as follows:

$$\mathbf{u_i} = \Psi_{(i)} \mathbf{A}^{(i)} \tag{4.22}$$

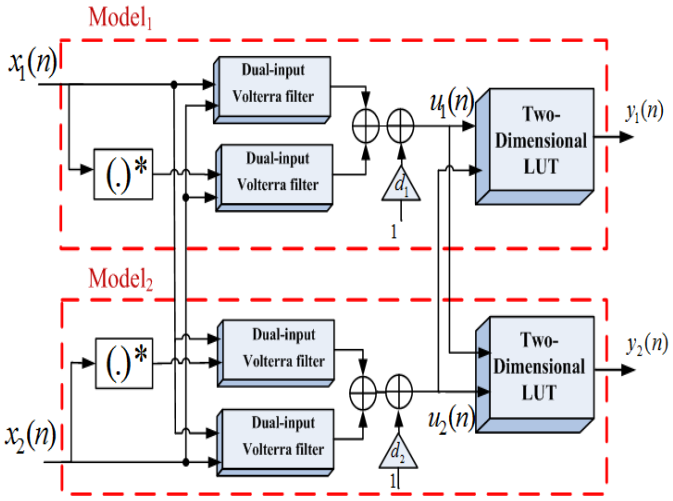

Figure 4.4: Schematic of the dual-input proposed model for the joint predistortion of PA nonlinearity and I/Q impairments for a dual-band PA.

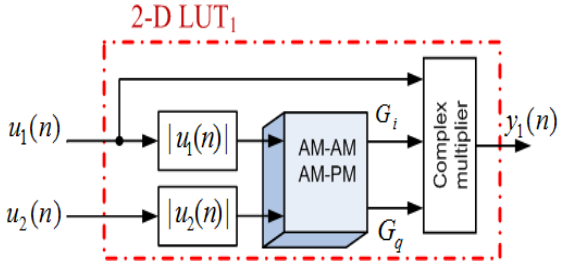

Figure 4.5: Schematic of the static nonlinear 2-D LUT_1.

where $\mathbf{u_i}$ is the estimated output vector of the two dynamic nonlinear Volterra filters, $\Psi_{(i)}$ is the matrix constructed using the basis functions of these two polynomial boxes and their input signals, and $\mathbf{A}^{(i)}$ is the vector containing the polynomial boxes coefficients. We define the vectors as follows:

$$\mathbf{u_i} = [\tilde{u}_i(1), \tilde{u}_i(2), \cdots, \tilde{u}_i(L)]^T$$

$$\mathbf{A}^{(i)} = \left[a_{00}^{(i)}(0), \cdots, a_{M_1M_2}^{(i)}(N), b_{00}^{(i)}, \cdots, b_{M_1M_2}^{(i)}, \bar{a}_{00}^{(i)}(0), \cdots, \bar{a}_{M_1M_2}^{(i)}(N), \bar{b}_{00}^{(i)}, \cdots, \bar{b}_{M_1M_2}^{(i)}, d_i\right]$$

where L is the length of the input samples training sequence used for identification, $i = 1$ for the lower band and $i = 2$ for the upper band.

The matrix $\Psi_{(i)}$ can be analyzed into sub-matrices as follows:

$$\Psi_{(i)} = \left[\Psi_{i,j}\ \bar{\Psi}_{i,j}\ \mathbf{1}\right] \tag{4.23}$$

where, $\Psi_{i,j}$ and $\bar{\Psi}_{i,j}$ are sub-matrices formed by the input signal and its conjugate image, respectively. The vector $\mathbf{1} = [1, 1, 1, \cdots, 1]^T$. The sub-matrix $\bar{\Psi}_{i,j}$ is the conjugate matrix of $\Psi_{i,j}$ as follows:

$\Psi_{i,j} =$

$$\begin{bmatrix} x_i(n) & \cdots & x_i(n-M_1)|x_j(n-M_1)|^N & \cdots & x_i(n-M_1)|x_j(n-M_2)| \\ x_i(n+1) & \cdots & x_i(n+1-M_1)|x_j(n+1-M_1)|^N & \cdots & x_i(n+1-M_1)|x_j(n+1-M_2)| \\ \vdots & & \vdots & \ddots & \vdots \\ x_i(n+L) & \cdots & x_i(n+L-M_1)|x_j(n+L-M_1)|^N & \cdots & x_i(n+L-M_1)|x_j(n+L-M_2)| \end{bmatrix}$$

and $\bar{\Psi}_{i,j} =$

$$\begin{bmatrix} x_i^*(n) & \cdots & x_i^*(n-M_1)|x_j(n-M_1)|^N & \cdots & x_i^*(n-M_1)|x_j(n-M_2)| \\ x_i^*(n+1) & \cdots & x_i^*(n+1-M_1)|x_i(n+1-M_1)|^N & \cdots & x_i^*(n+1-M_1)|x_j(n+1-M_2)| \\ \vdots & & \vdots & \ddots & \vdots \\ x_i^*(n+L) & \cdots & x_i^*(n+L-M_1)|x_i(n+L-M_1)|^N & \cdots & x_i^*(n+L-M_1)|x_j(n+L-M_2)| \end{bmatrix}$$

where the notation $(i, j) = (1, 2)$ for lower band and $(i, j) = (2, 1)$ for upper band.

The least-squares solution $\mathbf{A}_{\mathrm{LS}}^{(1)}$ is, therefore, obtained by the pseudo-inversing of the basis matrix $\Psi_{(i)}$ as follows:

$$\mathbf{A}_{\mathrm{LS}}^{(i)} = (\Psi_{(i)}^H \Psi_{(i)})^{-1} \Psi_{(i)}^H \mathbf{u_i} \tag{4.24}$$

where $[.]^H$ is the Hermitian transpose.

The computational complexity of the proposed model is much reduced compared to that of the parallel-MP model, since only the mildly nonlinear dynamic function is multiplied twice by the signal and its conjugate image. Therefore, the number of complex-valued multiplications is significantly decreased. In the parallel-MP model, each input signal and its conjugate image are applied to both the static and dynamic functions of the model's compound structure, which significantly increases the computational complexity of the model. In the proposed model, the mildly nonlinear dynamic function is applied to the output of the 2-D LUTs for the lower and upper bands, without the need to duplicate this function again for each signal and its conjugate image. Since both the proposed and parallel-MP models are linear in terms of their coefficients, a least squares algorithm is used for estimating the model coefficients.

However, the proposed model has added identification complexity than the parallel-MP model. The identification of the proposed model is done in two steps: the first step is the identification of the parallel dual-input Volterra filters. The second step is the de-embedding of the output signals for the identification of the memoryless nonlinear behavior of the 2-D LUT. On the other hand, the identification of the parallel-MP model is done in only one step.

This added identification step adds an extra identification complexity to the proposed model. However, this additional complexity is compensated for with the improved performance of the proposed model and the significant reduction in computational complexity over that of the parallel-MP model as will be shown in the next section.

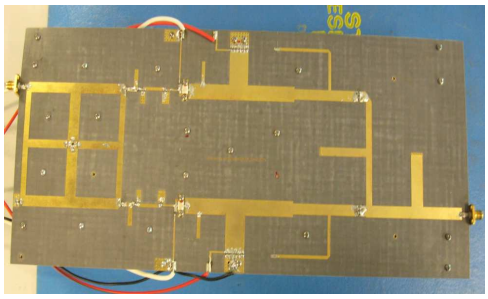

Figure 4.6: Prototype of the Dual-band Doherty PA used for model validation.

4.6 Measurement Setup

4.6.1 Device Under test

The DUT used for model validation is a dual-band Doherty PA designed using a silicon carbide (SiC) metal semiconductor field effect transistor (MESFET) (CREE, CRF24010), the complete design details and performance results are reported [50, 107]. The photo of the prototype used is shown in Fig. 4.6. The DUT operates at two frequency bands, which were set to 880 and 1978 MHz, using a T-network. The T-network acts as a dual band impedance transformer, which makes it possible to realize a concurrent dual band PA and other dual band components.

Both the carrier and peaking PAs employed the same topology of the dual-band PA discussed in [107]. The supply voltages of the carrier and peaking PAs were both initially set to 28 V. The gate bias voltages of the carrier and peaking PAs were set to -9 and -18 V, respectively.

4.6.2 Experimental Test Bench

Fig. 4.7 shows the measurement setup for dual-band Doherty PA characterization and predistortion, which is operated concurrently for dual bands with carrier frequencies of 880 and 1978 MHz. The two input signals are simultaneously downloaded using computer software into two signal generators through a general-purpose interface bus (GPIB) connection. The two signals are then modulated and up-converted to the required carrier frequencies, each through a separate I/Q modulator using two signal generators ESG1 (E4438C) and ESG2 (E4438C), which are time synchronized at baseband. An extra signal generator (ESG 4438B) is used as an external common clock for the two baseband generators to ensure the timing alignment of the baseband signals. Signals are combined using a power combiner (P2S-1.900V) that works in the frequency range from 800 to 3000 MHz. The combined input signal is then amplified via the dual-band PA.

The PA output at each band is individually down-converted and digitized using a vector spectrum analyzer (VSA, E4440A) and captured at two steps, where the VSA is first set to capture the signal at 880 MHz and then to capture the signal at 1978 GHz. These signals are then time aligned with their corresponding input signals for further signal processing and PA linearization, where the time-aligned and normalized input-output data is swapped to extract the inverse modeling function in MATLAB and form the predistorted signals. During the identification step, 10,000 samples of the input signals are used. For the validation step, the whole input waveform (184,320 samples) was utilized to form the predistorted signal. The predistorted signals are then downloaded from the signal generators and applied to the dual-band Doherty PA. Finally, the linearized signals are captured at the output of the

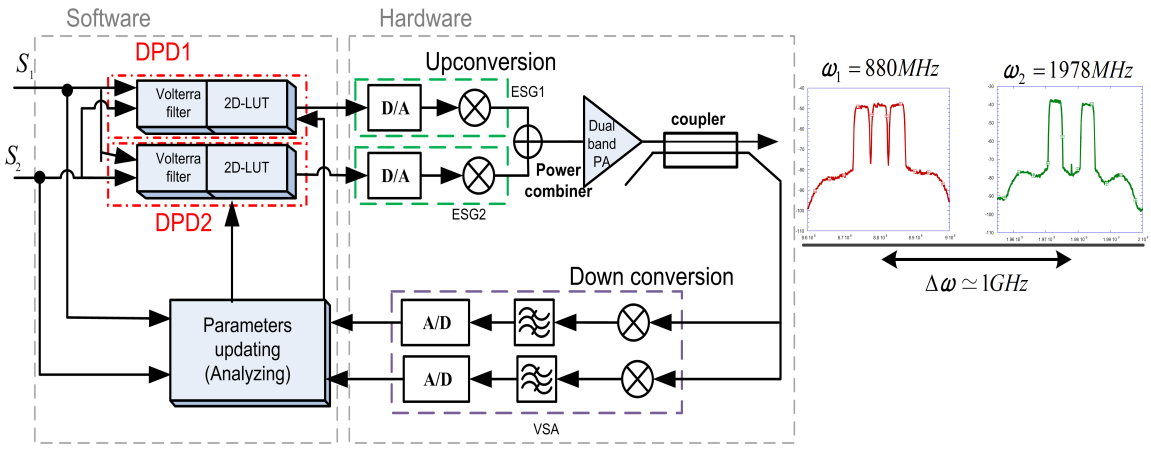

Figure 4.7: Schematic of the dual-band PA characterization and predistortion setup.

dual-band PA using the VSA.

4.7 Measurement and Simulation Results

The accuracy of the proposed dual-input Volterra model was validated by the characterization of the dual-band PA using two different scenarios, one with low-IF signals and the other with baseband signals. Indeed, input signals at a non-zero IF frequency result in an image signal in the image band having high power and must be suppressed. However, the use of zero IF signals (baseband signals) results in image signals that lie in the same band as the desired signals; hence, the I/Q mismatch problem is less obvious than in the case of non-zero IF signals.

- *Scenario* 1

The DUT was driven by two multi-carrier WCDMA signals. A WCDMA111 signal was applied for the lower band (ω_1 = 880 MHz) with a PAPR of 10.6 dB, and a WCDMA101 signal was applied for the upper band (ω_2 = 1978 MHz) with a PAPR of 10.5 dB.

• *Scenario* 2

The DUT was driven by WiMax and LTE signals; the The LTE signal has a bandwidth of 5 MHz and PAPR of 9.8 MHz, and shifted to a low-IF frequency (-5 MHz) and then up-converted to the lower RF frequency ($\omega_1 = 880$ MHz) to be applied to the PA. The WiMax signal has a bandwidth of 5 MHz and PAPR of 9.5 dB, and shifted to a low-IF frequency (+5 MHz), and then up-converter to upper band RF frequency ($\omega_2 = 1978$ MHz) to be applied to the PA.

The tests were carried out for two different I/Q imbalance conditions:

• Case I: Balanced modulators for both the lower and upper bands, with a gain imbalance of 0, a phase imbalance of 0, an I offset of 0, and a Q offset of 0.

• Case II: An imbalanced lower-band modulator with a gain imbalance of 0.8 dB, a phase imbalance of 2 degrees, an I offset of 1%, and a Q offset of 2%; and, an imbalanced upper-band modulator with a gain imbalance of 1 dB, a phase imbalance of 1.5 degrees, an I offset of 1.2%, and a Q offset of 1.2%.

The performance of the proposed dual-input truncated Volterra model, the parallel-MP model, and the 2-D MP model [52] were analyzed and compared through computer simulations for forward modeling and experimental setups for DPD in both cases.

4.7.1 Forward Modeling

The models were used to characterize the DUT for forward behavioral modeling. For *Scenario 1*, using two multi-carrier WCDMA signals for the lower and upper bands, the model dimensions for the 2-D MP model [52] were chosen to be $M = 4$ and $N = 6$. For the parallel-MP model, $M = 4$, and $N_1 = 6$ and $N_2 = 4$ were used for the two parallel branches.

Model ⇓	Number of coefficients
Scenario 1: WCDMA signals	
2-D MP model	140
Parallel-MP model	216
Dual-input Volterra model	112
Scenario 2: Low-IF LTE and WiMax signals	
2-D MP model	112
Parallel-MP model	173
Dual-input Volterra model	76

Table 4.1: Number of coefficients for *Scenarios* I and II

Model ⇓	lower band	upper band
Case I		
2-D MP model	−40.63	−34.18
Parallel-MP model	−41.02	−34.72
Dual-input Volterra model	−41.78	−37.48
Case II		
2-D MP model	−19.89	−16.45
Parallel-MP model	−36.79	−30.44
Dual-input Volterra model	−37.54	−32.53

Table 4.2: NMSE Values in (dB) for *Scenario* 1

Model ⇓	lower band	upper band
Case I		
2-D MP model	−34.13	−33.58
Parallel-MP model	−37.97	−37.78
Dual-input Volterra model	−39.71	−38.12
Case II		
2-D MP model	−27.82	−16.45
Parallel-MP model	−36.68	−34.64
Dual-input Volterra model	−38.34	−36.27

Table 4.3: NMSE Values in (dB) for *Scenario* 2

For the proposed model, the dimensions set for the Volterra filter were $M_1 = 4$ and $M_2 = 5$, and the 2-D LUT was identified using fifth degree polynomial fitting.

For *Scenario 2*, using the low-IF LTE and WiMax signals for the two bands, the model dimensions for the 2-D MP model [52] were chosen to be $M = 3$ and $N = 6$. For the parallel-MP model, $M = 3$, and $N_1 = 6$ and $N_2 = 4$ were used for the two parallel branches. For the proposed model, the dimensions set for the Volterra filter were $M_1 = 2$ and $M_2 = 4$.

In this case, since the WCDMA signals were of wider bandwidth than the LTE and Wimax signals used in *Scenario* 2, a decrease in the memory depth of the system was anticipated, as the drive signal used in *Scenario* 1 are of higher bandwidth. This also highlights the effects of the power distribution within the modulation bandwidth on the memory depth exhibited by the DUT [75].

The model dimensions of the three models are determined using a general sweep method. This general sweep method consists of simultaneously sweeping the model dimensions (non-

linearity order and memory depth) over a wide-enough range. The accuracy of each model is quantified using the normalized mean square error (NMSE) [75] metric. Finally, the model dimensions corresponding to the combination resulting in the lowest number of coefficients that achieves low NMSE are selected.

In Table 4.1, a summary of the number of coefficients for each band of the three models is presented for each scenario. In comparison with the parallel-MP model, the proposed model achieved an almost 50% reduction in the number of coefficients. The proposed model achieved a slight decrease in the number of coefficients compared to the 2-D MP model.

For the accuracy of the model, the NMSE for the three models was evaluated. Tables 4.2 and 4.3 report the NMSE values for the models for the two scenarios. For *Scenario* 1, Case I, with no I/Q imbalance, the 2-D MP [52] and parallel-MP models had similar performances, while the proposed model had an improved NMSE in the two bands, especially in the upper band where a WCDMA101 signal was used. The WCDMA 101 signal created more memory effects than the WCDMA 111 signal, due to the OFF carrier region that represented 33% of the signal bandwidth and suffered from higher memory effects intensity [75].

The parallel-MP and 2-D MP models fell short of characterizing the intense memory effects of the WCDMA 101 signal. This performance deteriorated further with concurrent dual-band operation, due to the added cross-modulation effects. On the other hand, the added memory cross terms of the proposed model improved the characterization of this signal.

For Case II, with induced I/Q imbalance, the 2-D MP model [52] had a very poor NMSE, because the model does not account for I/Q modulator imperfections, which highly degraded the model performance. The two other models achieved better results, because

their compound structures can characterize the I/Q modulator imperfections.

Similarly, in *Scenario* 2, for the low-IF signals, the 2-D MP model has poor performance in comparison to the two other models even in case I with no I/Q imbalance, due to the MFI effects, that will be shown in the linearization section.

The proposed model outperformed the other models in both scenarios, with a significant reduction in the computational complexity. The reported results demonstrate the robustness of the proposed model, as it has achieved better accuracy in characterizing the dynamic nonlinear behavior of the dual-band DUT and the I/Q impairments of the two modulators than the parallel-MP model, due to the added cross terms, which further enhanced the model performance.

The proposed model was also more computationally efficient than the parallel-MP model, as it alleviated the added computational complexity drawbacks of the reported parallel compound structures that compensate for the I/Q impairments by adding a parallel branch for the conjugate image input signal. The proposed model used the conjugate signal input only for identification of the low-order dynamic function and used only one branch for the identification of the high-order nonlinear static function. These results also proved that the structure of the 2-D MP model is incapable of characterizing the dual-band system with I/Q imperfections.

4.7.2 Digital Predistortion

The inverse functions of the 2-D MP, parallel-MP and proposed truncated Volterra models were used as predistorters to linearize the dual-band PA using the indirect learning architecture [73].

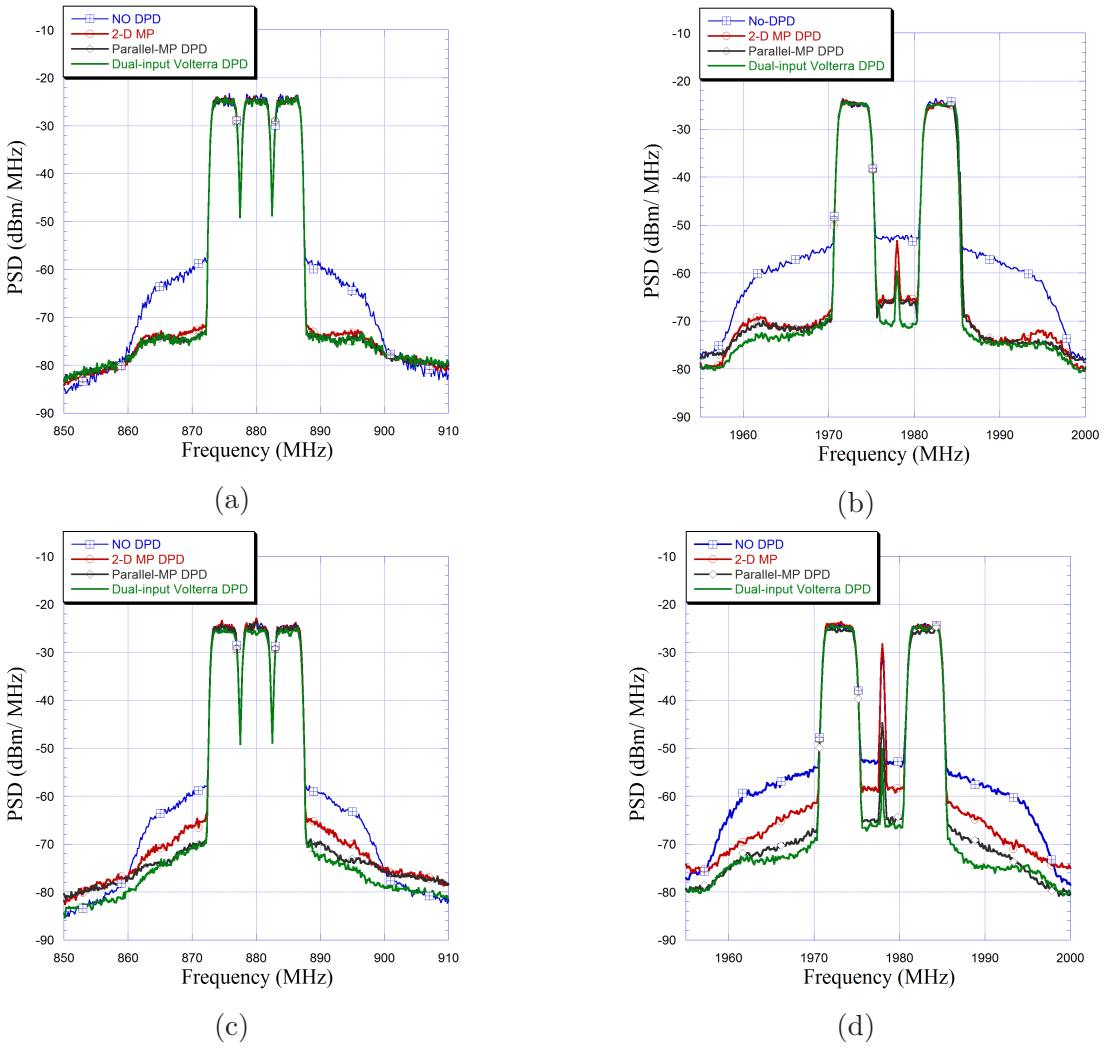

Figure 4.8: Measured PSDs with and without DPD for *Scenario* 1 (a) Case I, the lower-band (WCDMA111), (b) Case I, the upper band (WCDMA101), (c) Case II, the lower band(WCDMA111), (d) Case II, the upper band (WCDMA101).

The results for the three DPD techniques are demonstrated in Table 4.4 and Fig. 4.8 for *Scenario* 1, and in Table 4.5 and Fig. 4.9 for *Scenario* 2, for the two cases of balanced and imbalanced modulators. Results with no DPD are also provided for comparison. Tables 4.4 and 4.5 shows the adjacent channel power ratio (ACPR) in the adjacent channel slots, which are spaced at intervals of +/- 5 MHz, for the two Scenarios.

In Table 4.4, for *Scenario* 1, the ACPR results show that the proposed truncated Volterra

DPD had a better performance in suppressing the out-of-band emission, with an ACPR that reached below -49 dBc, an improvement of around 2 dB over that of the parallel-MP DPD.

The added cross terms improved the mitigation of the in-band and cross-band distortions of the parallel-MP DPD. The results further validate that the 2-D MP DPD cannot suppress the spectral regrowth and DC offsets in Case II (added I/Q imperfections). This was also demonstrated in Fig. 4.8, which shows the PSDs at the output of the linearized PA for the different DPDs and no DPD for Cases I and II. For the balanced I/Q modulators (Case I), the different DPD functions were able to suppress the spectral regrowth at the output of the DUT. The spectral regrowth at the output with no DPD was around -34 dB higher than the in-band spectral level. The figure also shows that the operation of the DUT in concurrent dual-band operation caused severe in-band and out-of-band distortions. For the imbalanced I/Q modulators in both lower and upper bands (Case II), the results in Fig. 4.8 (c and d) demonstrate the capability of the proposed model in further suppressing the spectral regrowth of the dual-band PA, resulting in better linearity performance than those of the other models. This is particularly evident in the close vicinity of the carrier signal, where the spectrum emission mask constraints are tougher to meet, and in the OFF carrier region for the WCDMA101 signal. This further validates previous reports for the modeling of the intense memory behavior emulated by this signal. It was also shown that the proposed and parallel-MP DPD techniques could compensate for the I/Q impairments in the modulator that appear as DC offsets at the carrier frequencies. Similarly, In Fig. 4.9, for *scenario* 2, the I/Q imbalance effects are now more obvious with using low-IF signals. The proposed model for both cases can considerably push the MFI effect down and results in better linearity results. The 2-D MP DPD fell short of suppressing the image band even in Case I, where

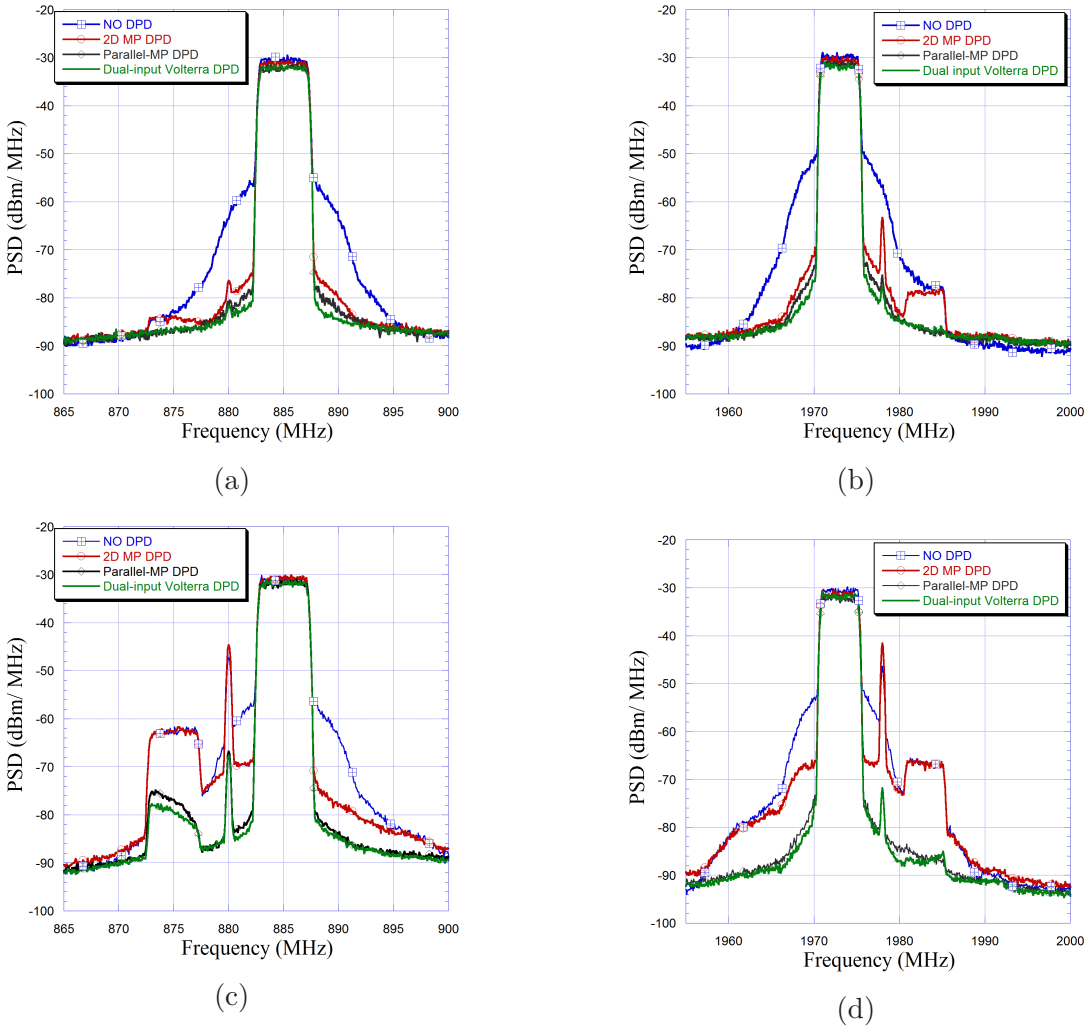

Figure 4.9: Measured PSDs with and without DPD for *Scenario* 2 (a) Case I, the lower-band (LTE signal), (b) Case I, the upper band (WiMax signal), (c) Case II, the lower band (LTE signal), (d) Case II, the upper band (WiMax signal).

there is no induced IQ imbalance, but only the minor IQ imperfections in the VSG is present. This was also apparent in the ACPR results in Table 4.4 and Table 4.5.

In Table 4.6, the Image Rejection Ratio (IRR) [14] which is defined as the ratio of the IF signal level produced by the desired input frequency to that produced by the image frequency, and the DC suppression in dB, are presented for *Scenario* 2 Case II. The results demonstrate that the effectiveness of the proposed DPD in further suppressing the image signal in the image band than the parallel-MP DPD.

DPD ⇓	lower band	upper band
	$-/+5$ MHz	
Case I		
No DPD	$-37.07/-38.76$	$-34.02/-34.94$
2-D MP DPD	$-47.86/-47.73$	$-46.34/-47.21$
Parallel-MP DPD	$-47.57/-48.06$	$-47.02/-47.53$
Dual-input Volterra DPD	$-48.08/-49.10$	$-48.98/-49.26$
Case II		
No DPD	$-34.47/-34.34$	$-30.70/-31.28$
2-D MP DPD	$-40.63/-41.46$	$-37.38/-37.55$
Parallel-MP DPD	$-45.48/-46.9$	$-45.54/-46.41$
Dual-input Volterra DPD	$-48.2/-48.9$	$-47.98/-49.84$

Table 4.4: ACPR Values in (dBc) for the Stated DPDs for *Scenario* 1

Fig. 4.10 shows the PSD of the whole band output captured by the VSA at span of 2 GHz, when excited with the two low-IF signals in *Scenario* 2 Case I, before and after applying the proposed DPD.

The figure shows the inter-band modulation outputs at the two fundamental frequencies (ω_1 and ω_2), as well as the cross-modulation effects at the two bands. Although the proposed DPD is implemented to characterize the PA output around the two carrier frequencies captured at a span of 72 MHz (due to the hardware capabilities), the proposed DPD could further suppress the cross modulation effects at the different frequency bands. It is also worth mentioning that since the frequency spacing between the two bands is more than 1 GHz, then the higher order inter-modulation products will lie far from the two operating frequencies, and could be easily filtered out.

DPD ⇓	lower band	upper band
	$-/+5$ MHz	
Case I		
No DPD	$-33.60/-34.45$	$-31.52/-24.64$
2-D MP DPD	$-46.79/-48.32$	$-46.32/-36.78$
Parallel-MP DPD	$-48.44/-49.50$	$-47.51/-41.29$
Dual-input Volterra DPD	$-50.21/-51.17$	$-48.58/-42.61$
Case II		
No DPD	$-31.82/-34.47$	$-31.04/-23.55$
2-D MP DPD	$-36.23/-45.92$	$-37.28/-27.39$
Parallel-MP DPD	$-49.25/-50.90$	$-47.95/-40.41$
Dual-input Volterra DPD	$-50.01/-51.21$	$-48.43/-41.04$

Table 4.5: ACPR Values in (dBc) for the Stated DPDs for *Scenario* 2

It can be concluded, therefore, that both high-order static nonlinearities and low-order dynamic nonlinearities contribute to the nonlinear distortions caused by a dual-band transmitter. Hence, the separate identification of the higher order static nonlinearity function and the mildly nonlinear dynamic function reduces the model complexity [66, 78]. Indeed, this allows more freedom in characterizing the mildly nonlinear dynamics with a low-order polynomial function, a sufficient memory depth and the addition of extra memory cross terms to enhance the modeling accuracy of the nonlinear memory effects of the system.

Moreover, the I/Q modulator imperfections are characterized in a compound structure with the mild dynamic nonlinearities, which further decreases the model complexity, since the dynamic low-order nonlinear functions are applied twice, once for the signal and once for its conjugate image. This avoids the use of an extra conjugate image branch for the

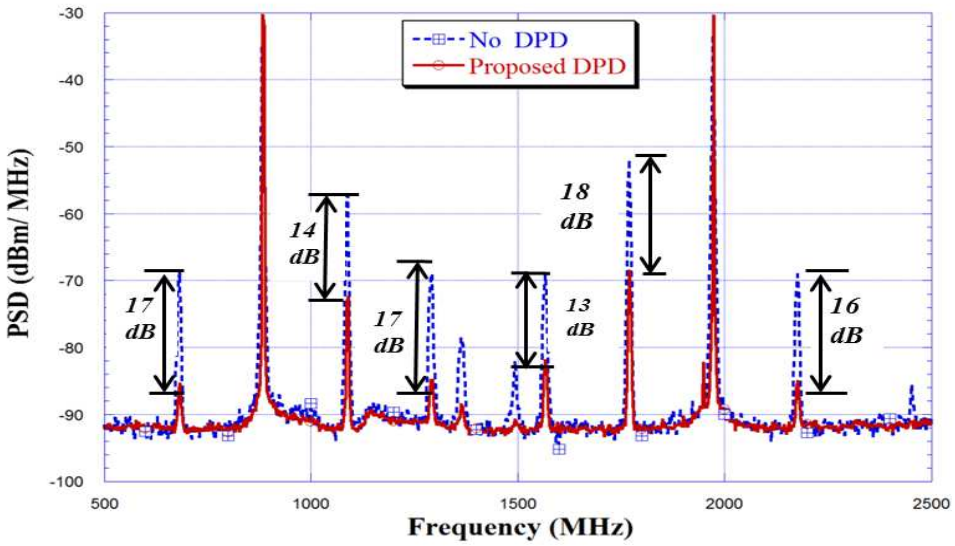

Figure 4.10: PSD of the output waveform of the dual-band Doherty PA before and after applying the proposed dual-input Volterra DPD for *Scenario* 2 Case I.

higher-order nonlinear function, which is applied only once to the output of the first block. Therefore, the number of coefficients and complex multiplications required to implement the model are significantly reduced.

DPD ⇓	IRR		DC suppression	
	LB	UB	LB	UB
Parallel-MP DPD	47.43	54.36	21.03	27.96
Dual-input Volterra DPD	49.46	56.65	21.80	28.81

Table 4.6: IRR and DC suppression in (dBc) for *Scenario* 2 Case II

4.8 Conclusion

In this chapter, a complexity-reduced dual-input truncated Volterra model is proposed for the characterization and digital predistortion of a dual-band transmitter's RF impairments. These impairments include the in-band and cross-band distortion of a concurrent dual-band PA in the presence of I/Q modulator imperfections.

The proposed technique was experimentally assessed by exciting a dual-band Doherty PA with two different scenarios, one with baseband signals and low-IF signals. Indeed, the proposed model showed accurate performance and reduced computational complexity in both cases, as it achieved a reduction of more than 50% in the number of coefficients for the state-of-the art compound parallel MP model. Indeed, it suppressed the MFI effect in the case of low-IF transmitter while the 2-D MP model fell short to suppress. Hence, the added memory effects cross terms of the proposed model further enhanced the characterization of the cross-modulation effects of the dual-band transmitter.

Chapter 5

Digital Predistortion of Concurrent Tri-Band Transmitters using 3-D Phase-Aligned Pruned Volterra Model

5.1 Introduction

Recently, new DPD techniques/models for the concurrent dual-band PAs have been subject to extensive research. In this chapter, the nonlinear distortion and DPD linearization problem in concurrent multi-band PAs, more specifically, in concurrent tri-band communication systems, are addressed. In the concurrent tri-band case, analysis of nonlinearities and DPD linearization are more challenging, since three input signals are involved. Although it is similar to the concurrent dual-band case in which both in-band inter-modulation and cross-band modulation exist in the concurrent tri-band PA. The exact form of the cross-band modulation in this case is more noticeable. This chapter demonstrates the detailed form of the nonlinear behavior of the concurrent tri-band PA for the first time [108].

The analysis is further extended to include the impact of the phase distortion observed in multi-band PAs as well as the compound amplitude distortion. By taking into account the phase variation effects across a wide frequency band, a three-dimensional (3-D) phase-aligned Volterra DPD is proposed. The proposed model can effectively compensate for the cross-talk between the fundamental frequencies, their harmonics and inter-modulation products due to

the nonlinearity exhibited by the tri-band PA.

The remainder of this chapter is organized as follows: An analysis of the tri-band PA nonlinear behavior is presented in Section 5.2 and the validation of the model is presented in Section 5.3. The effect of the phase distortion in wideband transmitters are analyzed in Section 5.4. Section 5.5 presents the structure of the proposed phase-aligned DPD and the model performance assessment. Finally, the conclusions of the chapter are summarized in Section 5.6.

5.2 Nonlinear behavior of concurrent tri-band PA

Fig. 5.1 shows the basic architecture for a concurrent tri-band PA transmitter, where the input signals are sent through three signal processors for modulation and up-conversion, and the combined input is applied then to a multi-band PA.

Polynomial models are widely used for behavioral modeling and digital predistortion of wideband signals [36]. A general structure of a memoryless SISO polynomial bandpass model is given by:

$$y(t) = \sum_{k=1}^{N} a_k x^k(t) \tag{5.1}$$

where N is the polynomial order, a_k is the set of bandpass model coefficients, $y(t)$ is the bandpass model output, and $x(t)$ is the bandpass input.

The bandpass input signal for the tri-band concurrent PA will be given as:

$$x(t) = x_1(t) + x_2(t) + x_3(t) \tag{5.2}$$

where $x_1(t)$, $x_2(t)$, and $x_3(t)$ are the bandpass input signals to the lower, middle, and upper bands at the three angular frequencies ω_1, ω_2, and ω_3, respectively.

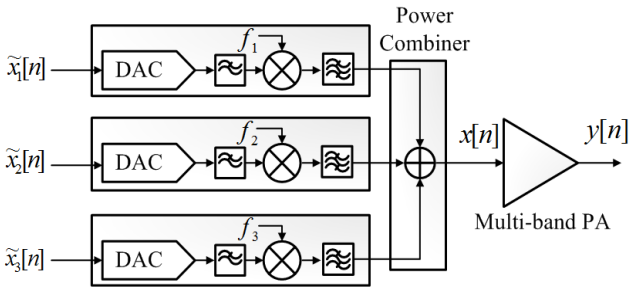

Figure 5.1: Concurrent Tri-band Transmitter Architecture.

By direct mathematical manipulation, the different inter-modulation distortion (IMD) product terms in the different frequency bands can be grouped as follows:

$$\text{IMD}_{\omega_1} = \tilde{x}_1|\tilde{x}_1|^{2k_1}|\tilde{x}_2|^{2k_2}|\tilde{x}_3|^{2k_3}$$

$$\text{IMD}_{\omega_2} = \tilde{x}_2|\tilde{x}_1|^{2k_1}|\tilde{x}_2|^{2k_2}|\tilde{x}_3|^{2k_3}$$

$$\text{IMD}_{\omega_3} = \tilde{x}_3|\tilde{x}_1|^{2k_1}|\tilde{x}_2|^{2k_2}|\tilde{x}_3|^{2k_3}$$

$$\text{IMD}_{2\omega_2-\omega_1} = \tilde{x}_1^*\tilde{x}_2^2|\tilde{x}_1|^{2(k_1-1)}|\tilde{x}_2|^{2k_2}|\tilde{x}_3|^{2k_3}$$

$$\text{IMD}_{2\omega_1-\omega_2} = \tilde{x}_1^2\tilde{x}_2^*|\tilde{x}_1|^{2k_1}|\tilde{x}_2|^{2(k_2-1)}|\tilde{x}_3|^{2k_3}$$

$$\text{IMD}_{2\omega_2-\omega_3} = \tilde{x}_2^2\tilde{x}_3^*|\tilde{x}_1|^{2k_1}|\tilde{x}_2|^{2k_2}|\tilde{x}_3|^{2(k_3-1)}$$

$$\text{IMD}_{2\omega_3-\omega_2} = \tilde{x}_3^2\tilde{x}_2^*|\tilde{x}_1|^{2k_1}|\tilde{x}_2|^{2(k_2-1)}|\tilde{x}_3|^{2k_3}$$

$$\text{IMD}_{2\omega_1-\omega_3} = \tilde{x}_1^2\tilde{x}_3^*|\tilde{x}_1|^{2k_1}|\tilde{x}_2|^{2k_2}|\tilde{x}_3|^{2(k_3-1)}$$

$$\text{IMD}_{2\omega_3-\omega_1} = \tilde{x}_3^2\tilde{x}_1^*|\tilde{x}_1|^{2(k_1-1)}|\tilde{x}_2|^{2k_2}|\tilde{x}_3|^{2k_3}$$

$$\text{IMD}_{\omega_1-\omega_2+\omega_3} = \tilde{x}_1\tilde{x}_2^*\tilde{x}_3|\tilde{x}_1|^{2k_1}|\tilde{x}_2|^{2(k_2-1)}|\tilde{x}_3|^{2k_3}$$

where $(.)^*$ denotes complex conjugate operation and $|.|$ denotes absolute value.

The baseband model around the three fundamental frequencies ω_1, ω_2, and ω_3 was extracted. The other terms could be ignored therein, if they lie beyond the band of interest and

could be filtered out. In [101], the frequency spacing between the three bands was set such that interaction of the middle and upper bands generate the third-order IMD term $\tilde{x}_2^2\tilde{x}_3^*$ that lies in the lower-band, and the IMD product $\tilde{x}_1^*\tilde{x}_2^2$ will lie around the upper-band. Also, the interaction between the three bands will generate the IMD term $\tilde{x}_1\tilde{x}_2^*\tilde{x}_3$ in the middle-band. However, if the frequency spacing between the three bands is wide enough, then these IMD terms will lie far enough from the desired bands and can be ignored.

The memory effects are further added to the fundamental models within the desired bands as follows:

$$\tilde{y}_1(n) = \sum_{m=0}^{M-1}\sum_{i=0}^{N-1}\sum_{s=0}^{i}\sum_{k=0}^{s} a_{misk}\tilde{x}_1(n-m) \times |\tilde{x}_1(n-m)|^{i-s}|\tilde{x}_2(n-m)|^{s-k}|\tilde{x}_3(n-m)|^k \tag{5.3}$$

$$\tilde{y}_2(n) = \sum_{m=0}^{M-1}\sum_{i=0}^{N-1}\sum_{s=0}^{i}\sum_{k=0}^{s} b_{misk}\tilde{x}_2(n-m) \times |\tilde{x}_1(n-m)|^{i-s}|\tilde{x}_2(n-m)|^{s-k}|\tilde{x}_3(n-m)|^k \tag{5.4}$$

$$\tilde{y}_3(n) = \sum_{m=0}^{M-1}\sum_{i=0}^{N-1}\sum_{s=0}^{i}\sum_{k=0}^{s} c_{misk}\tilde{x}_3(n-m) \times |\tilde{x}_1(n-m)|^{i-s}|\tilde{x}_2(n-m)|^{s-k}|\tilde{x}_3(n-m)|^k \tag{5.5}$$

where $\tilde{y}_1(n)$, $\tilde{y}_2(n)$, and $\tilde{y}_3(n)$ are the complex envelopes of the estimated tri-band PA output signals centered around the three fundamental frequencies ω_1, ω_2, and ω_3, respectively. a_{misk}, b_{misk}, and c_{misk} are the model coefficients for the three bands; M and N are the memory depth and the nonlinear order. This model will be referred to as the 3-D tri-band model hereafter.

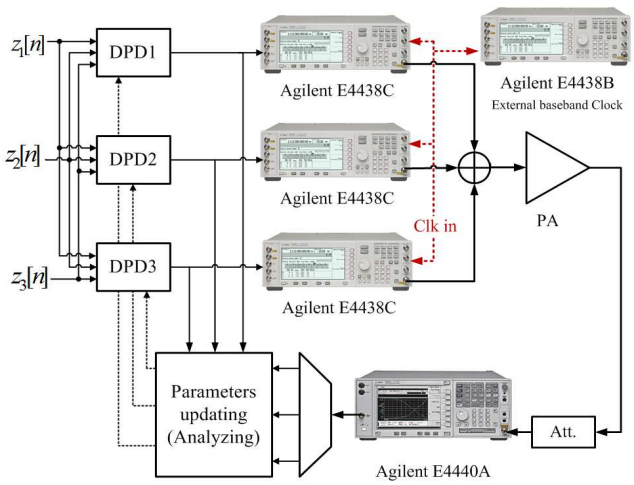

Figure 5.2: Block diagram of the experimental setup used for tri-band transmitter linearization.

5.3 Model Assessment

5.3.1 Experimental Setup for Tri-band linearization

Fig. 5.2 shows a block diagram of the experimental setup used for tri-band PA linearization. The transmitter hardware consists of three signal generators responsible for digital baseband to analog RF up-conversion. Connections between the generators and an external clock generator are made to allow the synchronization of the transmitted bandpass signals.

The DUT used for model validation is a broadband PA biased at class AB. The three signal generators used for sending the signals are time aligned and synchronized using a baseband clock signal generator. Each baseband signal is up-converted to the required RF frequency, and then the three signals were combined using a wideband power combiner and sent to the PA. The output signals were captured by a VSA in three steps, one for each frequency band. The VSA was set to capture the output data at a span of 72 MHz around each carrier frequency. The baseband output signal at each band is individually time aligned

with the respective input baseband signal, where the input and output waveforms were used to form the 3-D tri-band DPD functions in MATLAB.

5.3.2 Experimental Results of 3-D tri-band DPD

For model evaluation three signals were sent concurrently, a 5 MHz LTE signal at 2.14 GHz, a 5 MHz WiMAX signal at 2.425 GHz, and a 5 MHz WCDMA signal at 2.655 GHz, all are operating at sampling frequency of 92.16 MHz. A 10,000 samples interval of the input waveform is used for the model identification step, and the whole input waveform of 184,320 samples is used for the model validation. The DPD coefficients were extracted using the least squares algorithm for $M = 3$ and $N = 5$. Finally, the predistorted signals were re-sent using the described setup to capture the linearized signals at the output of the tri-band PA. Fig. 5.3 shows the PSD of the signals centered at the three carrier frequencies. The figure shows the PSD of the distorted output signals at the output of the PA in tri-band concurrent mode without applying predistortion. It also shows the linearized signals using a single-input single-output MP DPD [36] and the proposed 3-D tri-band DPD given by (5.3)-(5.5). Fig. 5.3 demonstrates that the MP DPD is incapable of suppressing the distortion resulting from the cross-modulation/cross-talk effect and inter-modulation products of the tri-band PA, as it accounts for the nonlinear effects of one band only. Indeed, the 3-D tri-band DPD has effectively suppressed the spectral distortion in the adjacent channels. Table 5.1 shows the ACPR in dBc for the adjacent channels spaced at -/+ 5 MHz intervals. The ACPR results for the tri-band DPD are approximately around 49 dBc for the three channels. However, the individual MP DPD did not satisfy the spectral emission mask for any of the three standard signals.

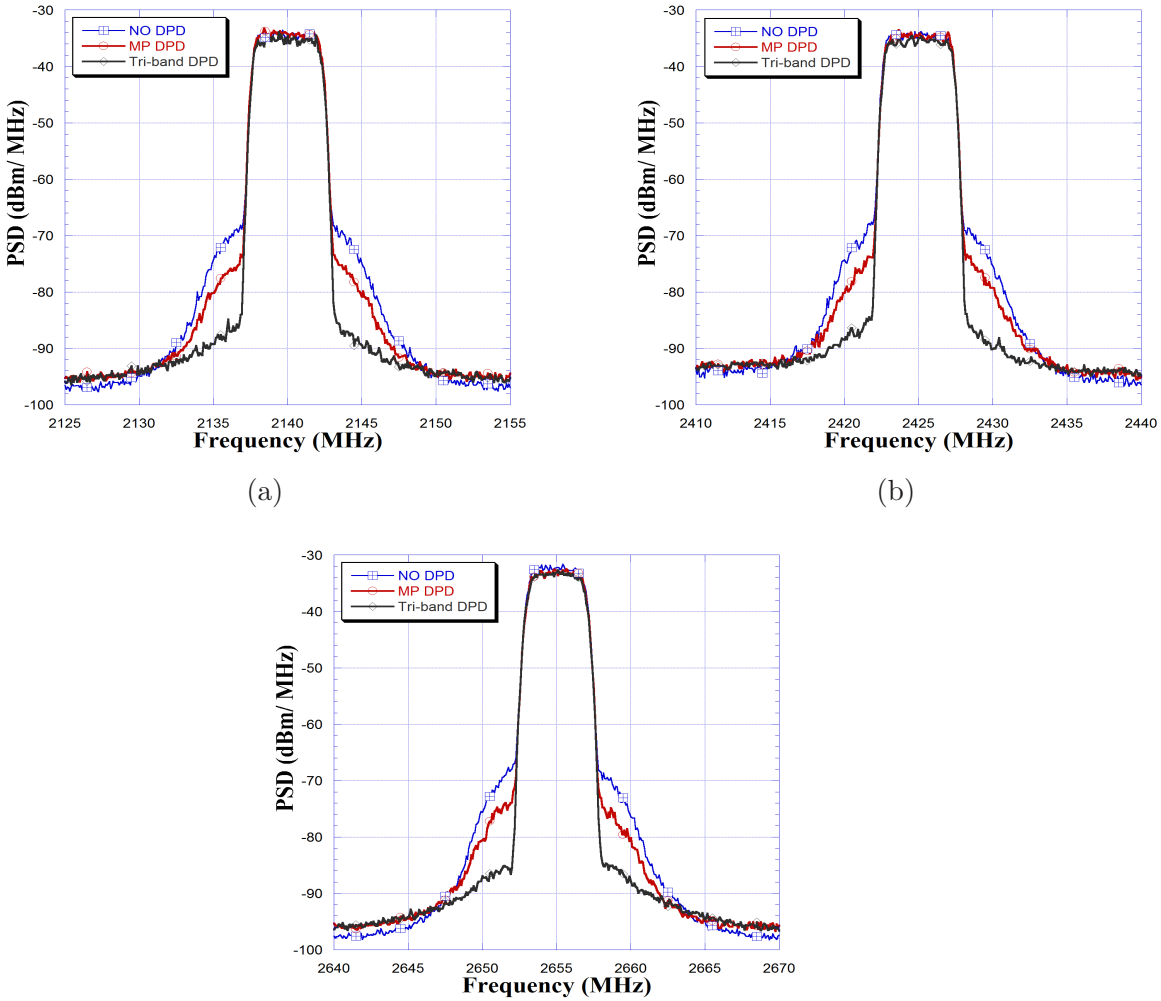

(a) (b)

(c)

Figure 5.3: Measured output spectra with and without DPD. (a) LTE signal at 2.14 GHz (b) WiMAX signal at 2.425 GHz (c) WCMDA signal at 2.655 GHz.

5.4 Limitations of previously reported Multi-band DPDs

The major drawback of the previously reported 3-D tri-band DPD and also the reported dual-band DPD cells that were discussed in literature [51,52,97–101,106], that they only account for the main amplitude modulation to amplitude modulation (AM-AM) and amplitude modulation to phase modulation (AM-PM) dynamic behavior of the multi-band PA. Hence, the output of each band relies on the compound amplitude of the input signal complex enve-

DPD	LB @2.14 GHz	MB @2.425 GHz	UB @2.655 GHz
	-/+5 MHz		
No-DPD	−34.4/−33.6	−33.8/−34.1	−33.7/−33.8
MP DPD	−41.2/−38.6	−40.8/−39.1	−41.3/−40.3
3-D tri-band DPD	−49.2/−49.1	−48.8/−49.2	−49.5/−48.8

Table 5.1: ACPR values in (dBc) for the Stated DPDs

lope, and the memory effects are incorporated only in the envelope amplitude. However, the effect of the instantaneous or past phase information from the other bands is not considered.

This issue was raised for single-band transmitters in [109], where the effects of the phase distortion on single-band wireless transmitters is analyzed and an artificial neural network (ANN) model is proposed that takes into account the effects of the phase modulation to amplitude modulation (PM-AM) and phase modulation to phase modulation (PM-PM) distortion due to linear filtering. Other Volterra models that take into account the PM-AM and PM-PM behavior of single-band transmitters were proposed in [76, 77, 110].

In the case of multi-band transmitters, this problem is more obvious. However, no previous work on multi-band transmitters has accounted for the phase variation across wideband frequency interval between multiple signals driving the transmitter. Therefore, in this work, the impact of the phase distortion as well as the dynamic amplitude distortion across three bands is investigated, and their impact on the accuracy of linearization is validated in a concurrent tri-band transmitter.

The proposed model in the following sections is an extended version of the 3-D tri-band DPD, where the analysis of the static and dynamic behavior of the tri-band PA is extended

to include the effects of the phase and amplitude information of the three signals on the output. Thus, a 3-D phase-aligned pruned Volterra model is proposed for accurate modeling and predistortion of the dynamic behavior of a concurrent tri-band PA suitable for CA in LTE-Advanced system.

5.4.1 Phase distortion effects in multi-band transmitters

The nonlinear behavior of PAs changes across a wide frequency range. In [109], it was shown that since wideband signals invalidate the assumption of constant phase in narrow band operated systems, i.e., signals that occupy a very small bandwidth compared to the bandwidth of the transmitter. Thus, they will suffer from phase distortion effects that manifest themselves as PM-AM and PM-PM behavior due to linear filtering. Indeed, the non-flat frequency response of the wireless transmitter system will cause these phase variation effects.

Multi-band transmitters are subject to multi-carrier signals applied concurrently in different frequency bands as shown in Fig. 5.1. The gain and phase response of the transmitter will change across the entire operating bandwidth of the different frequency bands, since the increase in frequency bandwidth tends to deteriorate the group delay [12]. Fig. 5.4 depicts the measured group delay for a multi-band transmitter across a wide frequency band. Therefore, with the wider bandwidths of multi-carrier signals, the non-constant group delay will cause phase variation over the whole operating frequency band that should be accounted for. Indeed, the variation of the phase over frequency between the different bands will give rise to phase distortion effects, as well as dynamic amplitude distortion effects represented by the AM-AM and AM-PM characteristics. Therefore, in order to accurately represent a multi-

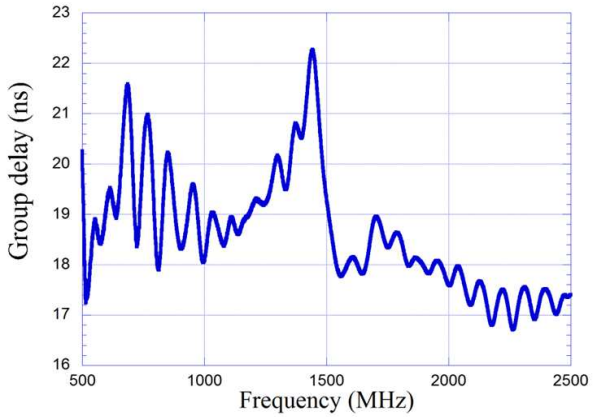

Figure 5.4: Measured group delay across the multi-band transmitter.

band transmitter, the model requires past information on the compound amplitude of the input envelope signals as well as phase differences between the different multi-input complex envelopes in order to account for the non-constant delay of the multi-band transmitter.

The previously described 3-D tri-band model in [108] has no past information of the phases of the different inputs. For example, the estimated output of Band 1 at angular carrier frequency ω_1 only relies on the past information of the compound envelope of the three input signals and the phase of the input signal in Band 1. Since, there is no instantaneous or past information of the phases of the inputs from Band 2 and Band 3, the model cannot account for the phase variation contributed by these two other bands.

In the next section, a static model of the tri-band PA is given, and the effect of the phase variation contributed by the different bands is analytically derived and accounted for by the proposed model.

5.5 Proposed Phase-Aligned Volterra DPD

5.5.1 Model Architecture

A truncated Volterra model for SISO transmitters in [77], which is a third-order, finite memory system, is given by:

$$\begin{aligned} y(n) = &\sum_{q=0}^{M_1} H_1(q)x(n-q) \\ &+ \sum_{q=0}^{M_1}\sum_{l=0}^{M_2} H_2(q,l)x(n-q)x(n-l) \\ &+ \sum_{q=0}^{M_1}\sum_{l=0}^{M_2}\sum_{m=0}^{M_3} H_3(q,l,m)x(n-q)x(n-l)x(n-m) \end{aligned} \tag{5.6}$$

where $y(n)$ and $x(n)$ are the pass-band single-output and single-input signals, respectively. $H_p(...)$ are the Volterra kernels for nonlinearity order P and different delay lengths.

The general Volterra model generates a large number of coefficients that increases exponentially with the degree of nonlinearity P and memory depth M of the system. Due to the complexity of the model, it is mostly limited to modeling mildly nonlinear systems. Therefore, different complexity-reduced Volterra models are proposed in the literature [66, 76–78]. In this analysis, the simplified Volterra model can be expressed as follows:

$$y(n) = y_{\mathrm{s}}(n) + y_{\mathrm{d}}(n) \tag{5.7}$$

where $y_{\mathrm{s}}(n)$ represents the static behavior of the PA, and $y_{\mathrm{d}}(n)$ represents the dynamic nonlinearity of the system.

Separate identification of the higher order static nonlinearity function and the mildly nonlinear dynamic function reduces the model complexity [66, 78]. Indeed, this allows more freedom in characterizing the mildly nonlinear dynamics with a low-order polynomial func-

tion with sufficient memory depth, and the addition of extra memory cross terms to enhance the modeling accuracy of the nonlinear memory effects of the system, with lower complexity than the general Volterra model given by (5.6).

The static function $y_{\mathrm{s}}(n)$ can be expressed by a power series assumption, while the mildly nonlinear dynamic function $y_{\mathrm{d}}(n)$ can be expressed as shown in [77]. The simplified dynamic Volterra filter, where only the bi-dimensional second-order cross terms, i.e., the products with two different time delays and with arbitrary order of nonlinearities, is given by:

$$y_{\mathrm{d}}(n) = \sum_{p=0}^{P} \sum_{i_1=0}^{M_1-1} \sum_{i_2=i_1+1}^{M_2-1} H_p(i_1, i_2) x^p(n-i_1) x(n-i_2) \tag{5.8}$$

where M_1 and M_2 are the memory depths of the second-order cross terms.

Therefore, the total output of the SISO simplified Volterra model, given by the summation of static and dynamic functions in (5.7), is as follows:

$$\begin{aligned} y(n) = & \sum_{p=1}^{P} H_p(0) x^p(n) \\ & + \sum_{p=0}^{P} \sum_{i_1=0}^{M_1-1} \sum_{i_2=i_1+1}^{M_2-1} H_p(i_1, i_2) x^p(n-i_1) x(n-i_2) \end{aligned} \tag{5.9}$$

where $H_p(0)$ and $H_p(i_1, i_2)$ are the bandpass coefficients of the static and dynamic functions, respectively.

The baseband static function $\tilde{y}_{\mathrm{s}}(n)$ for the tri-band case as previously derived in [108], is given as:

$$\begin{aligned} \tilde{y}_{\mathrm{s},q}(n) = & \sum_{p=0}^{N-1} \sum_{s=0}^{p} \sum_{k=0}^{s} h_{p,s,k}^{(q)} \tilde{x}_q(n) \\ & \times |\tilde{x}_q(n)|^{p-s} |\tilde{x}_j(n)|^{s-k} |\tilde{x}_l(n)|^k \end{aligned} \tag{5.10}$$

where $h_{p,s,k}^{(q)}$ is the set of baseband coefficients of the static part around angular frequency ω_q, and $q, j, l \in \{1, 2, 3\}$, where $q \neq j \neq l$.

For the dynamic part, if we substitute the tri-band input for $x(n)$ in (5.9), the dynamic function $y_{\mathrm{d}}(n)$ will be given as:

$$\begin{aligned} y_{\mathrm{d}}(n) = & \sum_{p=0}^{P} \sum_{i_1=0}^{M_1-1} \sum_{i_2=i_1+1}^{M_2-1} H_p(i_1, i_2) \\ & \times [x_1(n-i_1) + x_2(n-i_1) + x_3(n-i_1)]^p \\ & \times [x_1(n-i_2) + x_2(n-i_2) + x_3(n-i_2)] \end{aligned} \tag{5.11}$$

The baseband version of this bandpass dynamic model considers only the frequency components of the output at the three fundamental frequencies. The baseband bi-dimensional dynamic function is derived in Appendix B and is stated as:

$$\begin{aligned} \tilde{y}_{\mathrm{d},q}(n) = & \sum_{g=1}^{3} \sum_{i_1=0}^{M_1-1} \sum_{i_2=i_1+1}^{M_2-1} \boldsymbol{\psi}_{g,i_1,i_2}^{(q)}[\tilde{x}_q(n), \tilde{x}_j(n), \tilde{x}_l(n)] \\ & \times \sum_{p=0}^{N-3} \sum_{s=0}^{p} \sum_{k=0}^{s} h_{p,s,k,g}(i_1, i_2) F_{p,s,k,i_1}[\tilde{x}_q(n), \tilde{x}_j(n), \tilde{x}_l(n)] \end{aligned} \tag{5.12}$$

where $F_{p,s,k,i_1}[\tilde{x}_q(n), \tilde{x}_j(n), \tilde{x}_l(n)]$ is the compound envelope function given by:

$$\begin{aligned} & F_{p,s,k,i_1}[\tilde{x}_q(n), \tilde{x}_j(n), \tilde{x}_l(n)] = \\ & \qquad |\tilde{x}_q(n-i_1)|^{p-s} |\tilde{x}_j(n-i_1)|^{s-k} |\tilde{x}_l(n-i_1)|^k \end{aligned} \tag{5.13}$$

and $\boldsymbol{\psi}_{g,i_1,i_2}^{(q)}[\tilde{x}_q(n), \tilde{x}_j(n), \tilde{x}_l(n)]$ is given by:

$$\boldsymbol{\psi}_{1,i_1,i_2}^{(q)} = \tilde{x}_q^2(n-i_1) \tilde{x}_q^*(n-i_2)$$

$$\boldsymbol{\psi}_{2,i_1,i_2}^{(q)} = \tilde{x}_q(n-i_1) \tilde{x}_j^*(n-i_2) \tilde{x}_j(n-i_1)$$

$$\boldsymbol{\psi}_{3,i_1,i_2}^{(q)} = \tilde{x}_q(n-i_1) \tilde{x}_l^*(n-i_2) \tilde{x}_l(n-i_1)$$

As shown in Appendix B, the pass-band Volterra model has no even-order terms. However, even-order terms can be considered in the baseband representation as reported in [74]

in order to enhance the basis set, thus reducing the modeling error. Therefore, in this work the even-order terms are included in all the derivations.

Therefore, the total baseband model output is the summation of (5.10) and (5.12) as follows:

$$\tilde{y}_q(n) = \tilde{y}_{\mathrm{s},q}(n) + \tilde{y}_{\mathrm{d},q}(n) \tag{5.14}$$

where $\tilde{y}_q(n)$ is the estimated model output around the fundamental frequency ω_q, and $q \in \{1, 2, 3\}$.

If the analysis is extended to include tri-dimensional third-order cross terms, the bandpass tri-dimensional dynamic function will be expressed as:

$$\begin{aligned} y_{\mathrm{d}}(n) = & \sum_{p=0}^{P} \sum_{i_1=0}^{M_1-1} \sum_{i_2=i_1+1}^{M_2-1} \sum_{i_3=i_2+1}^{M_3-1} H_p(i_1, i_2, i_3) \\ & \times x^p(n-i_1)x(n-i_2)x(n-i_3) \end{aligned} \tag{5.15}$$

where $H_p(i_1, i_2, i_3)$ is the set of bandpass coefficients of the tri-dimensional dynamic function.

In case of tri-band system, the tri-dimensional dynamic function can be extended as previously and is given by:

$$\begin{aligned} \tilde{y}_{\mathrm{d},q}(n) = & \sum_{g=1}^{6} \sum_{i_1=0}^{M_1-1} \sum_{i_2=i_1+1}^{M_2-1} \sum_{i_3=i_2+1}^{M_3-1} \boldsymbol{\psi}^{(q)}_{g,i_1,i_2,i_3}[\tilde{x}_q(n), \tilde{x}_j(n), \tilde{x}_l(n)] \\ & \times \sum_{i=0}^{N-5} \sum_{s=0}^{p} \sum_{k=0}^{s} h_{p,s,k,g}(i_1, i_2, i_3) F_{p,s,k,i_1}[\tilde{x}_q(n), \tilde{x}_j(n), \tilde{x}_l(n)] \end{aligned} \tag{5.16}$$

where $F_{p,s,k,i_1}[\tilde{x}_q(n), \tilde{x}_j(n), \tilde{x}_l(n)]$ is defined in (5.13) and $\boldsymbol{\psi}^{(q)}_{g,i_1,i_2,i_3}[\tilde{x}_q(n), \tilde{x}_j(n), \tilde{x}_l(n)]$ for tri-

dimensional case is given by:

$$\boldsymbol{\psi}^{(q)}_{1,i_1,i_2,i_3} = \tilde{x}^3_q(n-i_1)\tilde{x}^*_q(n-i_2)\tilde{x}^*_q(n-i_3)$$

$$\boldsymbol{\psi}^{(q)}_{2,i_1,i_2,i_3} = \tilde{x}^2_q(n-i_1)\tilde{x}_j(n-i_1)\tilde{x}^*_q(n-i_2)\tilde{x}^*_j(n-i_3)$$

$$\boldsymbol{\psi}^{(q)}_{3,i_1,i_2,i_3} = \tilde{x}^2_q(n-i_1)\tilde{x}_l(n-i_1)\tilde{x}^*_q(n-i_2)\tilde{x}^*_l(n-i_3)$$

$$\boldsymbol{\psi}^{(q)}_{4,i_1,i_2,i_3} = \tilde{x}_q(n-i_1)\tilde{x}_j(n-i_1)\tilde{x}_l(n-i_1)\tilde{x}^*_j(n-i_2)\tilde{x}^*_l(n-i_3)$$

$$\boldsymbol{\psi}^{(q)}_{5,i_1,i_2,i_3} = \tilde{x}_q(n-i_1)\tilde{x}^2_j(n-i_1)\tilde{x}^*_j(n-i_2)\tilde{x}^*_j(n-i_3)$$

$$\boldsymbol{\psi}^{(q)}_{6,i_1,i_2,i_3} = \tilde{x}_q(n-i_1)\tilde{x}^2_l(n-i_1)\tilde{x}^*_l(n-i_2)\tilde{x}^*_l(n-i_3)$$

Note that the tri-dimensional dynamic function can generate other combinations of memory terms, such as $\tilde{x}^2_q(n-i_1)\tilde{x}_j(n-i_1)\tilde{x}^*_q(n-i_3)\tilde{x}^*_j(n-i_2)$ and $\tilde{x}_q(n-i_1)\tilde{x}_j(n-i_1)\tilde{x}_l(n-i_1)\tilde{x}^*_j(n-i_3)\tilde{x}^*_l(n-i_2)$, but only essential dominant terms are considered herein.

Hence, the tri-dimensional dynamic output will be the summation of (5.12) and (5.16). It is shown from these equations that accurate representation of the multi-band transmitter output requires past information on the compound amplitude of the complex envelopes of the multi-input signals, as well as past information on the phase differences between the complex envelopes of the input signals as analytically derived. This derivation indicates that the previously reported model in [108], which only depends on the compound amplitude of the input signals and neglects any phase information on the input signals, is incapable of the accurate and true representation of the full dynamics of the multi-band transmitter and hinders the full capacity of the model. In the next section, the analytical derivation is also experimentally validated, and shows that accounting for the non-constant group delay and phase variation across a wide frequency band where the channels fall plays an important role in multi-band systems.

5.5.2 Model Identification

The proposed DPD is linear with respect to its coefficients, as demonstrated in the previous section. Under the assumption of stationarity, if the coefficients are extracted with respect to a minimum mean or square-error criterion, a single global minimum can be achieved. Therefore, direct linear system identification algorithms, e.g., least squares (LS) or recursive least squares (RLS), can be used for estimating the model coefficients; which is defined as linear weighting of the nonlinear signals. In this work the LS estimation technique is used, as will be shown in the next section.

Based on the indirect learning architecture [73], the model coefficients of the proposed DPD are calculated by swapping the input and output signals of the model in order to extract the inverse function of the DPD, as shown in:

$$\begin{aligned}
\tilde{x}_1(n) = & \sum_{p=0}^{N-1}\sum_{s=0}^{p}\sum_{k=0}^{s} h^{(1)}_{p,s,k,0}(0)\tilde{z}_1(n)|\tilde{z}_1(n)|^{p-s}|\tilde{z}_2(n)|^{s-k}|\tilde{z}_3(n)|^{k} \\
& + \sum_{p=0}^{N-3}\sum_{s=0}^{p}\sum_{k=0}^{s}\sum_{i_1=0}^{M_1-1}\sum_{i_2=i_1+1}^{M_2-1} h^{(1)}_{p,s,k,1}(i_1,i_2)\tilde{z}_1^2(n-i_1)\tilde{z}_1^*(n-i_2) \\
& \qquad \times |\tilde{z}_1(n-i_1)|^{p-s}|\tilde{z}_2(n-i_1)|^{s-k}|\tilde{z}_3(n-i_1)|^{k} \\
& + \sum_{p=0}^{N-3}\sum_{s=0}^{p}\sum_{k=0}^{s}\sum_{i_1=0}^{M_1-1}\sum_{i_2=i_1+1}^{M_2-1} h^{(1)}_{p,s,k,2}(i_1,i_2)\tilde{z}_1(n-i_1)\tilde{z}_2^*(n-i_2)\tilde{z}_2(n-i_1) \\
& \qquad \times |\tilde{z}_1(n-i_1)|^{p-s}|\tilde{z}_2(n-i_1)|^{s-k}|\tilde{z}_3(n-i_1)|^{k} \\
& + \sum_{p=0}^{N-3}\sum_{s=0}^{p}\sum_{k=0}^{s}\sum_{i_1=0}^{M_1-1}\sum_{i_2=i_1+1}^{M_2-1} h^{(1)}_{p,s,k,3}(i_1,i_2)\tilde{z}_1(n-i_1)\tilde{z}_3^*(n-i_2)\tilde{z}_3(n-i_1) \\
& \qquad \times |\tilde{z}_1(n-i_1)|^{p-s}|\tilde{z}_2(n-i_1)|^{s-k}|\tilde{z}_3(n-i_1)|^{k} \qquad (5.17)
\end{aligned}$$

where, $\tilde{x}_1(n)$ is the complex baseband predistorted signal around ω_1, while $\tilde{z}_1(n)$, $\tilde{z}_2(n)$, and $\tilde{z}_3(n)$ are the complex baseband inputs of the three DPD cells. As shown in (5.17), only the

dynamic terms resulting from the bi-dimensional assumption are included in order to keep the model at acceptable complexity. The DPD functions of the predistorted signals $\tilde{x}_2(n)$ around ω_2 and $\tilde{x}_3(n)$ around ω_3, are formulated similarly.

The LS estimation solution is formulated as follows:

$$\mathbf{x_1} = \Phi_{(1)}\mathbf{h}^{(1)} \tag{5.18}$$

where $\mathbf{x_1}$ is the estimated output vector of the proposed tri-band DPD at the lower band ω_1, $\Phi_{(1)}$ is the matrix constructed using the basis functions defined in (5.17) and their input signals, and $\mathbf{h}^{(1)}$ is the vector of the polynomial coefficients around ω_1. The vectors are defined as follows:

$$\begin{aligned}
\mathbf{x_1} &= [\tilde{x}_1(1), \tilde{x}_1(2), \cdots, \tilde{x}_1(K)]^T \\
\mathbf{h}^{(1)} &= \Big[h^{(1)}_{0,0,0,0}(0), \cdots, h^{(1)}_{N-1,N-1,N-1,0}(0), \\
&\qquad h^{(1)}_{0,0,0,1}(0,1), \cdots, h^{(1)}_{N-3,N-3,N-3,1}(M_1-1, M_2-1), \\
&\qquad h^{(1)}_{0,0,0,2}(0,1), \cdots, h^{(1)}_{N-3,N-3,N-3,2}(M_1-1, M_2-1), \\
&\qquad h^{(1)}_{0,0,0,3}(0,1), \cdots, h^{(1)}_{N-3,N-3,N-3,3}(M_1-1, M_2-1)\Big]^T
\end{aligned}$$

where K is the length of the input samples training sequence used for identification.

The least-squares solution $\mathbf{h}^{(1)}_{\mathrm{LS}}$ is, therefore, obtained by the pseudo-inversing of the basis matrix as follows:

$$\mathbf{h}^{(1)}_{\mathrm{LS}} = \Phi^{\#}_{(1)}\mathbf{x_1} \tag{5.19}$$

where $\Phi^{\#}_{(1)} = (\Phi^H_{(1)}\Phi_{(1)})^{-1}\Phi^H_{(1)}$ is the pseudo-inverse of the matrix $\Phi_{(1)}$, and $[.]^H$ is the Hermitian transpose. The coefficient vectors $\mathbf{h}^{(2)}_{\mathrm{LS}}$ and $\mathbf{h}^{(3)}_{\mathrm{LS}}$ around ω_2 and ω_3, are estimated similarly.

5.5.3 Experimental Results of the 3-D phase-aligned DPD

In order to validate the proposed DPD, three signals were sent concurrently, a two-carrier LTE signal of bandwidth 8 MHz and PAPR 9.4 dB was sent at the lower frequency band 1.842 GHz (z_1); a one-carrier LTE signal of bandwidth 5 MHz and PAPR 9.5 dB located at middle frequency band 1.96 GHz (z_2); and a three-carrier LTE signal with a middle off-carrier, of total bandwidth 14 MHz and PAPR 9.7 dB at the upper frequency band 2.14 GHz (z_3), using the experimental setup described in Fig. 5.2. All three signals had a baseband sampling frequency (f_s) of 92.16 MHz. A 10,000 samples interval of the input waveform is used for the model identification step, and the whole input waveform of 184,320 samples is used for the model validation. The inverse functions of the 3-D tri-band MP model in [108] and the proposed 3-D phase-aligned pruned Volterra model given by (5.17) were used as predistorters to linearize the wideband PA using the indirect learning architecture [73].

The implemented DPDs were first trained using different model dimensions, i.e. memory depth and nonlinearity order, and then validated by calculating the normalized mean square error (NMSE) for the inverse modeling of the PA. Fig. 5.5 depicts the NMSE results versus the number of coefficients utilized by the two models for the lower, upper, and middle bands, respectively, which indicates the computational complexity of the models. It is observed that the proposed model enhances the modeling accuracy of the PA for the three bands even at the same or lower level of complexity.

The results for the DPD techniques are demonstrated in Table 5.2 and Fig. 5.6. Fig. 5.6 shows the PSD of the multi-carrier linearized LTE signals centered at the lower, middle, and upper frequency bands, respectively, for both the 3-D tri-band DPD and the proposed DPD.

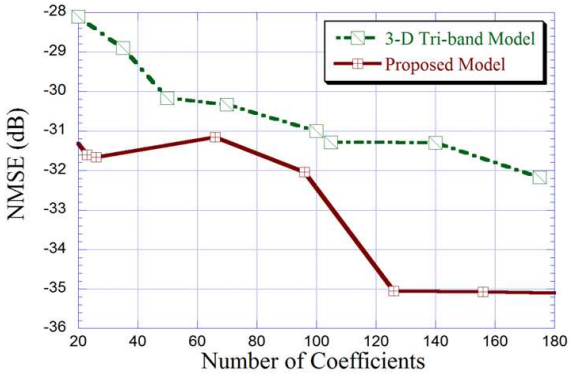

(a)

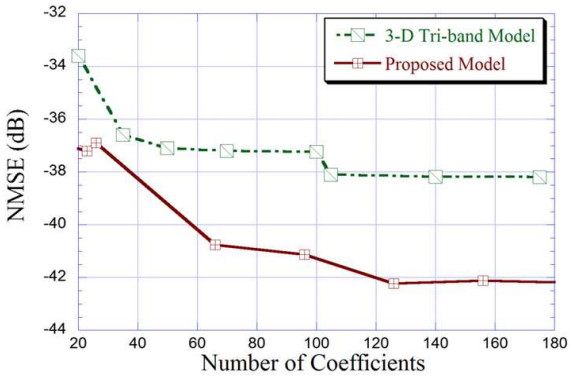

(b)

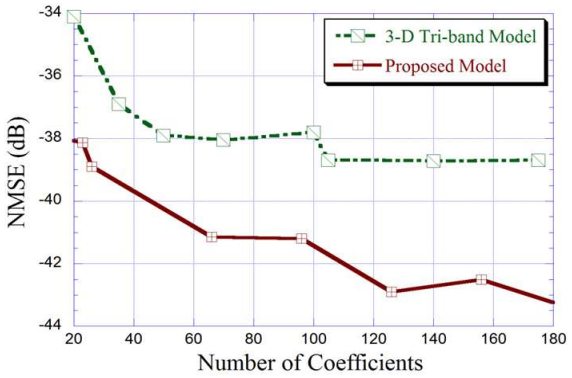

(c)

Figure 5.5: Inverse NMSE versus the number of coefficients. (a) Lower band. (b) Middle band. (c) Upper band.

The blue curves in figure show the PSD of the distorted output signals without applying predistortion.

Table 5.2 shows that the proposed DPD which accounts for the phase difference effects, has significant improvement in suppressing the spectral regrowth at the three carrier frequencies than the 3-D tri-band DPD, especially at adjacent channels where the cross-modulation effects of the input signals appear. This ACPR results in Table 5.2 are for the adjacent channel slots, which are spaced at intervals of +/−5 MHz, +/−10 MHz, and +/−15 MHz for the three bands.

Table 5.3 presents the model dimensions and number of coefficients used by the two DPDs. According to Fig. 5.5, the model dimensions of the two DPDs were chosen corresponding to the best NMSE results obtained with acceptable complexity. A slight increase in number of coefficients is observed for the proposed 3-D phase-aligned Volterra DPD in comparison to the 3-D tri-band DPD. However, this increase in number of coefficients is compensated for by the enhanced performance in suppressing the spectral regrowth due to the cross-modulation effects as shown in Fig. 5.6. Fig. 5.7 shows the PSD of the output over the whole band between 1750 MHz and 2250 MHz when excited with the three concurrent carrier aggregated LTE signals. The three signals have unequal power levels due to the frequency response of the PA. The figure shows the multi-band transmitter output with no DPD applied, where it shows the inter-band distortion around the three carrier frequencies as well as the higher-order IMD products around the three bands. By applying the proposed 3-D phase-aligned DPD and the 3-D tri-band DPD, the in-band linearization of more than 15 dB spectral regrowth suppression around the three fundamental frequencies is achieved, as shown previously in Fig. 5.6. Although the proposed DPD is implemented to characterize

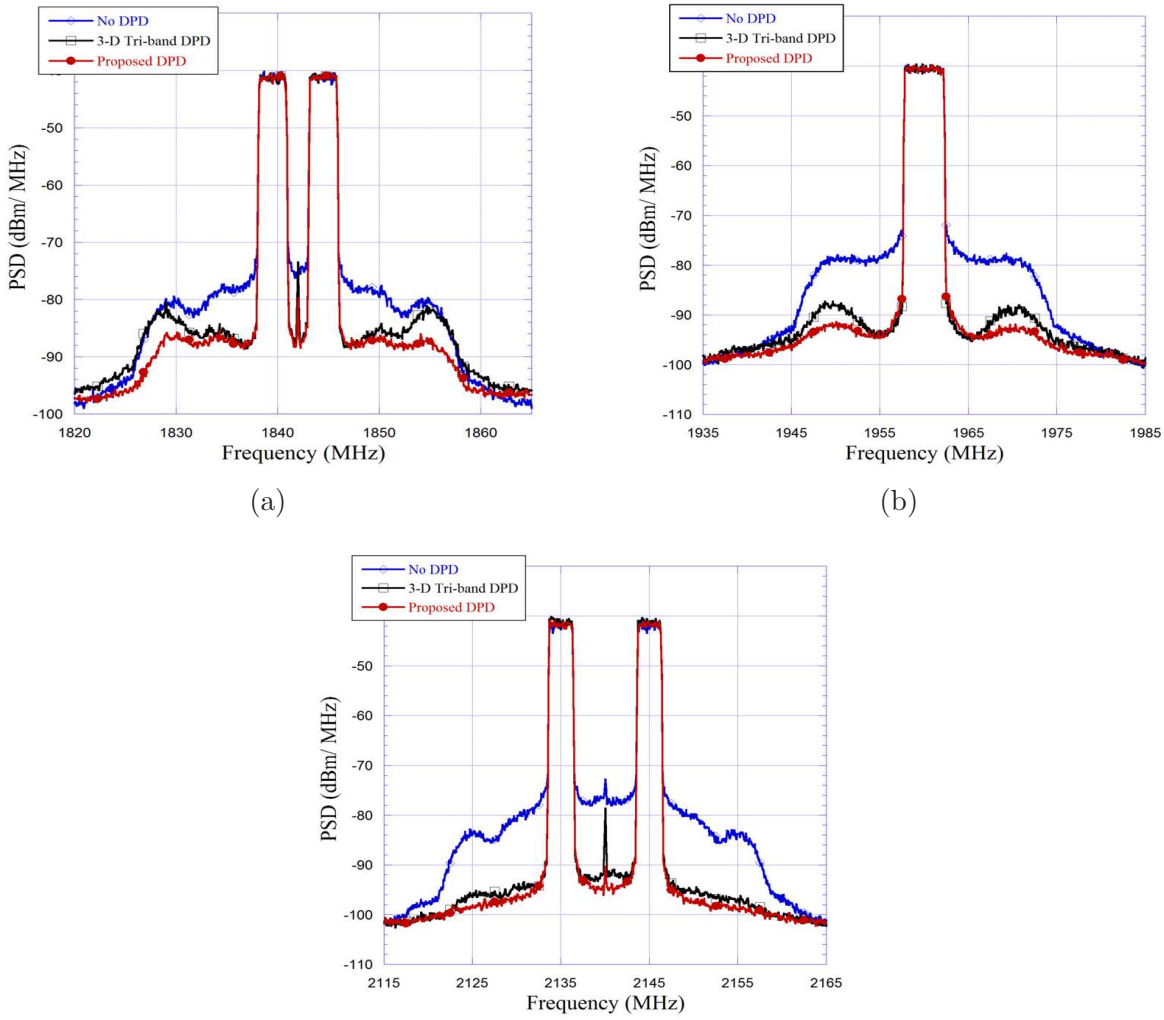

Figure 5.6: Output spectra with and without DPD. (a) Lower band. (b) Middle band. (c) Upper band.

the PA output around the three carrier frequencies (due to the hardware capabilities), the proposed DPD could further achieve around 10 dB suppression of the third-order ($\tilde{x}_2^2\tilde{x}_3^*$, $\tilde{x}_2^2\tilde{x}_1^*$, and $\tilde{x}_1\tilde{x}_2^*\tilde{x}_3$) and fifth-order IMD products ($\tilde{x}_1^2\tilde{x}_2^{*2}\tilde{x}_3$ and $\tilde{x}_1^{*2}\tilde{x}_2^3$) that lie in near regions to the carrier frequency bands, which satisfies the spectral emission mask of LTE signals of -45 dBc for the whole band. It also achieved around 3 to 4 dB IMD cancellation more than the 3-D tri-band DPD for the third-order and fifth-order IMD products as shown in Fig. 5.7.

DPD	lower band	middle band	upper band
	+/−5 MHz		
No-DPD	−34.48/−34.56	−35.25/−34.94	−37.81/−37.89
3-D tri-band DPD	−45.03/−45.17	−50.24/−50.65	−54.76/−55.11
Proposed DPD	−46.11/−45.91	−50.55/−50.59	−56.17/−56.82
	+/−10 MHz		
No-DPD	−35.61/−35.64	−34.64/−35.43	−39.56/ − 39.49
3-D tri-band DPD	−43.31/ − 43.20	−47.01/−47.11	−54.80/−55.37
Proposed DPD	−45.67/−45.54	−49.65/−49.88	−56.92/−57.01
	+/−15 MHz		
No-DPD	−39.55/−39.38	−38.45/−39.24	−43.71/−43.59
3-D tri-band DPD	−45.76/−45.84	−50.56/−50.11	−55.88/−56.34
Proposed DPD	−48.63/−48.41	−53.44/−53.72	−57.31/−57.62

Table 5.2: ACPR values in (dBc) for the Stated DPDs

Indeed, the proposed DPD that compensates for the phase and amplitude distortion effects around the carrier frequencies could result in better in-band linearization performance as well as out-of-band, since the interaction of the three predistorted signals would achieve better suppression of higher-order IMD products at the output of the tri-band PA without the need for higher ADC capabilities in order to capture these regions.

DPD	Model Dimensions	Number of coefficients
3-D tri-band DPD	$(M, N) = (3, 5)$	105
Proposed DPD	$(M_1, M_2, N) = (2, 3, 5)$	126

Table 5.3: Number of Coefficients

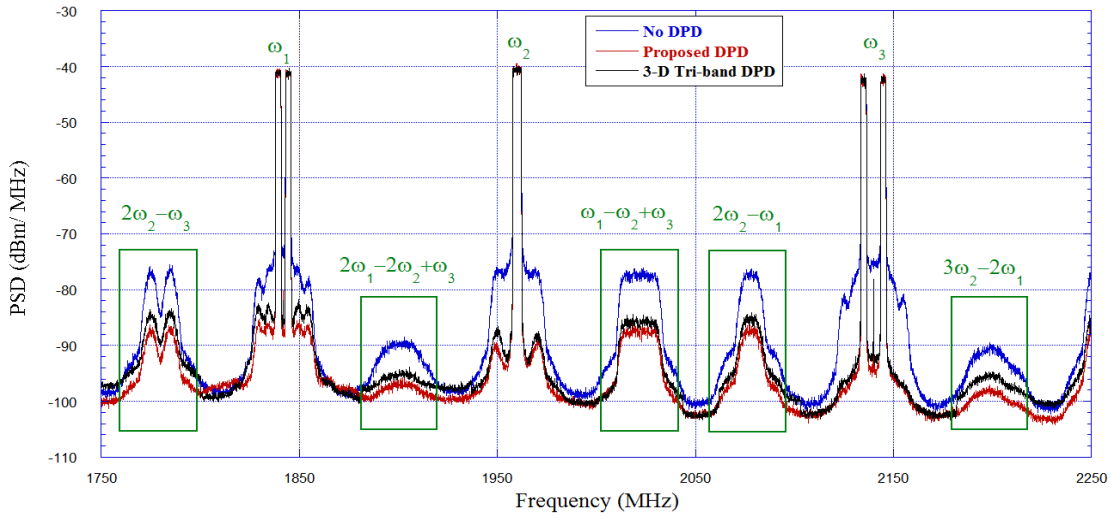

Figure 5.7: Spectra at the output of the tri-band PA for 500 MHz bandwidth with no DPD, 3-D tri-band DPD, and proposed DPD.

These results demonstrate that accounting for the phase distortion as well as the amplitude distortion of the three bands, enhances the linearization performance of the concurrent tri-band PA. Hence, the inclusion of the new cross terms that take into account the past information of the phase differences of the three different input signals has a major effect on the output of each band, and provides an accurate representation of the cross-modulation products between the three input signals. The results also show that neglecting the variation of the phase difference information over a wide frequency band affects the accuracy and linearization performance of the DPD.

5.6 Conclusions

This chapter presents a novel 3-D phase-aligned pruned Volterra model for the linearization of a concurrent tri-band transmitter. It was shown that combining three carrier aggregated LTE signals at three carrier frequencies suffers from severe inter-modulation and cross-modulation effects, due to the interaction of the three simultaneous input signals in a nonlinear envi-

ronment. The proposed DPD is based on the extension of a simplified Volterra model and extended in order to effectively compensate for the distortion induced by the tri-band PA, which requires the past information of the amplitude and phase variations of the different multi-input complex envelopes.

An experimental setup was used to validate the performance of the proposed 3-D phase aligned-pruned Volterra DPD that accounts for the phase distortion effects. The PA was driven by three different complex modulated multi-carrier LTE signals of different bandwidths at three carrier frequencies. In comparison with the basic 3-D tri-band model, the linearization results showed that the proposed DPD has significant in-band linearization improvement over the 3-D tri-band DPD. Since, the 3-D tri-band DPD ignores the instantaneous and past phase information impact of the combined input signals and only considers the past information of the compound amplitude of their complex envelopes. It also showed inter-band linearization improvement as it could further suppress the higher-order IMD products that lie in the near regions of the fundamental carrier frequencies.

Chapter 6

Complexity-Reduced techniques for multi-band PAs modeling and predistortion

6.1 Introduction

The multi-band DPDs discussed in the previous chapters are based on frequency-selective approaches. In such approaches, the PA nonlinear behavior around each frequency band is captured separately and processed using multi-input DPD cells [51, 52, 97, 98, 111] in order to alleviate the use of high bandwidth ADCs and DACs.

The main disadvantage of multi-band DPDs is the requirement of a high number of coefficients, in order to characterize the usual inter-modulation products and the added cross-modulation products that arise from the combined input signals and fall into the band of interest. Thus, these resulting multi-band DPDs have a high computational complexity that affects the real implementation of these DPDs. Therefore, different approaches for reducing the number of coefficients while achieving similar linearization results are reported. In [99], a 2-D modified MP model is proposed by modifying the envelope terms of the basic 2-D MP model in order to reduce the number of coefficients. In [112], a 2-D augmented Hammerstein model is proposed. In [114], the complexity of the 2-D MP DPD in [97] was simplified by eliminating certain terms to reduce computational complexity through a 1-D LUT, instead of a 2-D LUT.

In order to alleviate the numerical instability problems of the multi-band DPDs, [115] and

[116] proposed 2-D orthogonal models, where a closed-form orthogonal polynomial has been successfully introduced to replace the conventional polynomial in the 2-D MP DPD model. These orthogonal polynomial models are based on the orthogonal polynomials presented in [73] for single-band DPDs, and extended for the dual-band cases. In [117], an efficient hardware implementation inside the FPGA of the orthogonal polynomial 2-D DPD, which is based on the modified Legendre polynomials, is proposed.

In this chapter, a new basis function is defined for multi-band operation, which is based on a distributed polynomial system [118]. This distributed system is based on a radial pruning approach that separately estimates the dynamic nonlinearities of the multi-band transmitter and is validated in the case of a dual-band PA. Therefore, a 2-D multi-branch model is proposed for digital predistortion of concurrent dual-band transmitters. By employing this multi-branch distributed model, the overall complexity of the system, in terms of complex-valued parameters, has been reduced. The model also achieved an improved performance due to the accurate characterization of amplitude and phase variation effects of the dual-band PA.

The theory presented in this chapter will be demonstrated in the case of dual-band transmitters, for simplicity. However, it can be easily extended and validated for tri-band or higher-order band cases. The remainder of this chapter is organized as follows: Section 6.2 presents the modeling and characterization of the dual-band PA. The radial pruning approach of the general dual-band model is presented in Section 6.3. Section 6.4 demonstrates the model performance in the dual-band case, by using different bandwidth LTE and WCDMA signals. Finally, a conclusion of the chapter is presented in Section 6.5.

6.2 Dual-band MP Model

The concurrent dual-band transmitter has two input signal paths, where $\tilde{x}_1(n)$ and $\tilde{x}_2(n)$ are the two complex baseband input signals. Each signal is modulated to their respective RF band using two frequency up-conversion units. Subsequently, the two RF input signals are combined together to produce the wideband input signal, which drives the dual-band PA to give the outputs, $\tilde{y}_1(n)$ and $\tilde{y}_2(n)$, at the lower and upper frequency bands, ω_1 and ω_2, respectively.

The outputs of the dual-band PA are related to their corresponding inputs by nonlinear mapping functions as follows:

$$\tilde{y}_1(n) = f_{\mathrm{NL}}^{(1)}[\tilde{x}_1(n), \tilde{x}_2(n)]$$

$$\tilde{y}_2(n) = f_{\mathrm{NL}}^{(2)}[\tilde{x}_1(n), \tilde{x}_2(n)]$$

where the two nonlinear functions $f_{\mathrm{NL}}^{(1)}$ and $f_{\mathrm{NL}}^{(2)}$ are given by a 2-D MP function in [52] as follows:

$$\begin{aligned}\tilde{y}_1(n) = &\sum_{k=0}^{N}\sum_{j=0}^{k}\sum_{m=0}^{M} c_{k,j,m}^{(1)}\tilde{x}_1(n-m) \\ &\times |\tilde{x}_1(n-m)|^{k-j}|\tilde{x}_2(n-m)|^{j} \end{aligned} \tag{6.1}$$

$$\begin{aligned}\tilde{y}_2(n) = &\sum_{k=0}^{N}\sum_{j=0}^{k}\sum_{m=0}^{M} c_{k,j,m}^{(2)}\tilde{x}_2(n-m) \\ &\times |\tilde{x}_1(n-m)|^{k-j}|\tilde{x}_2(n-m)|^{j} \end{aligned} \tag{6.2}$$

where $\tilde{y}_1(n)$ and $\tilde{y}_2(n)$ are the estimated model outputs of the two-bands, respectively. $\tilde{x}_1(n)$ and $\tilde{x}_2(n)$ are the input signals at the lower and upper bands, respectively. $c_{k,j,m}^{(1)}$ and $c_{k,j,m}^{(2)}$ are the model coefficients of the lower and upper bands, respectively.

As shown in (6.1) and (6.2), the 2-D MP output is dependent only on the compound amplitude effect of the two input signals, and does not have phase information of the second input. Also, as the 2-D MP model is depending on the memory polynomial basis function, which has a fixed polynomial order for each branch that results in an over-sized model.

6.3 Proposed Model

The proposed model is based on extending the baseband single-band truncated Volterra model in [77, 119]. The general Volterra model is given by:

$$y(n) = \sum_{i=1}^{N} \sum_{\mathbf{l}_i=0}^{\mathbf{L}_i} h_i(\mathbf{l}_i) x(n-l_1) \prod_{q=1}^{i} x(n-l_q) x^*(n-l_{q+1}) \tag{6.3}$$

where $y(n)$ and $x(n)$ are the pass-band single-output and single-input signals, respectively. $h_i(\mathbf{l}_i)$ are the discrete-time Volterra kernels of order i and $\mathbf{l}_i$ is an i-dimensional vector composed of the delays, $l_q = 0, \cdots, L_i$ for all q. In order to truncate the model, the memory depth will have the same length $L_i = L$, for all nonlinearity order $i = 1, \cdots, N$.

This Volterra model is extended in order to include the multi-inputs in multi-band concurrent case. The resulting model is computationally heavy as it involve a huge number of coefficients, increasing extensively with the order and memory depth as shown in the previous chapter.

In the chapter, the dual-band case is studied. The Volterra model in (6.3) is further expanded to characterize the cross-modulation effects in dual-band case. The general Volterra kernels in this case can be represented by a grid forming a multi-dimensional hypercube and selection of the radial directions can be performed along the diagonals of this hypercube [119]. The different basis functions in the different radial-directions in case of third-order and fifth-

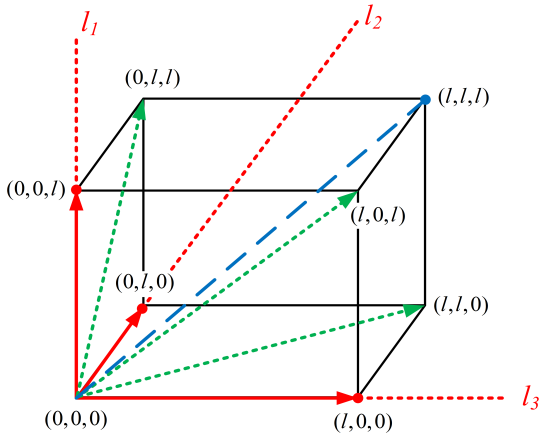

Figure 6.1: Three-dimensional pruning directions

order nonlinearity will be expressed as follows:

6.3.1 Third-order kernels

In order to show the radial pruning of pth-order Volterra kernels in case of dual-band transmitter, the idea for the third-order Volterra filters will be illustrated first. Fig. 6.1 demonstrates the different directions of the radial pruning technique for a 3rd-order Volterra filter. The basis functions resulting in this case are given as follows:

- Main-axis directions (1-D hypercube diagonals), represented by $(0,0,l)$, $(l,0,0)$, and $(0,l,0)$:

$$\varphi_{3,1,1}\left[\tilde{x}_1(n),\tilde{x}_2(n),l\right] = \tilde{x}_1(n-l)|\tilde{x}_1(n)||\tilde{x}_2(n)|,$$

$$\varphi_{3,1,2}\left[\tilde{x}_1(n),\tilde{x}_2(n),l\right] = \tilde{x}_1(n)\tilde{x}_2^*(n-l)\tilde{x}_2(n)$$

and

$$\varphi_{3,1,3}\left[\tilde{x}_1(n),\tilde{x}_2(n),l\right] = \tilde{x}_1^2(n)\tilde{x}_1^*(n-l).$$

- 2-D hypercube diagonal directions of the cube faces, represented by $(0,l,l)$, $(l,0,l)$, and

$(l, l, 0)$:

$$\varphi_{3,2,1}\left[\tilde{x}_1(n), \tilde{x}_2(n), l\right] = \tilde{x}_1(n)|\tilde{x}_1(n-l)||\tilde{x}_2(n-l)|,$$

$$\varphi_{3,2,2}\left[\tilde{x}_1(n), \tilde{x}_2(n), l\right] = \tilde{x}_1(n-l)\tilde{x}_2^*(n-l)\tilde{x}_2(n),$$

and

$$\varphi_{3,2,3}\left[\tilde{x}_1(n), \tilde{x}_2(n), l\right] = \tilde{x}_1^2(n-l)\tilde{x}_1^*(n).$$

• Main diagonal direction (3-D hypercube diagonals) , where $l_1 = l_2 = l_3$ and given by the corner (l, l, l): The different basis functions are

$$\varphi_{3,3,1}\left[\tilde{x}_1(n), \tilde{x}_2(n), l\right] = \tilde{x}_1(n-l)|\tilde{x}_1(n-l)||\tilde{x}_2(n-l)|.$$

The 2-D MP model [52] is only based on the main diagonal direction pruning, which limits the full capability of the model.

6.3.2 Higher-order kernels

Fig. 6.2 illustrates the 5th-order Volterra filter, represented by a 5-dimensional hypercube. Similarly, the higher-order volterra terms can be formulated with radial pruning directions. Therefore, the main basis functions for the pth-order Volterra kernals are given by:

• Main-axis directions (1-D hypercube diagonals):

$$\varphi_{(p,s),1,1}\left[\tilde{x}_1(n), \tilde{x}_2(n), l\right] = \tilde{x}_1(n)\tilde{x}_2^*(n-l)\tilde{x}_2(n)|\tilde{x}_1(n)|^s|\tilde{x}_2(n)|^{p-3-s},$$

$$\varphi_{(p,s),1,2}\left[\tilde{x}_1(n), \tilde{x}_2(n), l\right] = \tilde{x}_1(n-l)|\tilde{x}_1(n)|^s|\tilde{x}_2(n)|^{p-1-s},$$

and

$$\varphi_{(p,s),1,3}\left[\tilde{x}_1(n), \tilde{x}_2(n), l\right] = \tilde{x}_1^2(n)\tilde{x}_1^*(n-l)|\tilde{x}_1(n)|^s|\tilde{x}_2(n)|^{p-3-s}.$$

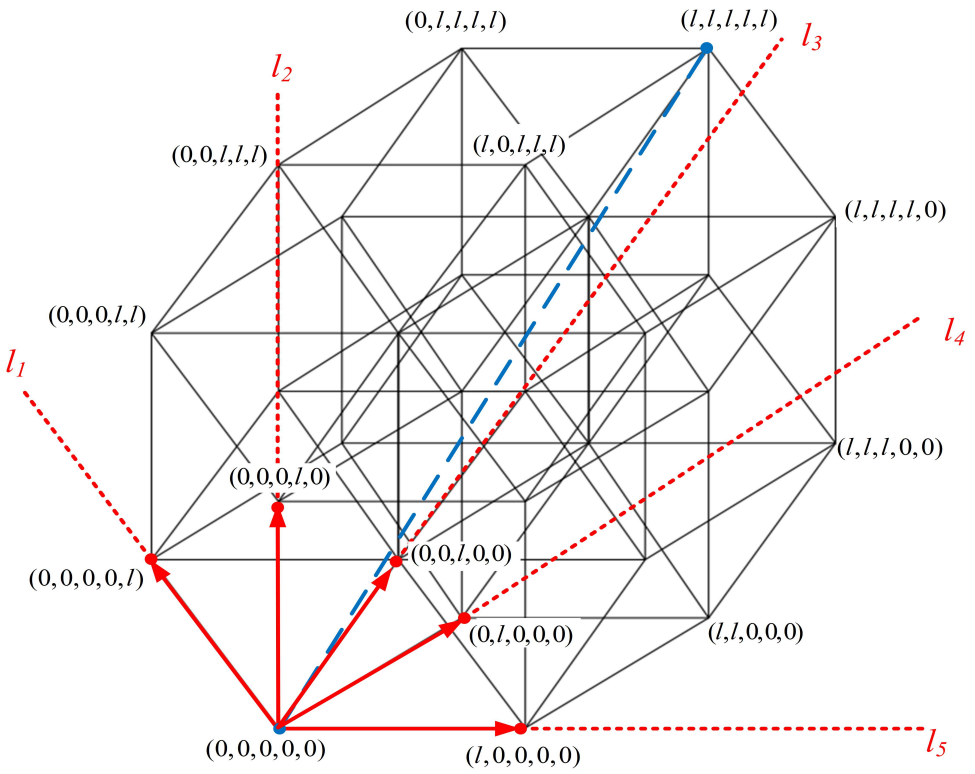

Figure 6.2: Five-dimensional pruning directions

• $(p-1)$-D Diagonal directions:

$$\varphi_{(p,s),p-1,1}\left[\tilde{x}_1(n),\tilde{x}_2(n),l\right]=\tilde{x}_1^2(n-l)\tilde{x}_1^*(n)|\tilde{x}_1(n-l)|^s|\tilde{x}_2(n-l)|^{p-3-s},$$

$$\varphi_{(p,s),p-1,2}\left[\tilde{x}_1(n),\tilde{x}_2(n),l\right]=\tilde{x}_1(n-l)\tilde{x}_2^*(n-l)\tilde{x}_2(n)|\tilde{x}_1(n-l)|^s|\tilde{x}_2(n-l)|^{p-3-s},$$

and

$$\varphi_{(p,s),p-1,3}\left[\tilde{x}_i(n),\tilde{x}_j(n),l\right]=\tilde{x}_1(n)|\tilde{x}_1(n-l)|^s|\tilde{x}_2(n-l)|^{p-1-s}.$$

• Main diagonal direction (p-D hypercube diagonals):

$$\varphi_{(p,s),p,1}\left[\tilde{x}_1(n),\tilde{x}_2(n),l\right]=\tilde{x}_1(n-l)|\tilde{x}_2(n-l)|^s|\tilde{x}_2(n-l)|^{p-1-s}$$

Similarly, the diagonal directions of the different order-hypercubes can be formulated. As shown, the proposed model is based on multi-branches, where the dynamic nonlinearities

of the PA is separately identified with different polynomial orders using a radial pruning approach [119]. Also, the model is extended to include the 2-D diagonal directions that include the phase variation effects of the two inputs. Note that the 2-D MP DPD [52] is only based upon the pruning of the general model in the main diagonal direction of the p-D hypercube.

The resultant model is given as follows:

$$\tilde{y}_i(n) = \sum_{p=1}^{N} \sum_{s=0}^{p} \sum_{r=1}^{p} \sum_{k=1}^{K_r} \sum_{l=0}^{L} h_{p,s,r,k}^{(i)}(l) \varphi_{(p,s),r,k} \left[\tilde{x}_i(n), \tilde{x}_j(n), l \right] \tag{6.4}$$

where $\tilde{y}_i(n)$ is the complex envelope of the estimated dual-band PA output signal centered around the fundamental frequency ω_i. L is the memory depth of the Volterra filters; N are the nonlinear orders of the multi-branches; K_r is the number of radial directions for each direction r; $h_{p,s,r,k}^{(i)}(l)$ are the model coefficients; where $i, j \in \{1, 2\}$, and $i \neq j$.

Note that the proposed model has added cross terms in the form of $\tilde{x}_i^2(n)\tilde{x}_i^*(n-m)$ and $\tilde{x}_i(n)\tilde{x}_j^*(n-m)\tilde{x}_j(n)$ rather than the 2-D MP DPD model, which is only based on the main diagonal truncation. These terms have both amplitude and phase information of the input signals and their impact on the output which enhances the model accuracy.

The model could be further reduced by selecting the most dominant basis functions and using a different polynomial order and memory depth for the dynamics of the model. This will give more flexibility in the characterization of the PA, and will reduce the overall computational complexity of the model.

The simplified model is given as follows:

$$\begin{aligned}\tilde{y}_i(n) = &\sum_{p=0}^{N_1-1}\sum_{s=0}^{p}\sum_{m=0}^{M_1} h_{p,s,1}^{(i)}(m)\tilde{x}_i(n) \times |\tilde{x}_i(n-m)|^{p-s}|\tilde{x}_j(n-m)|^s \\ &+ \sum_{p=0}^{N_2-1}\sum_{s=0}^{p}\sum_{m=1}^{M_2} h_{p,s,2}^{(i)}(m)\tilde{x}_i(n-m) \times |\tilde{x}_i(n-m)|^{p-s}|\tilde{x}_j(n-m)|^s \\ &+ \sum_{p=0}^{N_3-1}\sum_{s=0}^{p}\sum_{m=1}^{M_3} h_{p,s,3}^{(i)}(m)\tilde{x}_i^2(n)\tilde{x}_i^*(n-m) \times |\tilde{x}_i(n)|^{p-s}|\tilde{x}_j(n)|^s \\ &+ \sum_{p=0}^{N_4-1}\sum_{s=0}^{p}\sum_{m=1}^{M_4} h_{p,s,4}^{(i)}(m)\tilde{x}_i(n)\tilde{x}_j^*(n-m)\tilde{x}_j(n) \times |\tilde{x}_i(n)|^{p-s}|\tilde{x}_j(n)|^s \\ &+ \sum_{p=0}^{N_5-1}\sum_{s=0}^{p}\sum_{m=1}^{M_5} h_{p,s,5}^{(i)}(m)\tilde{x}_i(n-m)\tilde{x}_j^*(n)\tilde{x}_j(n-m) \times |\tilde{x}_i(n-m)|^{p-s}|\tilde{x}_j(n-m)|^s \quad (6.5)\end{aligned}$$

The model output is linear in terms of its coefficients. Therefore, linear least squares algorithms can be used for model identification. In this paper, least square (LS) algorithm is used for model identification.

6.3.3 Measurement Setup

The measurement setup for the characterization and digital predistortion of a dual-band PA operated in concurrent mode was previously described in Chapter 3. The transmitter chain contains 10 W GaN based wideband PA biased at class AB at Vds of 28 V and Vgs of -3.1 V. The PA is operated concurrently at 2,350 and 2,500 MHz carrier frequencies.

The dual-band input signals are modulated and up-converted to required carrier frequencies using vector signal generators VSG1 (E4438C) and VSG2 (E4438C), respectively. Both generators were time synchronized at baseband. The RF signals were combined using a power combiner and used to drive the PA. The PA output at each band is individually down-converted and digitized using vector spectrum analyzer VSA (E4440A). Data is captured at each band with a sampling frequency (f_s= 92.16 MHz).

	lower band @ 2.35 GHz	upper band @ 2.5 GHz
Scenario I	LTE Bandwidth= 5 MHz	LTE Bandwidth= 5 MHz
Scenario II	WCDMA(1111) Bandwidth= 20 MHz	WCDMA(1001) Bandwidth= 20 MHz
Scenario III	WCDMA Bandwidth= 5 MHz	LTE Bandwidth= 15 MHz

Table 6.1: Summary of the three scenarios

The baseband output signal at each band is individually time aligned with the respective input baseband signal. Time-aligned and normalized input-output data is swapped to extract inverse relation using the proposed model and the 2-D MP model in MATLAB. The predistorted signals are then re-applied to the dual-band PA in order to obtain the linearized signals. Three different signal scenarios of different bandwidths were considered and summarized in Table 6.1.

6.4 Performance Assessment

6.4.1 Measurement Results

The results for the proposed DPD and the 2-D MP DPD [52] are evaluated for the three scenarios indicated in the previous section.

Fig. 6.3 shows the PSD of the signals at the output of the PA for the three scenarios, with no linearization and with using the two DPDs. Table 6.2 shows the inverse NMSE measured for the two DPDs in the three scenarios and the number of coefficients used.

	DPD	No. of Coefficients	NMSE (dB)	
			lower band	upper band
Scenario I	2-D MP DPD	75	−42.12	−41.09
	Proposed DPD	56	−42.71	−44.75
Scenario II	2-D MP DPD	105	−38.81	−35.51
	Proposed DPD	87	−40.15	−38.63
Scenario III	2-D MP DPD	84	−39.61	−43.05
	Proposed DPD	69	−40.82	−43.23

Table 6.2: Inverse NMSE values in (dB) for the Stated DPDs

The model dimensions of the two DPDs are determined using a general sweep method. This general sweep method consists of simultaneously sweeping the model dimensions (nonlinearity order and memory depth) over a wide-enough range for each scenario. The accuracy of each model is quantified using the NMSE metric. Finally, the model dimensions corresponding to the combination resulting in the lowest number of coefficients that achieves low NMSE are selected. As shown in Table 6.2, In comparison with the 2-D MP model, the proposed model has reduced number of coefficients and also improved the NMSE in the three scenarios as also shown in the PSD figures shown in Fig. 6.3. These measurement results illustrate the improved performance achieved by the proposed model as well as the reduction of the number of model parameters as shown in the previous section.

6.5 Conclusion

In this chapter, a 2-D multi-branch model is proposed for the characterization and digital predistortion of the in-band and cross-band distortion of dual-band RF transmitters. The

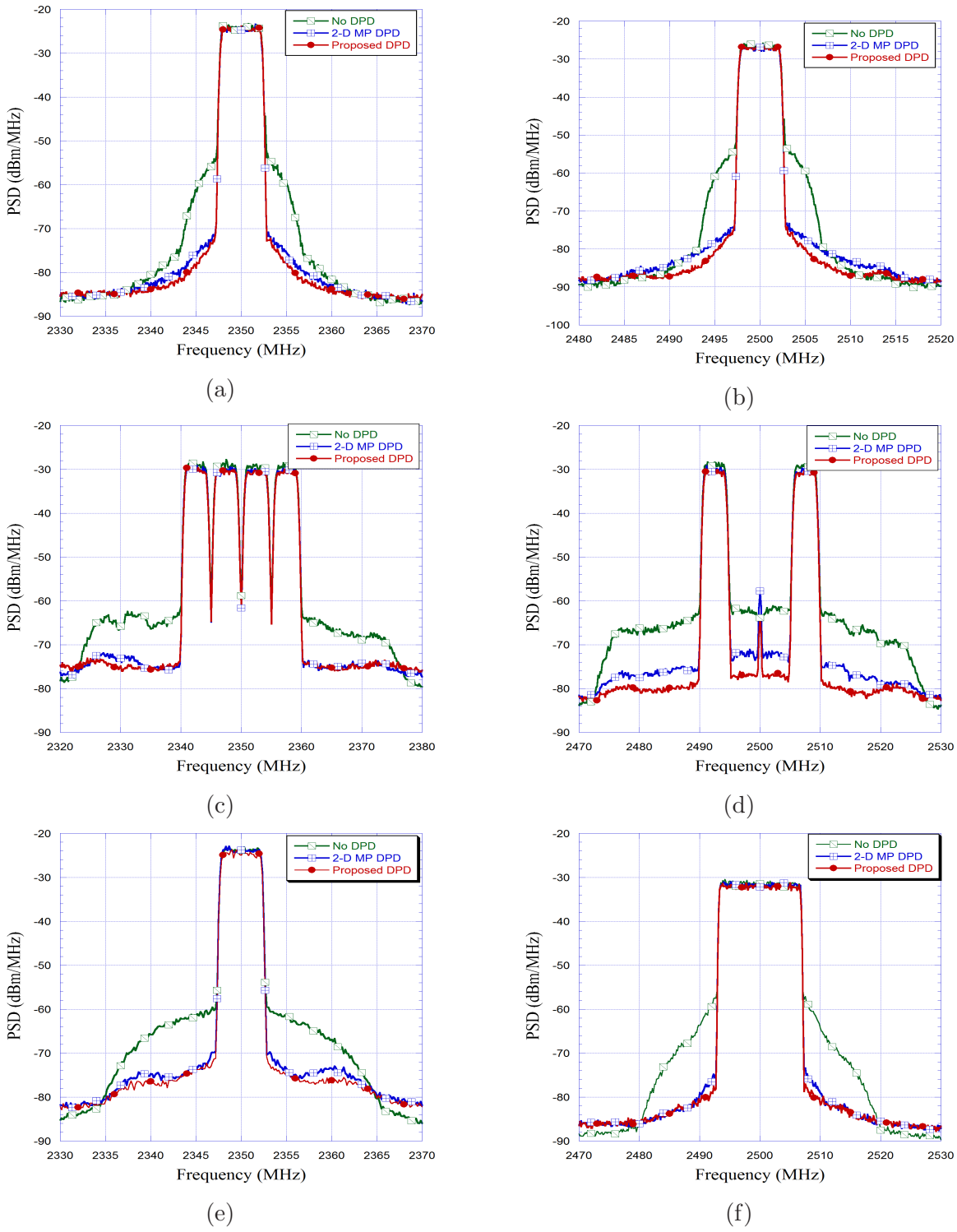

Figure 6.3: Measured PSDs with and without DPD (a) Scenario I, the lower-band LTE (5 MHz). (b) Scenario I, the upper-band LTE (5 MHz). (c) Scenario II, the lower-band WCDMA 1111 (20 MHz). (d) Scenario II, the upper-band WCDMA 1001 (20MHz). (e) Scenario III, the lower-band WCMDA (5 MHz). (f) Scenario III, the upper-band LTE (15 MHz).

proposed model is based on separately identifying the dynamic behavior of the PA and also adding memory cross terms in order to characterize the amplitude and phase distortion effects of the two inputs.

The proposed technique was experimentally assessed by exciting a dual-band Class AB PA with three different scenarios, of different standard signals with different bandwidths. Indeed, the proposed model showed accurate performance and reduced computational complexity, as compared to the state-of-the-art 2-D MP DPD.

Chapter 7

Conclusions and Future Work

In this chapter, the conclusions of this dissertation are presented in Section 7.1. Then, the future work is discussed in Section 7.2.

7.1 Conclusions

Multi-band transmitters are suitable candidates and very promising architectures for modern wireless communication systems, such as CA LTE-advanced systems. CA LTE is an efficient way to increase the signal bandwidth within the available spectrum. Therefore, multi-band transmitter architectures should operate in both concurrent and single modes of operation in order to support the intra-band and inter-band CAs in LTE-advanced.

In this dissertation, different RF impairments, such as PA nonlinearity, I/Q modulator imperfections, and phase variation effects, are investigated and compensated for in multi-band wireless communication systems. Closed-form expressions of the nonlinear distortion of the dual-band and tri-band transmitters were derived. Thus, a comprehensive analysis of the distortion output of various RF impairments and their effects on direct conversion and low-IF multi-band transmitters is presented. Specifically, the contributions of the dissertation are concluded as follows:

In Chapter 2, the topics of behavioral modeling and digital predistortion of RF single-band PAs are investigated. Behavioral modeling is an efficient tool in modeling and analyzing the PAs behavior and the design of linearization techniques [40]. In this kind of system level

modeling, the PA is considered as a "black box", where the model provides a computationally efficient means of relating the PA's input and output signals without knowing any apriori knowledge of the physical analysis of the system. In Chapter 2, different behavioral models were discussed and their performance was assessed.

A novel Feedforward Hammerstein model/DPD is proposed for the accurate characterization of the dynamic nonlinear behavior of the PAs [68]. The proposed model is composed of two coupled loops, a signal cancellation loop and a distortion injection. The structure of this model is similar to the Feedforward linearization technique, where the signal cancellation loop is responsible for characterizing the PA's dynamics through a Hammerstein model. The distortion injection loop models the residual distorted signal. This inter-modulation distorted signal is modeled via a combination of parallel nonlinear FIR filters to better mimick of the inter-modulation distortion products in the out-band regions. The model performance was assessed, and outperformed the state-of-the-art models, especially in the regions of the inter-modulation products. Indeed, the distortion injection loop was found to complement the main signal cancellation loop by adding an adequate mechanism to model the nonlinear dynamics of the inter-modulation distorted signal.

In Chapter 3, a joint DPD is proposed for compensation of I/Q imbalance and PA nonlinearity in single-band transmitters. Indeed, the performance of different DPD linearizers is affected by the imperfections of the up-converters in the transmission path and down-converters in the feedback path. These imperfections are caused by the non-idealities of the analog IQ modulators. The imperfections include gain imbalance, imperfect quadrature, and LO leakage, which will result in MFI and degraded EVM. Recent DPDs are mainly concerned with PA distortion, while the I/Q modulator imperfections are mitigated sepa-

rately in a two step process [54]. Therefore, the proposed structure is a complexity-reduced compound DPD for the joint mitigation of linear and nonlinear distortion of the transmitter [96]. The proposed DPD is able to adapt to the changes of the input data in the presence of modulator I/Q imbalances. The proposed linearization technique is validated in the cases of zero-IF and low-IF transmitters.

In Chapter 4, the nonlinear distortion in the case of dual-band transmitters is analyzed. The output distortion in this case arises from the cross-modulation and inter-modulation products that result from the interaction of multiple channels in a nonlinear environment, concurrently. These products manifest themselves as extra in-band and out-of-band distortion, rather than the distortion output in single-band cases. The proposed DPD in Chapter 3 is extended and a dual-input truncated Volterra model is proposed for the joint mitigation of dual-band PA inter-modulation and cross-modulation distortion in the presence of modulator imperfections and DC offset [106]. The proposed model showed enhanced performance and lower computational complexity than the state-of-the-art models. Therefore, the implementation of the proposed model in DSP/ FPGA platform is more practical as well as more economical in utilizing the FPGA resources.

In Chapter 5, theoretical analysis of the nonlinear distortion in the concurrent tri-band transmitters was given. It was shown that the cross-band modulation in the concurrent tri-band PA has a more complex form than that in the concurrent dual-band PA. Subsequently, a 3-D MP DPD is presented for the linearization of tri-band PA [108] for the first time. The proposed DPD was validated in a multi-band/multi-standard scenario by driving the PA, with three single-carrier 5 MHz LTE, WCDMA, and WiMAX signals applied in the three bands, concurrently.

The analysis is further extended in order to include the effects of the phase distortion in the tri-band transmitter. The phase response of RF filters is an important parameter for the transmission of signals through the filter. Unless the signal is just a sine-wave, the filter phase response will always create signal distortion. The phase relationships of the signal frequency components are affected by the filter's phase response. Indeed, using wider bandwidth signals will cause difference in group delay. The difference in group delay, for signals spread out over a filter's pass-band, is a measure of the phase distortion introduced by the filter. Thus, the transmitter phase distortion affects the transmission quality and needs to be compensated for. Therefore, for the first time in multi-band DPDs, a novel 3-D phase-aligned DPD is proposed that takes into account both the compound amplitude and phase variation effects in a concurrent tri-band transmitter [111].

The general basis function for the 2-D MP model has high complexity that requires a high number of coefficients. It only includes the diagonal terms of the general Volterra model in dual-band case, which also limits the model's performance. In Chapter 6, the basis function of the multi-dimensional model is extended to include higher-order cross terms of the general pass-band Volterra model including the amplitude and phase variation effects. However, this will increase the computational complexity even more. Therefore, the proposed pruned model is based on a distributed polynomial basis function with a radial pruning approach that separately characterize the dynamic nonlinearity of the cross-modulation products [118]. Indeed, the proposed multi-branch model accomplishes a significant reduction in the number of coefficients, with improved accuracy due to the added distortion terms. The proposed DPD is validated for a dual-band case by exciting a dual-band Class AB PA with different scenarios of different standards and bandwidth multi-carrier signals.

7.2 Future work

A potential future work of this research is to implement the proposed multi-dimensional models in a DSP/FPGA platform to test their accuracy and the numerical stability of their identification procedure. Another issue that must be addressed is the adaptability of the DPDs in order to compensate for the varying conditions, such as temperature and long term memory effects of base station PAs in the case of concurrent operation. For the future work, direct learning architecture can be studied and used for the identification of the multi-cell DPD functions. The direct learning architecture is more complex than the indirect architecture as it requires explicit knowledge of the DUT model, where adaptive algorithms are used to identify the coefficients of the predistorter that are updated directly from the DPD input. Thus, they can adapt faster to the varying conditions of the multi-band PAs. The impact of using the direct learning architecture on both the DPD performance and its added computational complexity would be worth studying for future research.

Another important factor that should be studied in multi-band PAs is the efficiency of transmission. Therefore, different efficiency enhancement transmitter architectures suitable for multi-band operation should be considered for future research. An example of such architectures, is an envelope tracking multi-band transmitter. In this case, the power supply voltage should be dynamically adapted according to the input signal envelope, such that the PA will always approach to the saturation and result in high efficiency. In case of multi-band, the dynamic supply should be adapted according to the multi-input signals waveform shaping techniques in order to ensure a trade-off between high-efficiency and high-linearity at the different frequency bands. Primary results of the envelope tracking multi-band transmitter is

presented in [120]. However, the generalization of the different multi-band DPDs presented in this dissertation is required in order to compensate for the added distortion in case of envelope tracking transmitters. The added distortion is due to the dynamic supply voltage that create $V_{DD} - AM$ and $V_{DD} - PM$ effects that should be compensated for by the multi-band DPD.

Appendix A

Derivation of the dual-band general static model

The passband output $y(t)$ is related to the bandpass inputs $x_1(t)$ and $x_2(t)$ by:

$$y(t) = \sum_{k=1}^{N} a_k(\alpha_1 x_1(t) + \alpha_2 x_2(t))^k \tag{A.1}$$

Therefore, $y(t)$ can be expressed as:

$$y(t) = \sum_{k=1}^{N} \sum_{r_1=0}^{k} C_{r_1}^k a_{kr_1} (x_1(t))^{k-r_1} (x_2(t))^{r_1} \tag{A.2}$$

where the set of coefficients a_{kr_1} is equal to $a_{kr_1} = a_k(\alpha_1)^{k-r_1}(\alpha_2)^{r_1}$ and $C_a^b = \dfrac{b!}{(b-a)!a!}$.

The complex representation of the passband signal $x(t)$ in terms of its complex envelope $\tilde{x}(t)$ is:

$$x(t) = \frac{\tilde{x}(t)e^{j\omega t} + \tilde{x}^*(t)e^{-j\omega t}}{2} \tag{A.3}$$

where the complex envelope $\tilde{x}(t)$ can be represented as $\tilde{x}(t) = X(t)e^{j\theta(t)}$, where $X(t)$ and $\theta(t)$ are the instantaneous amplitude and phase of $\tilde{x}(t)$, respectively.

For convenience, the notation (t) is dropped hereafter. Replacing the passband signals x_1 and x_2 in (A.2) with their complex representations results in:

$$y(t) = \sum_{k=1}^{N} \sum_{r_1=0}^{k} \frac{1}{2^k} C_{r_1}^k a_{kr_1} (\tilde{x}_1(t)e^{j\omega_1 t} + \tilde{x}_1^*(t)e^{-j\omega_1 t})^{k-r_1} (\tilde{x}_2(t)e^{j\omega_2 t} + \tilde{x}_2^*(t)e^{-j\omega_2 t})^{r_1}. \tag{A.4}$$

By applying the binomial theorem, the above relation ends up to as:

$$y(t) = \sum_{k=1}^{N} \sum_{r_1=0}^{k} \frac{1}{2^k} C_{r_1}^k a_{kr_1} \sum_{k_1=0}^{k-r_1} \sum_{k_2=0}^{r_1} C_{k_1}^{k-r_1} C_{k_2}^{r_1} (\tilde{x}_1)^{k-r_1-k_1} (\tilde{x}_1^*)^{k_1} (\tilde{x}_2)^{r_1-k_2} (\tilde{x}_2^*)^{k_2}$$
$$\times e^{j\omega_1(k-r_1-2k_1)t} e^{j\omega_2(r_1-2k_2)t} \tag{A.5}$$

Therefore, the general basis function series ϕ_{kr} for the dual-band model is given by:

$$\phi_{kr}(\tilde{x}_1, \tilde{x}_2) = (\tilde{x}_1)^{k-r_1-k_1}(\tilde{x}_1^*)^{k_1}(\tilde{x}_2)^{r_1-k_2}(\tilde{x}_2^*)^{k_2}e^{j\omega_1(k-r_1-2k_1)t}e^{j\omega_2(r_1-2k_2)t} \tag{A.6}$$

For the terms around ω_1:

$$\begin{cases} k - r_1 - 2k_1 & = 1 \\ r_1 - 2k_2 & = 0 \end{cases}$$

The basis function for the terms around ω_1 is then given as:

$$[\phi_{kr}(\tilde{x}_1, \tilde{x}_2)]_{\omega_1} = (\tilde{x}_1)^{1+k_1}(\tilde{x}_1^*)^{k_1}(\tilde{x}_2)^{k_2}(\tilde{x}_2^*)^{k_2}e^{j\omega_1 t} = \tilde{x}_1|\tilde{x}_1|^{2k_1}|\tilde{x}_2|^{2k_2}e^{j\omega_1 t} \tag{A.7}$$

Similarly, the terms grouped around the different frequencies are calculated, and the general equation for the dual-band PA can be given by:

$$\begin{aligned} y = \sum_{k=1}^{N}\sum_{r_1=0}^{k}\sum_{k_1=0}^{k-r_1}\sum_{k_2=0}^{r_1}\frac{1}{2^k}a_{kr_1}C_{r_1}^{k}C_{k_1}^{k-r_1}C_{k_2}^{r_1} \\ \times \Big[(\tilde{x}_1|\tilde{x}_1|^{2k_1}|\tilde{x}_2|^{2k_2})e^{j\omega_1 t} \\ + (\tilde{x}_2|\tilde{x}_1|^{2k_1}|\tilde{x}_2|^{2k_2})e^{j\omega_2 t} \\ + (\tilde{x}_1^*\tilde{x}_2^2|\tilde{x}_1|^{2(k_1-1)}|\tilde{x}_2|^{2k_2})e^{j(2\omega_2-\omega_1)t} \\ + (\tilde{x}_1^2\tilde{x}_2^*|\tilde{x}_1|^{2k_1}|\tilde{x}_2|^{2(k_2-1)})e^{j(2\omega_1-\omega_2)t} \\ + (\tilde{x}_1^3\tilde{x}_2^{*2}|\tilde{x}_1|^{2k_1}|\tilde{x}_2|^{2(k_2-2)})e^{j(2\omega_1-\omega_2)t} + \cdots\Big] \end{aligned} \tag{A.8}$$

y can also be expressed in terms of its complex envelope components around ω_1 and ω_2, similar to (A.3):

$$y = \frac{\tilde{y}_1 e^{j\omega_1 t} + \tilde{y}_1^*(t)e^{-j\omega_1 t}}{2} + \frac{\tilde{y}_2 e^{j\omega_2 t} + \tilde{y}_2^*(t)e^{-j\omega_2 t}}{2} + \cdots \tag{A.9}$$

By equating the coefficients in (A.8) and (A.9) around ω_1, the complex envelope $\tilde{y}_1$ of the

output signal around ω_1 can be given as:

$$\tilde{y}_1 = \sum_{k=1}^{N} \sum_{r_1=0}^{k} \sum_{k_1=0}^{k-r_1} \sum_{k_2=0}^{r_1} \frac{1}{2^{k-1}} a_{kr_1}^{(1)} C_{r_1}^{k} C_{k_1}^{k-r_1} C_{k_2}^{r_1} \times \tilde{x}_1 |\tilde{x}_1|^{2k_1} |\tilde{x}_2|^{2k_2} \tag{A.10}$$

Similarly, the complex envelope $\tilde{y}_2$ of the output signal around ω_2 can be given as:

$$\tilde{y}_2 = \sum_{k=1}^{N} \sum_{r_1=0}^{k} \sum_{k_1=0}^{k-r_1} \sum_{k_2=0}^{r_1} \frac{1}{2^{k-1}} a_{kr_1}^{(2)} C_{r_1}^{k} C_{k_1}^{k-r_1} C_{k_2}^{r_1} \times \tilde{x}_2 |\tilde{x}_1|^{2k_1} |\tilde{x}_2|^{2k_2} \tag{A.11}$$

where the set of coefficients for each band can be grouped in one term as follows:

$$\begin{aligned} A_{kr_1}^{(1)} &= \frac{1}{2^{k-1}} a_{kr_1}^{(1)} C_{r_1}^{k} C_{k_1}^{k-r_1} C_{k_2}^{r_1} \\ A_{kr_1}^{(2)} &= \frac{1}{2^{k-1}} a_{kr_1}^{(2)} C_{r_1}^{k} C_{k_1}^{k-r_1} C_{k_2}^{r_1} \end{aligned} \tag{A.12}$$

where $A_{kr_1}^{(1)}$ and $A_{kr_1}^{(2)}$ are the model baseband coefficients for the lower and upper bands, respectively.

Appendix B

Derivation of the tri-band dynamic function

The derivation for $\tilde{y}_{\mathrm{s},q}(n)$ is given as follows; where the dynamic bandpass model is given by (5.11):

$$\begin{aligned} y_{\mathrm{d}}(n) = & \sum_{p=0}^{P} \sum_{i_1=0}^{M_1-1} \sum_{i_2=i_1+1}^{M_2-1} H_p(i_1, i_2) \\ & \times [x_1(n-i_1) + x_2(n-i_1) + x_3(n-i_1)]^p \\ & \times [x_1(n-i_2) + x_2(n-i_2) + x_3(n-i_2)] \end{aligned}$$

By using the binomial theorem $y_{\mathrm{d}}(n)$ can be expressed as:

$$\begin{aligned} y_{\mathrm{d}}(n) = & \sum_{i_1=0}^{M_1-1} \sum_{i_2=i_1+1}^{M_2-1} \sum_{p=0}^{P} \sum_{r_1=0}^{p} \sum_{r_2=0}^{r_1} \binom{p}{r_1} \binom{r_1}{r_2} \\ & \times \Big[H_{p,r_1,r_2,1}(i_1, i_2) x_1^{p-r_1}(n-i_1) x_2^{r_2}(n-i_1) \\ & \qquad \times x_3^{r_1-r_2}(n-i_1) x_1(n-i_2) \\ & + H_{p,r_1,r_2,2}(i_1, i_2) x_1^{p-r_1}(n-i_1) x_2^{r_2}(n-i_1) \\ & \qquad \times x_3^{r_1-r_2}(n-i_1) x_2(n-i_2) \\ & + H_{p,r_1,r_2,3}(i_1, i_2) x_1^{p-r_1}(n-i_1) x_2^{r_2}(n-i_1) \\ & \qquad \times x_3^{r_1-r_2}(n-i_1) x_3(n-i_2) \Big]. \end{aligned} \tag{B.1}$$

The complex representation of the bandpass signal $x(n)$ in terms of its complex envelope $\tilde{x}(n)$ is:

$$x(n) = \frac{\tilde{x}(n) e^{j\omega n T_{\mathrm{s}}} + \tilde{x}^*(n) e^{-j\omega n T_{\mathrm{s}}}}{2}. \tag{B.2}$$

Then by replacing $x(n)$ with its expression in (B.2), (B.1) can be rewritten as:

$$
\begin{aligned}
y_{\mathrm{d}}(n) = & \sum_{i_1=0}^{M_1-1} \sum_{i_2=i_1+1}^{M_2-1} \sum_{p=0}^{P} \sum_{r_1=0}^{p} \sum_{r_2=0}^{r_1} \frac{1}{2^{p+1}} \binom{p}{r_1} \binom{r_1}{r_2} \\
& \times \sum_{k_2=0}^{p-r_1} \sum_{k_3=0}^{r_2} \sum_{k_4=0}^{r_1-r_2} \sum_{k_5=1}^{1} \binom{p-r_1}{k_2} \binom{r_2}{k_3} \binom{r_1-r_2}{k_4} \binom{1}{k_5} \\
& \times \Big\{ h_{p,r_1,r_2,1}(i_1,i_2) \phi^{(1)} \left[\tilde{x}_1(n), \tilde{x}_2(n), \tilde{x}_3(n)\right] \\
& + h_{p,r_1,r_2,2}(i_1,i_2) \phi^{(2)} \left[\tilde{x}_1(n), \tilde{x}_2(n), \tilde{x}_3(n)\right] \\
& + h_{p,r_1,r_2,3}(i_1,i_2) \phi^{(3)} \left[\tilde{x}_1(n), \tilde{x}_2(n), \tilde{x}_3(n)\right] \Big\}. \qquad \text{(B.3)}
\end{aligned}
$$

Therefore, the three basis functions can be expressed as follows:

$$
\begin{aligned}
& \phi^{(1)} \left[\tilde{x}_1(n), \tilde{x}_2(n), \tilde{x}_3(n)\right] = \\
& \left[\tilde{x}_1(n-i_2)\right]^{1-k_5} \left[\tilde{x}_1^*(n-i_2)\right]^{k_5} e^{j\omega_1(1-2k_5)(n-i_2)T_s} \\
& \times \left[\tilde{x}_1(n-i_1)\right]^{p-r_1-k_2} \left[\tilde{x}_1^*(n-i_1)\right]^{k_2} e^{j\omega_1(p-r_1-2k_2)(n-i_1)T_s} \\
& \times \left[\tilde{x}_2(n-i_1)\right]^{r_2-k_3} \left[\tilde{x}_2^*(n-i_1)\right]^{k_3} e^{j\omega_2(r_2-2k_3)(n-i_1)T_s} \\
& \times \left[\tilde{x}_3(n-i_1)\right]^{r_1-r_2-k_4} \left[\tilde{x}_3^*(n-i_1)\right]^{k_4} e^{j\omega_3(r_1-r_2-2k_4)(n-i_1)T_s} \qquad \text{(B.4)}
\end{aligned}
$$

$$
\begin{aligned}
& \phi^{(2)} \left[\tilde{x}_1(n), \tilde{x}_2(n), \tilde{x}_3(n)\right] = \\
& \left[\tilde{x}_2(n-i_2)\right]^{1-k_5} \left[\tilde{x}_2^*(n-i_2)\right]^{k_5} e^{j\omega_2(1-2k_5)(n-i_2)T_s} \\
& \times \left[\tilde{x}_1(n-i_1)\right]^{p-r_1-k_2} \left[\tilde{x}_1^*(n-i_1)\right]^{k_2} e^{j\omega_1(p-r_1-2k_2)(n-i_1)T_s} \\
& \times \left[\tilde{x}_2(n-i_1)\right]^{r_2-k_3} \left[\tilde{x}_2^*(n-i_1)\right]^{k_3} e^{j\omega_2(r_2-2k_3)(n-i_1)T_s} \\
& \times \left[\tilde{x}_3(n-i_1)\right]^{r_1-r_2-k_4} \left[\tilde{x}_3^*(n-i_1)\right]^{k_4} e^{j\omega_3(r_1-r_2-2k_4)(n-i_1)T_s} \qquad \text{(B.5)}
\end{aligned}
$$

$$\phi^{(3)}\left[\tilde{x}_1(n), \tilde{x}_2(n), \tilde{x}_3(n)\right] =$$

$$[\tilde{x}_3(n-i_2)]^{1-k_5}[\tilde{x}_3^*(n-i_2)]^{k_5} e^{j\omega_3(1-2k_5)(n-i_2)T_s}$$

$$\times[\tilde{x}_1(n-i_1)]^{p-r_1-k_2}[\tilde{x}_1^*(n-i_1)]^{k_2} e^{j\omega_1(p-r_1-2k_2)(n-i_1)T_s}$$

$$\times[\tilde{x}_2(n-i_1)]^{r_2-k_3}[\tilde{x}_2^*(n-i_1)]^{k_3} e^{j\omega_2(r_2-2k_3)(n-i_1)T_s}$$

$$\times[\tilde{x}_3(n-i_1)]^{r_1-r_2-k_4}[\tilde{x}_3^*(n-i_1)]^{k_4} e^{j\omega_3(r_1-r_2-2k_4)(n-i_1)T_s}. \tag{B.6}$$

By regrouping the terms around the fundamental frequencies ω_1, ω_2, and ω_3 in (B.4), (B.5), and (B.6), the general equation in (5.12) can be reached. Similarly, the tri-dimensional dynamic function can be derived by further expansion of the dynamic expression in (5.15).

Bibliography

[1] Hsiao-Hwa Chen, Xi Zhang, and Wen Xu, "Next Generation CDMA vs. OFDMA for 4G Wireless Applications," *IEEE Wireless Communications*, vol. 14, no. 3, pp. 6-7, June 2007.

[2] M. Steer, "Beyond 3G," *IEEE Microw. Mag.*, vol. 8, no. 1, pp. 76-82, Feb. 2007.

[3] K. Rawat, M. Hashmi, F. M. Ghannouchi, "Double the Band and Optimize," *IEEE Microw. Mag.*, vol. 13, no. 2, pp. 69-82, March-April 2012.

[4] XA. Nghiem, J. Guan, T. Hone, and R. Negra, "Design of Concurrent Multiband Doherty Power Amplifiers for Wireless Applications," *IEEE Trans. Microw. Theory Tech.*, vol. 61, no. 12, pp. 4559-4568, Dec. 2013.

[5] A. Tasic, W.A. Serdijn, J.R. Long, "Adaptive multi-standard circuits and systems for wireless communications," *IEEE Circuits Syst. Mag.*, vol. 6, no. 1, pp. 29-37, 2006.

[6] A. A. Abidi, "Direct-conversion radio transceivers for digital communications," *IEEE J. Solid-State Circuits*, vol. 30, no. 12, pp. 1399-1410, Dec. 1995.

[7] P.-I. Mak, S.-P. U, and R. P. Martins, "Transceiver architecture selection: review, state-of-the-art survey and case study," *IEEE Circuits Syst. Mag.*, vol. 7, pp. 6-25, Apr. 2007.

[8] M. Valkama, A. Springer, G. Hueber, "Digital signal processing for reducing the effects of RF imperfections in radio devices-An overview," in *Proceeding of 2010 IEEE International Symposium on Circuits and Systems (ISCAS)*, June 2010, pp. 813-816.

[9] S. Cripps, *RF power amplifers for wireless communications*, 2nd ed. Boston: Artech House, 2006.

[10] J. K. Cavers, "The effect of quadrature modulator and demodulator errors on adaptive digital predistorters for amplifier linearization," *IEEE Trans. Veh. Technol.*, vol. 46, no. 2, pp. 456-466, May 1997.

[11] S. Myoung, Y. Kim, and J. Yook, "Impact of group delay in RF BPF on impulse radio systems," in *IEEE MTT-S Int. Microwave Symp. Dig.*, June 2005, pp. 1891-1894.

[12] R. Sapawi, R. K. Pokharel, S. A. Z. Murad, A. Anand, N. Koirala, H. Kanaya, and K. Yoshida, "Low group delay 3.1-10.6 GHz CMOS power amplifier for UWB applications," *IEEE Microw. and Wireless Compon. Lett.*, vol. 22, no. 1, pp. 41-43, Jan. 2012.

[13] Z. Zhu, H. Leung, X. Huang, "Challenges in Reconfigurable Radio Transceivers and Application of Nonlinear Signal Processing for RF Impairment Mitigation," *IEEE Circuits and Systems Magazine*, vol. 13, no. 1, pp. 44-65, Feb. 2013.

[14] L. Anttila, M. Valkama, M. Renfors, "Frequency-Selective I/Q Mismatch Calibration of Wideband Direct-Conversion Transmitters," *IEEE Trans. Circuits Syst. II: Exp. Briefs*, vol. 55, no. 4, pp. 359-363, Apr. 2008.

[15] F. H. Raab, P. Asbeck, S. Cripps, P. B. Kenington, Z. B. Popovic, N. Pothecary, J. F. Sevic, and N. O. Sokal, "Power amplifiers and transmitters for RF and microwave," *IEEE Trans. Microwave Theory Tech.*, vol. 50, no. 3, pp. 814-826, Mar. 2002.

[16] P. M. Lavrador, T. R. Cunha, P. M. Cabral, and J. C. Pedro, "The linearity-efficiency compromise," *IEEE Microw. Mag.*, vol. 11, no. 5, pp. 54-58, Aug. 2010.

[17] A. Katz, "Linearization: reducing distortion in power amplifiers," *IEEE Microw. Mag.*, vol. 2, no. 4, pp. 37-49, Dec. 2001.

[18] F. M. Ghannouchi, "Power amplifier and transmitter architectures for software defined radio systems," *IEEE Circuits Syst. Mag.*, vol. 10, pp. 56-63, 4th Quart. 2010.

[19] P. L. Gilabert, G. Montoro, P. Vizarreta, and J. Berenguer, "Digital processing compensation mechanisms for highly efficient transmitter architectures," *IET Microwaves, Antennas & Propagation*, vol. 5, no. 8, pp. 963-974, 2011.

[20] D. Gustafsson, C. M. Andersson, C. Fager, "A Modified Doherty Power Amplifier With Extended Bandwidth and Reconfigurable Efficiency," *IEEE Trans. Microw. Theory Tech.*, vol. 61, no. 1, pp. 533-542, Jan. 2013.

[21] J. Moon, J. Son, J. Kim, I. Kim, S. Jee, Y. Y. Woo, and B. Kim, "Doherty amplifier with envelope tracking for high efficiency," in IEEE MTT-S Int. Microwave Symp. Dig., Anaheim, CA, May 2010.

[22] F. Wang, D. F. Kimball, J. D. Popp, A. H. Yang, D. Y. C. Lie, P. M. Asbeck, and L. E. Larson, "Wideband envelope elimination and restoration power amplifier with high efficiency wideband envelope amplifier for WLAN 802.11g applications," in *IEEE MTT-S Int. Microwave Symp. Dig.*, June 2005, pp. 645-648.

[23] F. Wang, D. F. Kimball, J. D. Popp, A. H. Yang, D. Y. C. Lie, P. M. Asbeck, and L. E. Larson, "An improved power-added efficiency 19-dBm hybrid envelope elimination and restoration power amplifier for 802.11g WLAN applications," *IEEE Trans. Microw. Theory Tech.*, vol. 54, no. 12, pp. 4086-4099, Dec. 2006.

[24] I. Kim, J. Kim, J. Moon, and B. Kim, "Optimized envelope shaping for hybrid EER transmitter of mobile WiMAX Optimized ET operation," *IEEE Microw. Wireless Compon. Lett.*, vol. 14, no. 8, pp. 389-391, Aug. 2004.

[25] D. F. Kimball, J. Jeong, C. Hsia, P. Draxler, S. Lanfranco, W. Nagy, K. Linthicum, L. E. Larson, and P. M. Asbeck, "High-efficiency envelope tracking WCDMA base-station amplifier using GaN HFETs," *IEEE Trans. Microwave Theory Tech.*, vol. 54, no. 11, pp. 3848-3856, Nov. 2006.

[26] A. Zhu, P. J. Draxler, C. Hsia, T. Brazil, D. F. Kimball, and P. M. Asbeck, "Digital predistortion for envelope-tracking power amplifiers using decomposed piecewise Volterra series," *IEEE Trans. Microw. Theory Tech.*, vol. 56, no. 10, pp. 2237-2247, Oct. 2008.

[27] J. Jeong, D. F. Kimball, M. Kwak, C. Hsia, P. Draxler, and P. M. Asbeck, "Wideband envelope tracking power amplifiers with reduced bandwidth power supply waveforms and adaptive digital predistortion techniques," *IEEE Trans. Microw. Theory Tech.*, vol. 57, no. 12, pp. 3307-3314, Dec. 2009.

[28] M. Helaoui, S. Boumaiza, F. M. Ghannouchi, A. B. Kouki and A. Ghazel, "A New Mode-Multiplexing LINC Architecture to Boost the Efficiency of WiMAX Up-Link Transmitters," *IEEE Trans. Microw. Theory Tech.*, IEEE Trans. Microw. Theory Tech., vol. 55, no. 2, pp. 248-253, Feb. 2007.

[29] J. Choi, J. Yim, J. Yang, J. Kim, J. Cha, D. Kang, D. Kim, and B. Kim, "A Delta-Sigma-Digitized Polar RF Transmitter," *IEEE Trans. Microw. Theory Tech.*, vol. 55, no. 12, pp. 2679-2690, Dec. 2007.

[30] B. Shi, L. Sundstrom, "Linearization of RF power amplifier using power feedback," in *Proceedings of Vehicular Technology Conference (VTC) 1999*, vol. 2, pp.1520-1524, Jul. 1999.

[31] T.A. Johansen, K.J. Hunt, "A computational approach to approximate input/state feedback linearization," in *Proceedings of the 39th IEEE Conference on Decision and Control 2000*, vol. 5, pp. 4467-4472, June 2000.

[32] M. Faulkner, "Amplifier linearization using RF feedback and feedforward techniques," *IEEE Trans. Vehicular Tech.*, vol. 74, pp. 209-215, Feb. 1998.

[33] L. Larose, F. M. Ghannouchi, "Optimization of feedforward amplifier power efficiency on the basis of drive statistics," *IEEE Trans. Microw. Theory Tech.*, vol.51, no.1, pp.41-54, Jan. 2003.

[34] D. Huang, H. Leung, and X. Huang, "Experimental evaluation of predistortion techniques for high power amplifier," *IEEE Trans. Instrum. Meas.*, vol. 55, no. 6, pp. 2155-2164, Dec. 2006.

[35] E. G. Jeckeln, F. M. Ghannouchi, and M. A. Sawan, "A new adaptive predistortion technique using software-defined radio and DSP technologies suitable for base station 3G power amplifiers," *IEEE Trans. Microw. Theory Tech.*, vol. 52, no. 9, pp. 2139-2147, Sep. 2004.

[36] J. Kim and K. Konstantinou, "Digital predistortion of wideband signals based on power amplifier model with memory," *Electron. Lett.*, vol. 37, no. 23, pp. 1417-1418, Nov. 2001.

[37] F. M. Ghannouchi and O. Hammi, "Behavioural modeling and predistortion," *IEEE Microw. Mag.*, vol. 10, no. 7, pp. 52-64, Dec. 2009.

[38] J. C. Pedro and S. Maas, "A Comparative Overview of microwave and wireless power-amplifier behavioral modeling approaches," *IEEE Trans. Microw. Theory Tech.*, vol. 53, no. 4, pp. 1150-1163, Apr. 2005.

[39] M. Isaksson, D. Wisell, and D. Ronnow, "A comparative analysis of behavioral models for RF power amplifiers," *IEEE Trans. Microw. Theory Tech.*, vol. 54, no. 1, pp.348-359, Jan. 2006.

[40] F. M. Ghannouchi, M. Younes, and M. Rawat, "Distortion and impairments mitigation and compensation of single- and multi-band wireless transmitters (invited)," *IET Microwaves, Antennas & Propagation*, vol. 7, no. 7, pp. 518-534, May. 2013.

[41] P. Rykaczewski, M. Valkama, and M. Renfors, "On the connection of I/Q imbalance and channel equalization in direct-conversion transceivers,? *IEEE Trans. Veh. Technol.*, vol. 57, no. 3, pp. 1630-1636, May 2008.

[42] S. Bassam, W. Chen, M. Helaoui, and F. M. Ghannouchi, "Transmitter Architecture for CA: Carrier Aggregation in LTE-Advanced Systems," *IEEE Microw. Mag.*, vol. 14, no. 5, pp. 78-86, July-Aug. 2013.

[43] M. Windisch, G. Fettweis, "Adaptive I/Q imbalance compensation in low-IF transmitter architectures," in *Proceedings of Vehicular Technology Conference (VTC 2004)*, vol. 3, Sept. 2004, pp. 2096-2100.

[44] P. Colantonio, F. Giannini, R. Giofre, and L. Piazzon, "A design technique for concurrent dual-band harmonic tuned power amplifier," *IEEE Trans. Microw. Theory Tech.*, vol. 56, no. 11, pp. 2545-2555, Nov. 2008.

[45] R. Negra, A. Sadeve, S. Bensmida, and F. M. Ghannouchi, "Concurrent dual-band class-F load coupling network for applications at 1.7 and 2.14 Ghz," *IEEE Trans. Circuits and Syst. II: Exp. Briefs*, vol. 55, no. 3, pp. 259-263, March 2008.

[46] P. Saad, P. Colantonio, L. Piazzon, F. Giannini, K. Andersson, C. Fager, "Design of a Concurrent Dual-Band 1.8-2.4 GHz GaN-HEMT Doherty Power Amplifier," *IEEE Trans. Microw. Theory Tech.*, vol. 60, no. 6, pp. 1840-1849, June 2012.

[47] K. Rawat and F. M. Ghannouchi, "Design Methodology for Dual-Band Doherty Power Amplifier With Performance Enhancement Using Dual-Band Offset Lines," *IEEE Trans. Indust. Electron.*, vol. 59, no. 12, pp. 4831-4842, Dec. 2012.

[48] Z. Wang and W. C. Park, "Concurrent Tri-band GaN HEMT power amplifier using resonators in both input and output matching networks," in *2012 IEEE WAMICON Conf.*, USA, Apr. 2012, pp. 1-4.

[49] XA. Nghiem and R. Negra, "Novel design of a concurrent tri-band GaN-HEMT Doherty power amplifier," in *2012 Asia-Pacific Microwave Conference Proceedings (APMC)*, Taiwan, Dec. 2012, pp. 364-366.

[50] W. H. Chen, S. A. Bassam, X. Li, Y. Liu, M. Helaoui, K. Rawat, F. M. Ghannouchi, and Z. Feng, "Design and Linearization of Concurrent Dual-Band Doherty Power Amplifier

With Frequency-Dependent Power Ranges", *IEEE Trans. Microw. Theory Tech.*, vol. 59, no. 10, pp. 2537-2546, Oct. 2011.

[51] P. Roblin, S .K. Myoung, D. Chaillot, Y. G. Kim, A. Fathimulla, J. Strahler, and S. Bibyk, "Frequency selective predistortion linearization of RF power amplifiers," *IEEE Trans. Microw. Theory Tech.*, vol. 56, no. 1, pp. 65-76, Jan. 2008.

[52] S. A. Bassam, M. Helaoui, and F. M. Ghannouchi, "2-D digital predistortion (2-D-DPD) architecture for concurrent dual-band transmitters," *IEEE Trans. Microw. Theory Tech.*, vol. 59, no. 10, pp. 2547-2553, Oct. 2011.

[53] G. Fettweis, M. Lhning, D. Petrovic, M. Windisch, P. Zillmann, and W. Rave, "Dirty RF: A new paradigm," *Springer Int. J. Wireless Infor. Netw.*, vol. 14, no. 2, pp. 133-148, Jun. 2007.

[54] L. Ding, Z. Ma, D. R. Morgan, S. Member, M. Zierdt, G. T. Zhou, "Compensation of Frequency-Dependent Gain/Phase Imbalance in Predistortion Linearization Systems," *IEEE Trans. Circuits Syst. I:Reg. Papers*, vol. 55, no. 1, pp. 390-397, Feb. 2008.

[55] M. T. Le and L. Thibault, "Performance evaluation of COFDM for digital audio broadcasting. II: Effects of HPA Nonlinearities," *IEEE Trans. Broadcast.*, vol. 44, no. 2, pp. 165-171, Jun. 1998.

[56] P. Banelli, G. Baruffa and S. Cacopardi, "Effects of HPA non linearity on frequency multiplexed OFDM signals," *IEEE Trans. Broadcast.*, vol. 47, no. 2, pp. 123-136, Jun. 2001.

[57] M. Chrysochoos and J. Kim, "Performance analysis of an MC-CDMA broadcasting system under high power amplifier non-linearities, Part I: system proposal," *IEEE Trans. Broadcast.*, vol. 46, no. 4, pp. 256-262, Dec. 2000.

[58] K. J. Muhonen, M. Kavehrad, and R. Krishnamoorthy, "Look-up table techniques for adaptive digital predistortion: A development and comparison," *IEEE Trans. Veh. Technol.*, vol. 49, no. 9, pp. 1995-2002, Sep. 2000.

[59] J. S. Kenney, W. Woo, L. Ding, R. Raich, H. Ku, and G. T. Zhou, "The impact of memory effects on predistortion linearization of RF power amplifiers," in *Proc. 8th Int. Microw. Opt. Technol. Symp.*, Jun. 2001, pp. 189-193.

[60] P. Gilabert, G. Montoro and E. Bertran, "On the Wiener and Hammerstein models for power amplifier predistortion," in *2005 Asia-Pacific Microwave Conference Proceedings*, 2005, vol. 2, no. 2, pp. 1-4.

[61] P. Crama and Y. Rolain, "Broad-band Measurement and Identification of a Wiener-Hammerstein Model for an RF Amplifier," in *Proc. IEEE Automated RF Techniques Group(ARFTG) Conf.*, 2002, no. 5, pp. 49-57.

[62] T. Liu, S. Boumaiza, F. M. Ghannouchi, "Deembedding Static Nonlinearities and Accurately Identifying and Modeling Memory Effects in Wide-Band RF Transmitters," *IEEE Trans. Microw. Theory Tech.*, vol. 53, no. 11, pp. 3578-3587, Nov. 2005

[63] T. Liu, S. Boumaiza, and F. M. Ghannouchi, "Augmented Hammerstein Predistorter for Linearization of Broad-Band Wireless Transmitters," *IEEE Trans. Microw. Theory Tech.*, vol. 54, no. 4, pp. 1340?1349, Jun. 2006.

[64] F. Mkadem and S. Boumaiza, "Extended Hammerstein behavioral model using artificial neural networks," *IEEE Trans. Microw. Theory Tech.*, vol. 57, no. 4, pp. 745-751, Apr. 2009.

[65] O. Hammi, F. Ghannouchi, "Twin nonlinear two-box models for power amplifiers and transmitters exhibiting memory effects with application to digital predistortion," *IEEE Microw. Wireless Compon. Lett.*, vol. 19, no. 8, pp. 530-532, Aug. 2009.

[66] M. Younes, O. Hammi, A. Kwan, and F. M. Ghannouchi, "An accurate complexity-reduced 'PLUME' model for the behavioral modeling and digital predistortion of RF Power Amplifiers," *IEEE Trans. Ind. Electron.*, vol. 58, no. 4, pp. 1397-1405, Apr. 2011.

[67] J. Moon and B. Kim, "Enhanced Hammerstein Behavioral Model for Broadband Wireless Transmitters," *IEEE Trans. Microw. Theory Tech.*, vol. 59, no. 4, pp. 924-933, Apr. 2011.

[68] M. Younes, F. M. Ghannouchi, "An accurate predistorter based on a feedforward hammerstein structure," *IEEE Trans. Broadcast.*,vol.58, no.3, pp.454-461, Sept. 2012.

[69] C. Crespo-Cadenas, J. Reina-Tosina, and M. Madero-Ayora, "Volterra Behavioral Model for Wideband RF Amplifiers," *IEEE Trans. Microw. Theory Tech.*, vol. 55, no. 3, pp. 449-457, March 2007.

[70] M. Schetzen, *The Volterra & Wiener Theories of Nonlinear Systems. New York: Wiley*, 1989.

[71] A. Zhu, M. Wren, and T. J. Brazil, "An efficient Volterra-based behavioural model for

wideband RF power amplifiers," in *IEEE MTT-S Int. Microw. Symp. Dig.*, pp. 787-790, June 2003.

[72] D. R. Morgan, Z. Ma, J. Kim, M. G. Zierdt, and J. Pastalan, "A generalized memory polynomial model for digital predistortion of RF power amplifiers," *IEEE Trans. Signal Process.*, vol. 54, no. 10, pp. 3852-3860, Oct. 2006.

[73] R. Raich, H. Qian, and G. T. Zhou, "Orthogonal polynomials for power amplifier modeling and predistorter design," *IEEE Trans. Veh. Technol.*, vol. 53, no. 5, pp. 1468-1479, Sept. 2004.

[74] L. Ding and G. T. Zhou, "Effects of even-order nonlinear terms on power amplifier modeling and predistortion linearization," *IEEE Trans. Veh. Technol.*, vol. 53, no. 1, pp. 156?162, Jan. 2004.

[75] O. Hammi, M. Younes and F. M. Ghannouchi, "Metrics and Methods for Benchmarking of Rf Transmitter Behavioral Models with Application to the Development of a Hybrid Memory Polynomial Model," *IEEE Trans. Broadcast.*, vol. 56, no. 3, pp. 350-357, Sept. 2010.

[76] D. Mirri, G. Iuculano, F. Filicori, G. Pasini, G. Vannini, and G. P. Gualtieri, "A modified Volterra series approach for nonlinear dynamic systems modeling," *IEEE Trans. Circuits Syst. I*, Fundam. Theory Appl., vol. 49, no. 8, pp. 1118-1128, Aug. 2002.

[77] N. Safari, T. Rste, P. Fedorenko, and J. S. Kenny, "An approximation of Volterra series using delay envelopes, applied to digital predistortion of RF power amplifiers

with memory effects," *IEEE Microw. Wireless Compon. Lett.*, vol. 18, no. 2, pp. 115-117, Feb. 2008.

[78] A. Zhu, J. C. Pedro, and T. J. Brazil, "Dynamic deviation reduction based Volterra behavioral modeling of RF power amplifiers," *IEEE Trans. Microw. Theory Tech.*, vol. 54, no. 12, pp. 4323-4332, Dec. 2006.

[79] A. Zhu, J.C. Pedro, and T.R. Cunha, "Pruning the Volterra series for behavioral modeling of power amplifiers using physical knowledge," *IEEE Trans. Microw. Theory Tech.*, vol. 55, no. 5, pp. 813-821, May 2007.

[80] M. Isaksson, D. Wisell, and D. Ronnow, "Wide-band dynamic modeling of power amplifiers using radial-basis function neural networks," *IEEE Trans. Microw. Theory Tech.*, vol. 53, no. 11, pp. 3422-3428, Nov. 2005.

[81] M. Rawat, K. Rawat, and F.M. Ghannouchi, "Adaptive Digital Predistortion of Wireless Power Amplifiers/Transmitters Using Dynamic Real-Valued Focused Time-Delay Line Neural Networks," *IEEE Trans. Microw. Theory Tech.*, vol. 58, no. 1, pp. 95-104, Jan. 2010.

[82] A. S. Tehrani, H. Cao, S. Afsardoost, T. Eriksson, M. Isaksson, and C. Fager, "A comparative analysis of the complexity/accuracy tradeoff in power amplifier behavioral models," *IEEE Trans. Microw. Theory Tech.*, vol. 58, no. 7, pp. 1510-1520, Jun. 2010.

[83] M. Younes, O. Hammi and F. M. Ghannouchi, "Algorithm for Model Dimensions Estimation of Memory Polynomial-Based RF Transmitters / Power Amplifiers Behavioral

Models," *International Journal of Microwave and Optical Technology*, vol. 4, no. 4, pp. 242-247, Jul. 2009.

[84] J.H.K. Vuolevi, T. Rahkonen and J.P.A. Manninen, "Measurement technique for characterizing memory effects in RF power amplifiers," *IEEE Trans. Microw. Theory Tech.*, vol. 49, no. 8, pp. 1383-1389, Dec. 2001.

[85] D. Schreurs, M. O'droma, A.A. Goacher and M. Gardinger, *RF Power Amplifier Behavioral Modeling*, Cambridge University Press, 2009.

[86] T. Liu, Y. Ye, S. Boumaiza, M. Helaoui, O. Hammi, and F. M. Ghannouchi, "Accurate identification of static nonlinear properties of wideband RF power amplifiers," in *International Conference on Microwave and Millimeter Wave Technology (ICMMT)*, April 2008, pp. 1351-1354.

[87] O. Hammi and F. M. Ghannouchi, "Power alignment of digital predistorters for power amplifiers linearity optimization," *IEEE Trans. Broadcast.*, vol. 55, no. 1, pp. 109-114, Mar. 2009.

[88] P. Landin, M. Isaksson and P. Handel, "Comparison of evaluation criteria for power amplifier behavioral modeling," in *Proc. IEEE MTT-S Int. Microwave Symposium*, Atlanta, GA, Jun. 2008, pp. 1441-1444.

[89] D. Wisell, M. Isaksson, and N. Keskitalo, "A general evaluation criteria for power amplifier behavioral PA models," in *Proc. 69th ARFTG Conf. Dig.*, 2007, pp. 251-255.

[90] A. Cantoni and J. Tuthill, "Digital compensation of frequency dependent imperfections

in direct conversion I-Q modulators," in *Proc. IEEE Int. Circuits Systems. Symp.*, May 2007, pp. 269-272.

[91] M. Valkama, M. Renfors, and V. Koivunen, "Compensation of frequency selective I/Q imbalances in wideband receivers: Models and algorithms," *in Proc. 3rd IEEE Signal Process. Workshop (SPAWC)*, Taoyuan, Taiwan, Mar. 2001, pp. 42-45.

[92] H. Cao, A. S. Tehrani, C. Fager, T. Eriksson, and H. Zirath, "I/Q Imbalance Compensation using a Nonlinear Modeling Approach," *IEEE Trans. Microw. Theory Tech.*, vol. 57, pp. 513-518, Mar. 2009.

[93] M. Li, L. Hoover, K. G. Gard, M. B. Steer, "Behavioural modelling and impact analysis of physical impairments in quadrature modulators," *IET Microwaves, Antennas & Propagation*, vol. 4, no. 12, pp. 2144-2154, Dec. 2010.

[94] Y. Kim, E. Jeong, Y. H. Lee, "Adaptive compensation for power amplifier nonlinearity in the presence of quadrature modulation / demodulation errors," *IEEE Trans. Sig. Process.*, vol. 55, no. 9, pp. 4717-4721, Sept. 2007.

[95] L. Anttila, P. Handel, and M. Valkama, "Joint Mitigation of Power amplifier and I/Q Modulator Impairments in Broadband Direct-Conversion Transmitters," *IEEE Trans. Microw. Theory Tech.*, vol. 58, no.4, pp. 730-739, Apr. 2010.

[96] M. Younes and F. M. Ghannouchi, "Generalised twin-box model for compensation of transmitters radio frequency impairments," *IET Communications*, vol. 8, no. 4, pp.413-418, Mar. 2014.

[97] S. A. Bassam, W. Chen, M. Helaoui, F. M. Ghannouchi, and Z. Feng, "Linearization of concurrent dual-band power amplifier based on 2D-DPD technique," *IEEE Microw. Wireless Compon. Lett.*, vol. 21, no. 12, pp. 685-687, Dec. 2011.

[98] R. N. Braithwaite, "Digital predistortion of a power amplifier for signals comprising widely spaced carriers," in *Proc. 78th ARFTG Microwave Meas. Conf.*, Tempe, AZ, Dec. 2011, pp. 1-4.

[99] Y. J. Liu, W. Chen, J. Zhou, B. Zhou and F. M. Ghannouchi, "Digital predistortion for concurrent dual-band transmitters using 2-D modified memory polynomials," *IEEE Trans. Microw. Theory Tech.*, vol. 61, no. 1, pp. 281-290, Jan. 2013.

[100] J. Moon, P. Saad, J. Son, C. Fager, B. Kim, "2-D enhanced hammerstein behavior model for concurrent dual-band power amplifiers," in *Proc. Microwave Conf. 42nd European*, Oct. 2012, pp. 1249-1252.

[101] J. Kim, P. Roblin, D. Chaillot, and Z. Xie, "A generalized architecture for the frequency-selective digital predistortion linearization technique," *IEEE Trans. Microw. Theory Tech.*, vol. 61, no. 1, pp. 596-605, Jan. 2013.

[102] P. Roblin, *Nonlinear RF circuits and nonlinear vector network analyzers: Interactive measurement and design techniques*. Cambridge, U.K.: Cambridge Univ., 2011.

[103] Y. Jin and F.F. Dai, "Impact of Transceiver RFIC Impairments on MIMO System Perfromance," *IEEE Trans. Ind. Electron.*, vol. 59, no. 1, pp. 538-549, Jan. 2012.

[104] D. Saffar, N. Boulejfen, F. M. Ghannouchi, and M. Helaoui, "Compensation of I/Q impairments and nonlinear distortion in MIMO wireless transmitters," in *2013 IEEE 11th*

International New Circuits and Systems Conference (NEWCAS'2013), Paris, France, June 2013, pp. 1-4.

[105] M. Rawat, K. Rawat, M. Younes, and F. M. Ghannouchi, "Joint Mitigation of Non-Linearity and modulator imperfections in a dual-band Concurrent Transmitter Using Neural Networks," *IET Electronics Letters*, vol. 49, no. 4, pp. 253-255, Feb. 2013.

[106] M. Younes and F. M. Ghannouchi, "On the modeling and linearization of a concurrent dual-band transmitter exhibiting nonlinear distortion and hardware impairments," *IEEE Trans. Circuits Syst. I*, Reg. Papers, vol. 60, no. 11, pp. 3055-3068, Nov. 2013.

[107] X. Li, W. H. Chen, Z. Zhang, Z. Feng, X. Tang, and K. Mouthaan, "A Concurrent Dual-Band Doherty Power Amplifier," in *Proceedings of Asia-Pacific Microwave Conference*, Dec. 2010, pp. 654-657.

[108] M. Younes, A. Kwan, M. Rawat, and F. M. Ghannouchi, "Three-dimensional digital predistorter for concurrent tri-band power amplifier linearization," in *IEEE MTT-S Int. Microw. Symp. Dig.*, Seattle, WA, Jun. 2013, pp. 1-4.

[109] E. G. Lima, T. R. Cunha, and J .C. Pedro, "A physical-meaningful neural network behavioral model for wireless transmitters exhibiting PM-AM/PM-PM distortions," *IEEE Trans. Microw. Theory Tech.*, vol. 59, no. 12, pp. 3512-3521, Dec. 2011.

[110] E. G. Lima, T. R. Cunha, and J. C. Pedro, "PM-AM/PM-PM distortions in wireless transmitter behavioral modeling," in *IEEE MTT-S Int. Microw. Symp. Dig.*, Baltimore, MD, Jun. 2011, pp. 1-4.

[111] M. Younes, A. Kwan, M. Rawat, and F. M. Ghannouchi, "Linearization of Concurrent Tri-Band Transmitters Using 3-D Phase-Aligned Pruned Volterra Model," *IEEE Trans. Microw. Theory Tech.*, vol. 61, no. 12, pp. 4569-4578, Dec. 2013.

[112] Y. J. Liu, W. Chen , B. Zhou , J. Zhou and F.M. Ghannouchi, "2D augmented Hammerstein model for concurrent dual-bandpower amplifiers," *IET Electron. Lett.*, vol. 48, no. 11, pp. 1214-1216, Sept. 2012.

[113] S. Zhang, W. Chen , F. M. Ghannouchi, and Y. Chen, "An iterative pruning of 2-D digital predistortion modelbased on normalized polynomial terms," in *IEEE MTT-S Int. Microw. Symp. Dig.*, Seattle, WA, Jun. 2013, pp. 1-4.

[114] L. Ding, Z. Yang, and H. Gandhi, "Concurrent dual-band digital predistortion," in *IEEE MTT-S Int. Microw. Symp. Dig.*, Seattle, WA, Jun. 2013, pp. 1-4.

[115] G. Yang, F. Liu, L. Li, H.Wang, C. Zhao, and Z. Wang, "2D orthogonal polynomials for concurrent dual-band digital predistortion," in *IEEE MTT-S Int. Microw. Symp. Dig.*, Seattle, WA, Jun. 2013, pp. 1-4.

[116] C. Quindroit, N. Naraharisetti, P. Roblin, S. Gheitanchi, V. Mauer, and M. Fitton, "Concurrent dual-band digital predistortion for power amplifier based on orthogonal polynomials," in *IEEE MTT-S Int. Microw. Symp. Dig.*, Seattle, WA, Jun. 2013, pp. 1-4.

[117] C. Quindroit, N. Naraharisetti, P. Roblin, S. Gheitanchi, V. Mauer, and M. Fitton, "FPGA Implementation of Orthogonal 2D Digital Predistortion System for Concurrent Dual-Band Power Amplifiers Based on Time-Division Multiplexing," *IEEE Trans.*

Microw. Theory Tech., vol. 61, no. 12, pp. 4591-4599, Dec. 2013.

[118] M. Younes, A. Kwan, and F. M. Ghannouchi, "Digital Predistortion of Concurrent Dual-Band Power Amplifier based on Two-dimensional Multi-Branch DPD," *IEEE Canadian Conference on Electrical and Computer Engineering 2014* (CCECE 2014), Toronto, On., May. 2014, pp. 1-5.

[119] C. Crespo-Cadenas, J. Reina-Tosina, M. Madero-Ayora, and J. Munoz-Cruzado, "A new approach to pruning Volterra models for power amplifiers," *IEEE Trans. Sig. Process.*, vol.58, no.4, pp. 2113-2120, April 2010.

[120] A. Kwan, M. Younes, S. Zhang, W. Chen, R. Darraji, M. Helaoui, F. M. Ghannouchi, "Dual-band Predistortion Linearization of an Envelope Modulated Power Amplifier Operated in Concurrent Multi-Standard Mode," in *IEEE MTT-S Int. Microw. Symp. Dig. 2014*, Tampa bay, Florida, USA, Jun. 2014, pp. 1-4.